

Chem Soc Rev

Chemical Society Reviews

rsc.li/chem-soc-rev



ISSN 0306-0012

REVIEW ARTICLE

Dan Wu, Lang Rao, Xiaoyuan Chen, Guocan Yu *et al.*
Metal-free bioorthogonal click chemistry in cancer
theranostics



Cite this: *Chem. Soc. Rev.*, 2022, **51**, 1336

Metal-free bioorthogonal click chemistry in cancer theranostics

Dan Wu,^{†*a} Kuikun Yang,^{†b} Zhankui Zhang,^a Yunxuan Feng,^c Lang Rao,^{*d} Xiaoyuan Chen ^{*e} and Guocan Yu ^{*c}

Bioorthogonal chemistry is a powerful tool to site-specifically activate drugs in living systems. Bioorthogonal reactions between a pair of biologically reactive groups can rapidly and specifically take place in a mild physiological milieu without perturbing inherent biochemical processes. Attributed to their high selectivity and efficiency, bioorthogonal reactions can significantly decrease background signals in bioimaging. Compared with metal-catalyzed bioorthogonal click reactions, metal-free click reactions are more biocompatible without the metal catalyst-induced cytotoxicity. Although a great number of bioorthogonal chemistry-based strategies have been reported for cancer theranostics, a comprehensive review is scarce to highlight the advantages of these strategies. In this review, recent progress in cancer theranostics guided by metal-free bioorthogonal click chemistry will be depicted in detail. The elaborate design as well as the advantages of bioorthogonal chemistry in tumor theranostics are summarized and future prospects in this emerging field are emphasized.

Received 13th August 2021

DOI: 10.1039/d1cs00451d

rsc.li/chem-soc-rev

^a College of Materials Science and Engineering, Zhejiang University of Technology Hangzhou, 310014, P. R. China. E-mail: danwu@zjut.edu.cn

^b State Key Laboratory of Quality Research in Chinese Medicine, Institute of Chinese Medical Sciences, University of Macau, Avenida da Universidade, Taipa, Macau 999078, P. R. China

^c Key Laboratory of Bioorganic Phosphorus Chemistry & Chemical Biology, Department of Chemistry, Tsinghua University, Beijing 100084, P. R. China. E-mail: guocanyu@mail.tsinghua.edu.cn

^d Institute of Biomedical Health Technology and Engineering, Shenzhen Bay Laboratory, Shenzhen 518132, P. R. China. E-mail: lrhao@szbl.ac.cn

^e Yong Loo Lin School of Medicine and Faculty of Engineering, National University of Singapore, Singapore, 117597, Singapore. E-mail: chen9647@gmail.com

[†] These authors contributed equally to this work.



Dan Wu

Dan Wu was born in Henan, China, in 1988. She received her PhD degree from Zhejiang University in 2016 under the supervision of Prof. Guping Tang. She is currently an associate researcher at the college of materials science and engineering at Zhejiang University of Technology. Her current research interests are focused on the construction of functional biomaterials.



Lang Rao

Lang Rao received his BS degree in Physics and PhD degree in Electrical Engineering both from Wuhan University, China. After the graduation, he started his postdoc carrier at the University of Texas Southwestern Medical Center (UTSW) under the supervision of Dr Jinming Gao. In the spring of 2019, he moved to the National Institutes of Health (NIH) as a research fellow with Dr Xiaoyuan (Shawn) Chen. Then he initiated his independent research carrier in late 2020 at the Shenzhen Bay Laboratory, China. Dr Rao's research aims to create cutting-edge nanotechnology and exploit them to study and solve complex biological problems that are associated with human diseases. One major research interest is developing smart biomaterials and devices to overcome the barriers in the treatment of cancer and viral infection.

1. Introduction

Cancer is a general term for many difficult miscellaneous diseases which are characterized by rapid and uncontrolled cellular division, threatening the lives of millions of people in the world every year.^{1–5} In order to overcome the limitations of traditional chemotherapeutic drugs including limited bioavailability, poor solubility, severe side effects and short half-life, nanomedicines have been proposed and regarded as ideal formulations over the past decades.^{6–13} Nanomedicines can selectively deliver therapeutic drugs and diagnostic probes to the target sites *via* the enhanced permeability and retention (EPR) effect (also named as passive targeting), active targeting or stimuli-responsiveness strategies.^{14–19} However, several challenges hinder the clinical translation of nanomedicines. For example, nanomedicines always accumulate at the perivascular site of tumors owing to the EPR effect, leading to the inhomogeneous drug distribution in the tumor.^{20–25} Meanwhile, the efficacy of EPR-based tumor accumulation of nanomedicines may vary significantly among different patients owing to the heterogeneousness of tumors.^{26–32} For active targeting strategy, there may be marginal difference in the expression of target receptors between tumor and normal cells, leading to low efficacy and poor selectivity of a variety of nanomedicines.^{33–40} As for the stimuli-responsiveness strategy, there may be little differences between normal and tumor tissues in regards to the acidity or enzymatic activity. As a result, severe damage may be found in normal tissues.^{41–46} Sometimes, an endogenous factor (such as receptor expression, acidity or enzymatic activity)-dependent tumor selectivity may impair the theranostic performances of nanomedicines in a certain degree.

In addition to the intrinsic barriers of tumors, conventional nanomedicines also suffer from inherent drawbacks including low drug loading efficiency, premature drug leakage, poor colloidal stability and potential cytotoxicity.^{47–53} To overcome these drawbacks, prodrug-based nanosystems have emerged as a new generation of nanomedicines with great potential. Prodrug strategies endow nanomedicines with the high drug loading efficiency, favorable pharmacokinetics, enhanced stability, and site-specific drug release.^{54–59} On-demand activation of prodrugs by chemical reactions without essential biological mediators can realize an accurate control over the target sites (*e.g.*, tumor *in situ*), thus minimizing the damage to healthy tissues.^{60–65}

Bioorthogonal chemistry is a sophisticated tool to spatially-temporally activate prodrugs both *in vitro* and *in vivo*. Bioorthogonal reactions occur rapidly and specifically in a mild physiological milieu without perturbation from inherent biochemical processes.^{66–71} Because of the high selectivity, bioorthogonal reactions greatly decrease background signals from cross reactions in organisms.^{72–80} The first bioorthogonal reaction, also a modified Staudinger ligation, occurred between an azide group and a triarylphosphine group.⁶⁶ However, Staudinger ligation is hardly applied in biological events mainly because of the slow kinetics ($8.0 \times 10^{-3} \text{ M}^{-1} \text{ s}^{-1}$).^{81–85} In 2001, Sharpless *et al.* put forward the term of click chemistry and defined a series of strict standards for click reactions: (1) modular and wide in scope, the starting materials and reagents are readily available; (2) mild reaction conditions (insensitive to water and oxygen), high yields and harmless byproducts that are eliminated by distillation or crystallization; (3) stereospecific and stable products in physiological environment.⁸⁶ Owing to the advantages



Xiaoyuan Chen

Xiaoyuan (Shawn) Chen received his PhD in Chemistry from the University of Idaho (1999). After two postdocs at Syracuse University and Washington University in St. Louis, he started his Assistant Professorship in 2002 and then moved to Stanford in 2004. He was promoted to Associate Professor in 2008. He moved to NIH in 2009 and became a Senior Investigator and Chief of the Laboratory of Molecular Imaging and Nanomedicine (LOMIN) at

the National Institute of Biomedical Imaging and Bioengineering (NIBIB), NIH. He is currently Nasrat Muzayyin Professor in Medicine and Technology, Yong Loo Lin School of Medicine and Faculty of Engineering, National University of Singapore. Dr Chen has published over 800 peer-reviewed papers (H-index: 158, total citations > 92 000 based on google scholar) and numerous books and book chapters. He is the founding editor of journal "Theranostics" (2019 IF = 11.556).



Guocan Yu

Guocan Yu received his PhD degree from Zhejiang University in 2015 under the direction of Prof. Feihe Huang. He spent five years as a postdoctoral fellow in Dr Xiaoyuan (Shawn) Chen's research group at National Institutes of Health (NIH) from 2015 to 2020. He starts his independent research carrier in Department of Chemistry at Tsinghua University in late 2020. His research interests are focused on the development of

smart delivery systems, supramolecular theranostics and supramolecular strategies for immune modulation.

of intrinsic selectivity and tunable electronics, copper-catalyzed [3+2] azide-alkyne cycloaddition (CuAAC) was developed by Meldal, Sharpless *et al.* in 2002 and has been applied in areas of drug design and biomolecule labelling.^{87,88} Compared with Staudinger ligation, CuAAC exhibits almost 1000-fold higher reaction rate ($10 \text{ M}^{-1} \text{ s}^{-1}$).⁸⁹ However, copper(i) catalyst is cytotoxic to mammalian and bacterial cells, which significantly restricts the biological applications of CuAAC. To get rid of metal catalysts and improve the reaction rate of cycloaddition, Bertozzi *et al.* utilized the ring-strain to increase the reactivity of azide-alkyne reactions.⁹⁰⁻⁹² The second order reaction rates of the strain-promoted azide-alkyne cycloaddition (SPAAC) were greatly enhanced (*e.g.* $7.6 \times 10^{-2} \text{ M}^{-1} \text{ s}^{-1}$ for difluorinated cyclooctyne (DIFO) system), but its water solubility was unsatisfactory. Meanwhile, the side reactions between cyclooctynes and biological thiols (such as serum albumin and glutathione) inevitably led to undesired background interferences. During the same period, thiol-ene coupling (TEC), a century-old reaction between thiols and alkenes, emerged as an effective click reaction after optimization by Schlaad and coworkers. The photo-/thermo-induced TEC reactions are supported by a radical mechanism and have been developed into efficient ligation tools for glycopeptides and peptides copolymerization.⁹³⁻⁹⁷ However, this reaction is reversible and easily affected by the cellular thiols, thus its applications in bioorthogonal field are also limited.⁹⁸ In 2008, Fox *et al.* explored inverse-electron demand Diels-Alder (iEDDA) reaction by using a *trans*-cyclooctene (TCO) containing probe and a bipyridyltetrazine-tethered probe.⁹⁹ The reaction rate of this copper-free click reaction was orders of magnitude higher than any other CuAAC reactions.¹⁰⁰ Nevertheless, because *trans*-cyclooctenes can easily transform into inert *cis*-isomers, this click reaction needs to be further optimized.¹⁰¹ Inspired by the synthetic pathway of D-luciferin in fireflies, Rao *et al.* developed a thiol-based condensation between D-cysteine (D-Cys) and 2-cyanobenzothiazole (CBT).¹⁰² The rate constant of this click reaction was about $9.0 \text{ M}^{-1} \text{ s}^{-1}$ and the reaction could proceed in different physiological conditions.^{103,104} The “photo-click” reaction between an alkene and a nitrile imine may provide us more bioorthogonal strategies owing to the well-controlled spatiotemporal properties. Interestingly, the starting tetrazole is non-fluorescent, but the product pyrazoline emits strong fluorescence, making it an attractive imaging agent for cancer theranostic.¹⁰⁵⁻¹⁰⁷ The Pictet-Spengler reactions have played a key role in the synthesis of indole alkaloids since 1911.¹⁰⁸ The canonical Pictet-Spengler reactions are condensations between an aldehyde (ketone) and a β -arylethylamine. However, the Pictet-Spengler reactions always take place at weak acidic condition and their products are unstable in storage. To overcome these limitations, an improved variation-hydrazino-Pictet-Spengler (HIPS) ligation was developed and has been widely applied in protein labelling.¹⁰⁹⁻¹¹³ Notably, Michael additions between thiol and maleimide/enone are also widely used click reactions. Considering that their related biological applications have been well discussed in other reviews, we will not discuss this reaction here.

In general, click reactions are classified into two parts: metal-catalyzed click reactions and metal-free click reactions. Cu-Catalysed CuAAC have prevailed in some physiological conditions where cytotoxicity can be neglected, such as in cell lysates and in fixed cells.¹¹⁴ Nevertheless, CuAAC are not suitable for dynamic physiological processes due to the cytotoxicity of copper catalysts. Although some ligands have been applied to decrease the toxicity, the procedures are complicated and cannot fundamentally address the problem.¹¹⁵⁻¹¹⁷ On the contrary, metal-free click reactions can be safely and efficiently applied in living organisms for multiple treatment purposes.^{118,119} Table 1 summarizes the recently developed metal-free click reactions. Although some reviews about metal-free click reactions have been reported, most of them mainly focused on biomolecule labelling/imaging and prodrug activation. With a growing number of cancer theranostics researches supported by bioorthogonal chemistry in recent years,^{120,121} a review systematically introducing the development of these theranostics is needed.

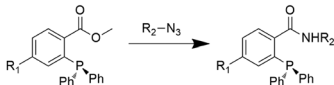
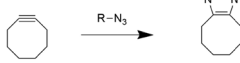
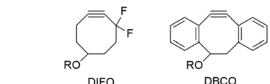
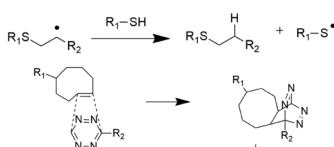
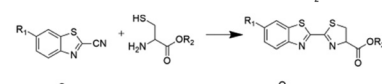
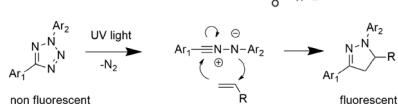
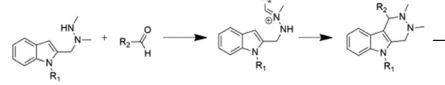
This review will present a variety of novel strategies for cancer theranostics on the basis of metal-free bioorthogonal chemistry, which is divided into two parts: cancer diagnosis and cancer therapy. Cancer diagnosis will be discussed according to various imaging methods, such as fluorescence imaging (FI), magnetic resonance imaging (MRI), photoacoustic imaging (PAI), positron-emission tomography (PET) imaging and Raman imaging (RI). Cancer therapy will be discussed according to the therapeutic modalities, including chemotherapy, photodynamic therapy (PDT), photothermal therapy (PTT) and immunotherapy. With the rapid development of organic methodology, materials science and biochemistry, more and more bioorthogonal reactions are expected to bring us more smart modalities for precise cancer theranostics.

2. Metal-free bioorthogonal click chemistry for cancer diagnosis

2.1 Metal-free bioorthogonal click chemistry for fluorescence imaging

High signal to noise (S/N) ratio is urgently desired in imaging/detecting biomolecules in the organisms. In case of proteins, genetically encoded reporters (*e.g.* green fluorescent protein) can be used as probes. However, lipids and glycans cannot be imaged by the same method because they are post-translational modifications that cannot be modified by genetically encoded reporters. Although these biomolecules have already been investigated in the static systems and *in vitro*, their real-time behaviors in living systems are not well monitored. Bertozzi *et al.* designed a ring strain-promoted [3+2] cycloaddition reaction between DIFO derivatives and azide analogues to reveal the glycosylation process (Fig. 1a-I).⁹⁰ This kind of cycloaddition reactions was 17–63 times faster than the reported similar cycloadditions or Staudinger ligations. After labelled for 1 min, the cell-surface glycans bearing azide groups were imaged with high S/N. Furthermore, the trafficking

Table 1 Summary of metal-free bioorthogonal click reactions

Name	Representative reaction	k ($M^{-1} s^{-1}$)	Merits/demerits	Ref.
Staudinger ligation		$\sim 8.0 \times 10^{-3}$	Slow kinetics	271
SPAAC		0.1	No metal catalyst; moderate kinetics	73
TEC		—	Reversible; high cross-reactivity	—
iEDDA		$\sim 1-10^6$	No metal catalyst; very high kinetics	272
Thiol-based click reaction		~ 9	Moderate kinetics; reaction under different controllable physiological conditions (enzymes, pH and reductions)	105
“Photo-click” reaction		~ 11	Spatiotemporal controllability; fluorescent switch	108
Pictet-Spengler reaction		—	Under weak acidic environment; product unstable	—

pathway of the glycans was revealed and the half-life of glycosylation process was calculated to be 15 min (Fig. 1a-II). This Cu-free SPAAC reaction showed comparable kinetics as the Cu-catalyzed click reactions but without any metal cytotoxicity, displaying great potential in site-specific labelling of other metabolites in living systems.

Tirrell *et al.* designed a series of membrane-penetrable DIFO derivatives (1–3) by conjugation with coumarin (Fig. 1b-I).⁹² The fluorescence test indicated that coumarin-labelling was specific to azidohomoalanine (Aha) which was related to the new generated proteins in the period of Aha pulse. Confocal slices and cellular protein analysis confirmed that the labelling happened not only on cell membranes, but also inside cells. It was worth noting that the optimal concentration of compound 3 is 10 μ M (Fig. 1b-II). The reason may be ascribed to the side reactions (thiol addition reactions) between coumarin-cyclooctyne conjugates and cellular nucleophiles. Hence, when using 3 as a labelling probe, the undesired side reactions should be avoided. The mean fluorescence enhancement in

optimal conditions reached eightfold or higher, providing an efficient tool for real-time imaging of protein modifications that are not accessible previously.

Although bioorthogonal reactions have been applied in various biological fields, such as monitoring zebrafish development and exploring metabolic pathways,^{122,123} there are few reports about their *in vivo* applications, particularly for the targeted transportation of nanomedicines. Owing to the outstanding properties of nanoparticles, *e.g.* long circulation time and multivalent effect, nanomedicines bind to azide groups bearing unnatural glycans on target cells more easily than small molecular drugs. Kim *et al.* introduced a novel targeting strategy based on bioorthogonal SPAAC reaction, metabolic glycoengineering and nanotechnology (Fig. 1c-I).¹²⁴ Unnatural sialic acids bearing azide groups were easily anchored on the surfaces of target tumor cells in a dose-dependent way when using a tetraacetylated *N*-azidoacetyl-D-mannosamine ($Ac_4ManNAz$) precursor. PEGylated liposomes (PEG-lipo, PEG = poly(ethylene glycol)), a widely used nano-sized drug delivery system, were

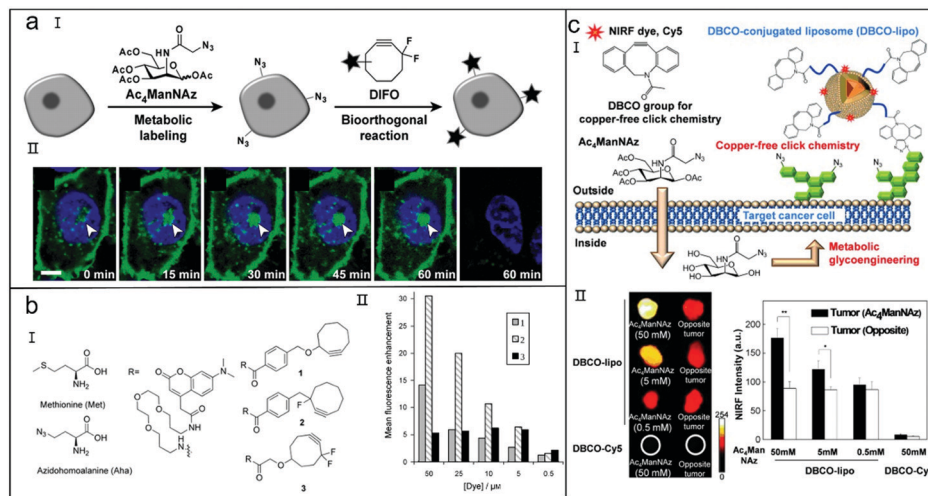


Fig. 1 (a) Bioorthogonal reactions between DIFO derivatives and artificial glycans bearing azide groups to monitor the kinetic processes of living system. (I) Mechanism of glycan detection. (II) Real-time imaging of a cell over the period of 1 h. Scale bar: 5 μm. Reproduced with the permission from ref. 90. Copyright 2007, The National Academy of sciences of the USA. (b) Bioorthogonal reactions involving coumarin–cyclooctynes to image newly synthesized proteins in living system. (I) Structures of coumarin–cyclooctynes and protein precursors. (II) Cellular fluorescence analysis under different coumarin–cyclooctynes concentrations. Reproduced with the permission from ref. 92. Copyright 2010, Wiley-VCH Verlag GmbH & Co. KGaA, Weinheim. (c) Tumor-targeted transport of nanoparticles *in vivo* with the aid of bioorthogonal DBCO/azide click reaction. (I) Illustration of tumor-targeted nanoparticle delivery *in vivo*. (II) *Ex vivo* near-infrared fluorescence images and fluorescence analysis after different treatments. Reproduced with the permission from ref. 124. Copyright 2012, Wiley-VCH Verlag GmbH & Co. KGaA, Weinheim.

conjugated with dibenzyl cyclooctyne (DBCO) groups to generate DBCO-lipo. For ease of viewing, near-infrared (NIR) fluorescence dye Cy5 was incorporated into DBCO-lipo. As a control group, DBCO-Cy5 (DBCO was conjugated with Cy5) was designed. After synergistic action of metabolic glycoengineering and bioorthogonal chemistry, the fluorescence of DBCO-lipo in the tumor increased with an increasing concentration of Ac₄ManNAz. Due to the fast clearance and short circulation time, the accumulation of DBCO-Cy5 in the tumor was obviously lower than DBCO-lipo, confirming that the multivalent effect and long circulation time of nanoparticles were beneficial to *in vivo* bioorthogonal chemistry (Fig. 1c-II). As a result, the combination of metabolic glycoengineering and bioorthogonal chemistry significantly promoted the development of targeted drug delivery systems for cancer diagnosis and treatment.

Under physiological conditions, thiol–yne click interactions or hydrophobic interactions always lead to noise signals or even compromise the efficiency of cyclooctyne in bioorthogonal systems. To avoid these unspecific interactions, polar or water-soluble cyclooctynes are desired. Delft *et al.* developed a set of bicyclo[6.1.0]nonyne (BCN)-derived cyclooctynes (A-BCN (5), GA-BCN (6) and BHM-BCN (7)) with excellent hydrophilicity, high reactivity and specificity (Fig. 2a-I).¹²⁵ Compared with BCN, the membrane staining of A-BCN and GA-BCN in HEK293 cells was more obvious. Furthermore, A-BCN selectively stained the Golgi apparatus, providing the possibility to study the dynamic glycan trafficking (Fig. 2a-II). These polar BCN-derived cyclooctynes showed the improved labelling specificity for the *N*-glycan of the transient receptor potential vanilloid type 5 (TRPV5) with high S/N ratio, representing a

useful tool for visualising glycans of membrane proteins in living systems (Fig. 2a-III).

Metabolic labelling and subsequent fluorescent imaging of DNA are basic techniques for decoding the location and timing of DNA synthesis in living systems. However, all the bioorthogonal reporters of RNA and DNA relied on alkyne–azide click reactions. Therefore, an alternative bioorthogonal click reaction for DNA imaging should be put forward to enrich the species of DNA and RNA probes. Luedtke *et al.* designed a metabolic probe 5-vinyl-2'-deoxyuridine (VdU) for DNA labelling based on the iEDDA click reaction (Fig. 2b-I).¹²⁶ With the help of endogenous enzymes, VdU firstly inserted into the genome of replicating cells, then the added fluorescent tetrazine reacted with VdU-modified DNA and eventually lit up the strands. Compared with 5-ethynyl-2'-deoxyuridine (EdU) that is a widely used DNA reporter based on alkyne–azide click reactions, VdU showed several remarkable advantages, such as reduced genotoxicity (Fig. 2b-II), faster reaction, high resolution and potential multicolor labelling of DNA duplication (Fig. 2b-III). This bioorthogonal iEDDA paves the way to explore alternative bioorthogonal reporters for the cellular nucleic acids.

Compared with “Always On” and “Turn-Off” probes, “Turn-On” probes have the lowest background noise and are always preferred. “Turn-On” probes need to remain “off” before turning on at the sites of action. Liang *et al.* designed a single quenched small molecule probe Cys(StBu)-Lys(GlyLys(DABCYL)-Gly-Gly-Arg-Arg-Val-Arg-Gly-FITC)-CBT (12) (induced by fluorescence resonance energy transfer (FRET) effect) which contained four key components: (1) a disulfided cysteine (Cys) and a CBT motif for reduction-triggered CBT-Cys condensation; (2) a DABCYL unit as a

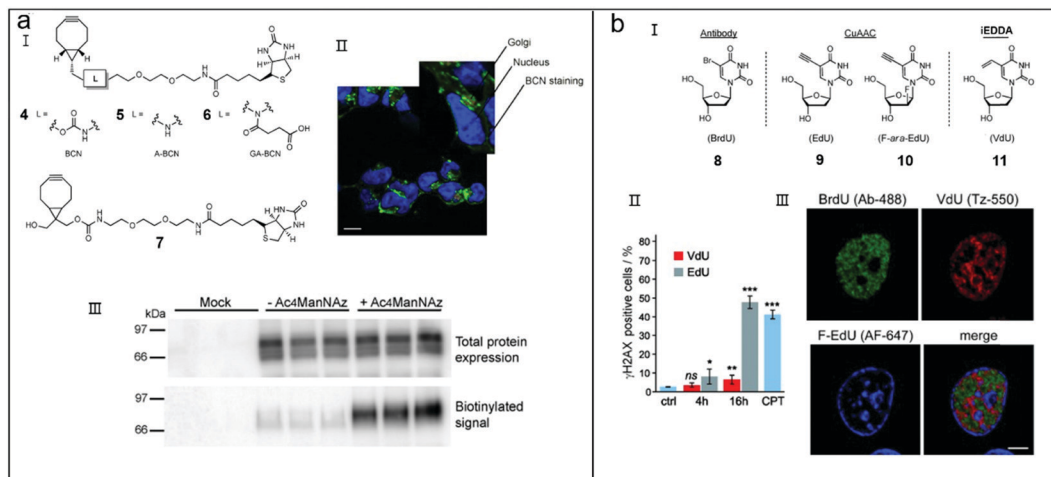


Fig. 2 (a) Bioorthogonal reactions involving polar bicyclononynes for cell imaging. (I) Structures of polar bicyclononynes. (II) Confocal laser scanning microscopy (CLSM) image of HEK293 cells after treatment with 5. (III) Western blots of the TRPV5 channel of HEK293 cells after treatment with 5 (CPT: camptothecin). Scale bar: 10 μm . Reproduced with the permission from ref. 125. Copyright 2014, Wiley-VCH Verlag GmbH & Co. KGaA, Weinheim. (b) Alkene-tetrazine click reaction for DNA imaging. (I) Structures of thymidine analogues applied to metabolically label cellular DNA. (II) γH2AX assay of HeLa cells after different treatments. (III) Images of a cell at different stages of S-phase after the treatment of different thymidine analogues. Scale bar: 5 μm . Reproduced with the permission from ref. 126. Copyright 2014, Wiley-VCH Verlag GmbH & Co. KGaA, Weinheim.

fluorescence quencher of FITC; (3) an Arg-Arg-Val-Arg tetrapeptide specific to furin; (4) an Gly-Gly dipeptide to avoid the steric effect of furin cleavage (Fig. 3a-I).¹²⁷ After the reduction-triggered condensation reaction, 12 quickly self-assembled into nanoparticles

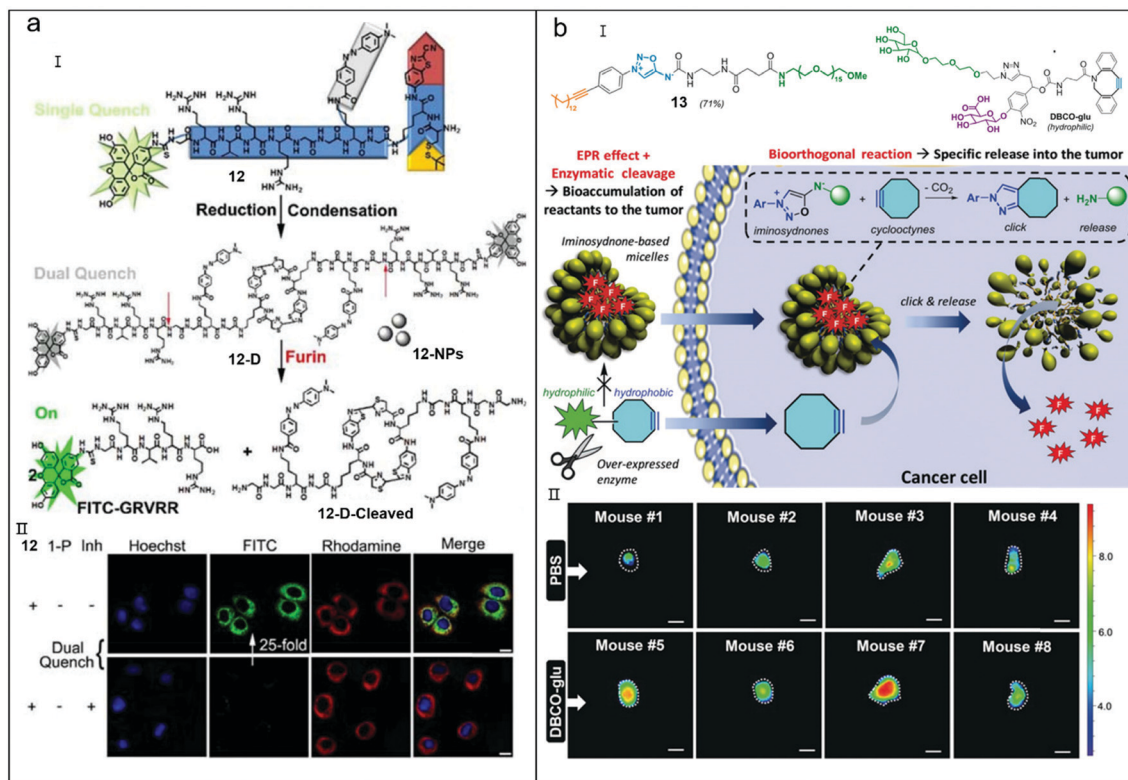


Fig. 3 (a) Dual-quenching system applied to detect cellular furin. (I) Imaging mechanism of dual-quenching system. (II) CLSM images of MDA-MB-468 cells after different treatments (1-P: single quenched control probe; Inh: furin inhibitor). Scale bar: 10 μm . Reproduced with the permission from ref. 127. Copyright 2018, American Chemical Society. (b) SPICC system applied to image tumor cells. (I) Imaging mechanism of SPICC system. (II) *Ex vivo* images of tumors after different treatments. Scale bar: 1 cm. Reproduced with the permission from ref. 129. Copyright 2019, Wiley-VCH Verlag GmbH & Co. KGaA, Weinheim.

(12-NPs) which was a dual-quenched probe caused by the FRET and aggregation-caused quenching (ACQ) effects. After the proteolysis of furin, the dual-quenched FITC was released from 12-NPs followed by the immediate fluorescence recovery. Because furin is overexpressed in tumor,¹²⁸ sensitive readouts of furin using probe 12 provides a feasible strategy for the accurate diagnosis of cancers. After treatment with 12, the fluorescence of MDA-MB-468 cells became apparent and reached its maximum at 2 h, indicating that cascade uptake, immediate reduction-triggered condensation and quick collapse of 12-NPs effectively occurred in tumor cells. Furthermore, the green fluorescence of FITC overlapped well with the red fluorescence of Rhodamine, confirming that the recovery of green fluorescence was initiated by intracellular furin (Fig. 3a-II). Because the Arg-Arg-Val-Arg substrate in probe 12 can be replaced by other enzyme-cleavable polypeptides, this “Turn-On” probe can serve as a template to design other smart imaging probes for accurate cancer diagnosis.

While some works based on bioorthogonal cleavage reactions have significantly improved therapeutic effect *in vitro*, the goal of designing two-component bioorthogonal systems that can be efficiently applied in the complex living systems are still challenging. Taran *et al.* presented a strategy which promoted the bioorthogonal disassembly of smart micelles inside tumor tissues following a programmed mode (Fig. 3b-I).¹²⁹ Strain-promoted iminosydnone-cycloalkyne cycloaddition (SPICC) was utilized to construct bioorthogonal system. For instance, an iminosydnone unit was introduced into a cleavable amphiphile 13 while a cycloalkyne group was introduced into a β -glucuronidase-responsive pro-activator (DBCO-glu). Without β -glucuronidase, there was extremely weak red fluorescence in the cytoplasm of KB cells, indicating that DBCO-glu hardly induced the disassembly of micelles. On the contrary, the fluorescence was significantly lit up in the presence of β -glucuronidase, demonstrating the vital role of β -glucuronidase in the decomposition of the micelles. As expected, the

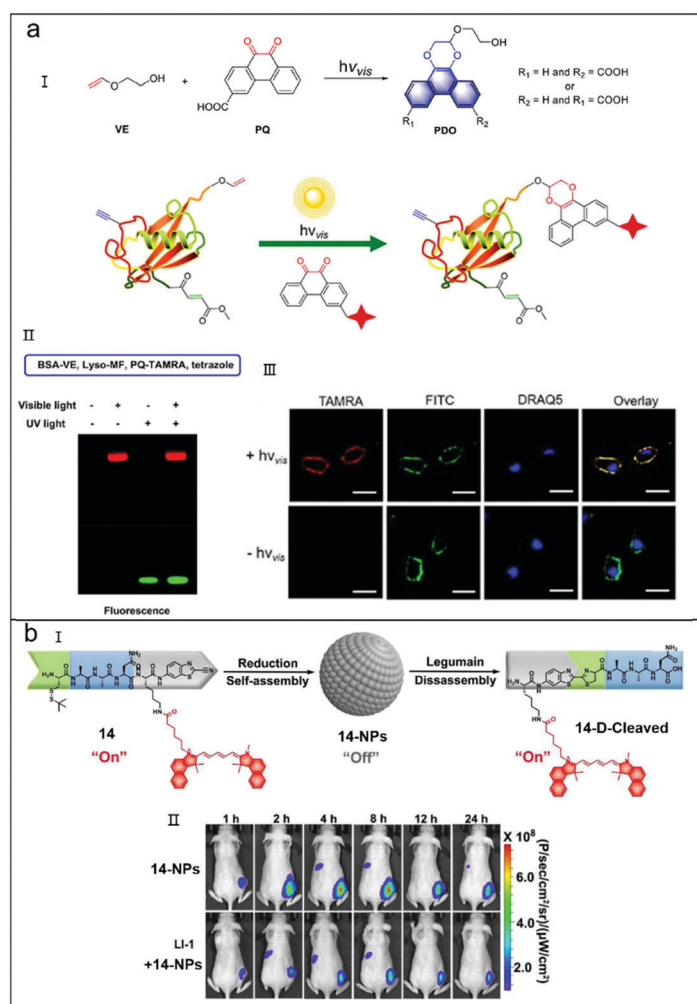


Fig. 4 (a) A visible light-triggered PQ/VE cycloaddition to label DNA. (I) Imaging mechanism of PQ/VE system. (II) Fluorescent labelling results of different bioorthogonal reactions. (III) CLSM images of A549 cells after different treatments. Scale bar: 50 μ m. Reproduced with the permission from ref. 130. Copyright 2018, American Chemical Society. (b) Legumain-specific NIR fluorescent switch for tumor imaging. (I) Imaging mechanism of legumain-specific NIR fluorescent switch. (II) *In vivo* time-lapse fluorescence imaging of mice after different treatment (LI-1: a specific inhibitor of legumain). Reproduced with the permission from ref. 133. Copyright 2018, American Chemical Society.

intensity of red fluorescence in tumors in the M5-DiR + DBCO-glu group was the strongest, indicating the decomposition of micelles was triggered by a cascade enzymatic and bioorthogonal cleavage reactions inside the tumor (Fig. 3b-II). Such approaches based on bioorthogonal cleavage reactions are brilliant candidates for the delivery of drugs to lesions in a controllable and precise manner, which is very important for disease diagnosis and therapy.

Bioorthogonal reactions triggered by light are highly demanded in biological studies. However, the current photoclick chemistry is usually based on UV light and has cross reactions under complex biological environments. Hence, a new visible light-catalyzed bioorthogonal reaction which can efficiently proceed in biological environment is urgently needed. Zhang *et al.* reported a visible light-triggered bioorthogonal cycloaddition to orthogonally label specific proteins (Fig. 4a-I).¹³⁰ The bioorthogonal [4+2] cycloaddition between 9,10-phenanthrenequinone (PQ) groups and electron-rich vinyl ether (VE) groups generated a fluorescent phenanthrodioxine (PDO) cycloadduct. In a mixture of tetrazole, PQ-TAMRA (PQ labelled with tamra), BSA-VE (bovine serum albumin labelled with VE) and Lyso-MF (lysozyme labelled with monomethyl fumarate), Lyso and/or BSA could be selectively labelled by green fluorescence emitted from pyrazoline and/or red fluorescence emitted from TAMRA upon irradiation with mild UV light and/or a hand-held LED lamp (Fig. 4a-II), suggesting VE and PQ did not crossly react with other bioorthogonal groups. After irradiation with visible light, there were obvious colocalized red fluorescence and green fluorescence on the surfaces of tumor cells in cetuximab-VE/FITC + PQ-TAMRA group, confirming that PQ-VE photocycloaddition successfully proceeded in living tumor cells (Fig. 4a-III). Because PQ-VE photocycloaddition-triggered cell labelling can be temporally and spatially controlled by the visible light, this bioorthogonal reaction opens the door to more precise biological applications.

Legumain is a kind of cysteine protease, which mainly exists in the lysosomes and plays a key role in the catabolic process of proteins. The overexpression of legumain is closely related with certain malignant cancers, *e.g.* breast cancer, colon carcinoma and prostate cancer.¹³¹ In addition, the level of legumain in tumor reflects the degree of cancer progression.¹³² Inspired by the indication function of legumain, Liang *et al.* designed a smart NIR probe 14 which contained three parts: (1) a CBT moiety and a Cys moiety for CBT-Cys click reaction; (2) a Ala-Ala-Asn (AAN) tripeptide which is specific to legumain; (3) a Cy5.5 chromophore for NIR imaging (Fig. 4b-I).¹³³ After the reduction of disulfide bond, 14 proceeded a CBT-Cys condensation reaction and self-assembled into the nanoprobe (14-NPs), in which NIR fluorescence of Cy5.5 was quenched due to the ACQ effect. Upon internalization into cancer cells, the tripeptide structure in 14-NPs was cut off by legumain, leading to the collapse of 14-NPs and the *in situ* recovery of the NIR fluorescence (Fig. 4b-II). As a result, this smart probe shows the potentials in diagnosis of legumain-associated cancers.

Due to their innate merits including low background, deep tissue penetration and effective solid-state emission,

aggregation-induced emission (AIE) luminogens (AIEgens) with NIR fluorescence have been used in diversified fields, *e.g.* biomedical engineering and optoelectronics. In the quest for the easily available and functional NIR imaging probes, Tang *et al.* introduced tetraphenylethene (TPE) and thiophene units to both sides of spiro-benzo[*d*]imidazole-2,1'-cyclohexane (BI), generating a donor-acceptor (D-A) architecture (2TPE-2T-BI) with high quantum yield, large Stokes shift and AIE luminescent property (Fig. 5a-I).¹³⁴ After coating DSPE-PEG-DBCO and DSPE-PEG on 2TPE-2T-BI, DBCO-AIEdots were obtained, in which DSPE and 2TPE-2T-BI formed the hydrophobic core while PEG formed the hydrophilic outer layer. MCF-7 cells pretreated with Ac₄ManNAz displayed strong red fluorescence after incubation with DBCO-AIEdots, demonstrating the combination of Ac₄ManNAz and DBCO-AIEdots efficiently lit up tumor cells. The red fluorescence signal in Ac₄ManNAz-pretreated mice was almost located at tumor sites *in vivo* (Fig. 5a-II), while the fluorescence spread all over the body in PBS pretreated group, suggesting bioorthogonal click reactions enhanced the accumulation of DBCO-AIEdots in tumors. Benefiting from their good biocompatibility and superior optical performances, these AIE dots have enormous potentials in imaging-guided PDT, PTT and drug delivery. Recently, another type of bioorthogonal AIE dot was developed, in which a NIR AIEgen (2TPE-4E) was encapsulated by DBCO-PEG-lipids (Fig. 5a-III).¹³⁵ The polyyne bridge moiety in 2TPE-4E not only extended the π -conjugated system but also avoided the ACQ effect. Animal experiments confirmed that AIE dots selectively accumulated in tumor tissues with negligible organ toxicity by taking advantages of bioorthogonal click reaction and metabolic glycoengineering, suggesting AIE dots are eligible imaging probes for cancer diagnosis.

Due to the unparalleled advantages such as good biocompatibility, versatile cavity structure and conveniently genetical modifications, cell membrane vesicles (MVs) have received intensive attentions from various fields. By means of metabolic engineering, azide motifs can be anchored on the cell membrane (CM) and act as the artificial receptors which can undergo bioorthogonal click reactions.¹³⁶ In acidic conditions, vesicular stomatitis virus G-protein (VSVG) enables the fusion of adjacent cells, thus the heterogeneity of acceptors on the tumor cells can be efficiently overcome. Based on these ideas, Liu *et al.* prepared N₃-anchored mimovirus vesicles (MVs-N₃) from VSVG overexpressing HEK293T cells.¹³⁷ Attributing to the fusion function of VSVG protein, MVs-N₃ were able to selectively aggregate in tumor and underwent a low-pH fusion with tumor cells (Fig. 5b-I). By conjugating with different kinds of DBCO-modified imaging agents on the surfaces of fused tumor cells, multiple targeted theranostic strategies can be realized for malignant tumors. The red fluorescence signal of DBCO-Cy5 around tumor cells at pH 6.0 was much stronger than that at pH 7.4, indicating MVs-N₃ possessed an outstanding capability to fuse with tumor cell membrane in a weak acid environment. 4T1 or MCF-7 bearing mice treated with MVs-N₃ also showed the strongest fluorescent intensity (Fig. 5b-II), suggesting that smart MVs-N₃ were able to deliver VSVG protein and bioorthogonal N₃

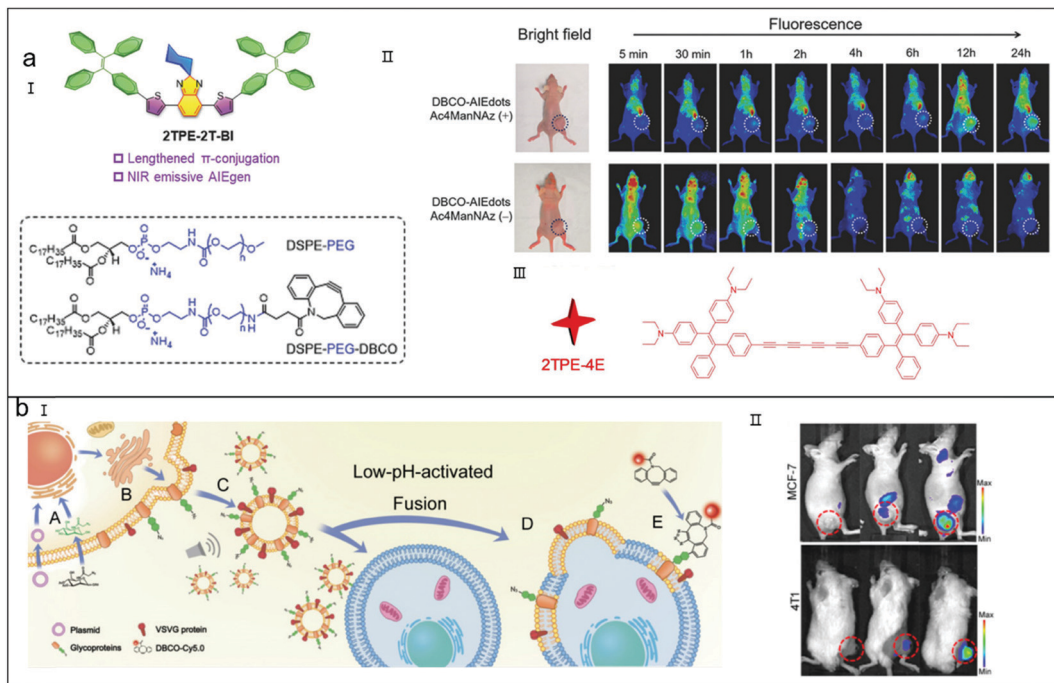


Fig. 5 (a) NIR AIEgens for tumor imaging *in vivo*. (I) Structures of 2TPE-2T-BI AIEgen, DSPE-PEG and DSPE-PEG-DBCO. (II) *In vivo* time-lapse fluorescence imaging of mice after different treatment. (III) Structure of 2TPE-4E AIEgen. Reproduced with the permission from ref. 134. Copyright 2018, Wiley-VCH Verlag GmbH & Co. KGaA, Weinheim. (b) Mimovirus vesicle-based cancer diagnosis. (I) Imaging mechanism of mimovirus vesicle. (II) *In vivo* FL images of MCF-7/4T1 tumor-bearing mice after different treatments. Reproduced with the permission from ref. 137. Copyright 2020 Wiley-VCH Verlag GmbH & Co. KGaA, Weinheim.

moieties to tumor tissues, which efficiently overcomes the barriers of tumor heterogeneity. If imaging agent DBCO-Cy5 was replaced by DBCO-liposomes/indocyanine green (ICG) or DBCO-SPION (superparamagnetic iron oxide nanoparticles), accurate fluorescence imaging could also be acquired, confirming this targeting imaging method was a versatile strategy for cancer diagnosis.

Although the “click-to-release” strategy occupies an important position in the fields of *in situ* drug activation and fluorescence recovery of imaging agent, it is still urgent to develop excellent bioorthogonal molecules with fast reaction kinetics and good pharmacokinetics. Bernardes *et al.* developed a pretargeting strategy on the basis of TCO/Tz bioorthogonal decaying reaction for activation of probe/drug at tumor sites (Fig. 6a-I).¹³⁸ In pretargeting strategy, tetrazine-modified single-walled carbon nanotubes (TZ@SWCNTs) and TCO-containing complementary molecules, such as TCO-carbamate hemicyanine (tHCA) and TCO-carbamate DOX (tDOX), were designed for NIR imaging and cancer therapy. TZ@SWCNTs were firstly administrated and allowed to fully accumulate in tumor tissues with the assistance of the EPR effect. Then tHCA or tDOX was administrated and quickly accomplished “click-to-release” reaction *in situ* to activate probe or active drug. After modification, the cytotoxicity of tDOX was reduced by over one hundred times. However, the cytotoxicity was largely recovered with the help of TZ@SWCNTs, demonstrating this strategy improved the safety and selectivity of cancer chemotherapy. CT26 tumor-bearing mice pretreated with TZ@SWCNTs showed an obvious signal in the belly at 1.5 h post injection of tHCA, and this

signal became invisible at 3 h. Meanwhile, the fluorescence gradually became visible at tumor site at 3 h and further increased during a period of 24 h (Fig. 6a-II), suggesting HCA were successfully released in the Tz-labelled tumors. It is worthy note that this strategy needs smaller dose of tetrazine derivatives than conventional methods owing to the tumor-targeted transportation of TZ@SWCNTs. In addition, the interval time in this pretargeting strategy was also much shorter than other TCO/Tz-based activation strategies due to the fast clearance of TZ@SWCNTs. Based on these excellent performances, this pretargeting activation strategy will provide important value to the existing targeting strategies for cancer diagnosis and treatment.

Tetrazine bioorthogonal probes emitting NIR fluorescence are in urgent demand for *in vivo* bioimaging applications. Wu *et al.* synthesized a serial of tetrazine-containing NIR “Huaxi-Fluors” (HFs) whose fluorescence were enhanced hundreds of times after BCN/Tz bioorthogonal reactions. HFs were characterized with large Stokes shifts, high S/N ratio and low photo-bleaching.¹³⁹ Tumor cells pretreated with BCN-modified conjugates (such as BCN-cetuximab, BCN-morpholine and BCN-triphenylphosphonium) followed by HFs, were all efficiently lit up at their target sites without washing step, such as cell surface (BCN-cetuximab group), lysosomes (BCN-morpholine group) and mitochondria (BCN-triphenylphosphonium group), suggesting these HFs served as excellent NIR probes with high S/N ratio in living systems. The NIR fluorescence of tumor tissues in the HF probe group was significantly stronger than that in control groups. Moreover, the

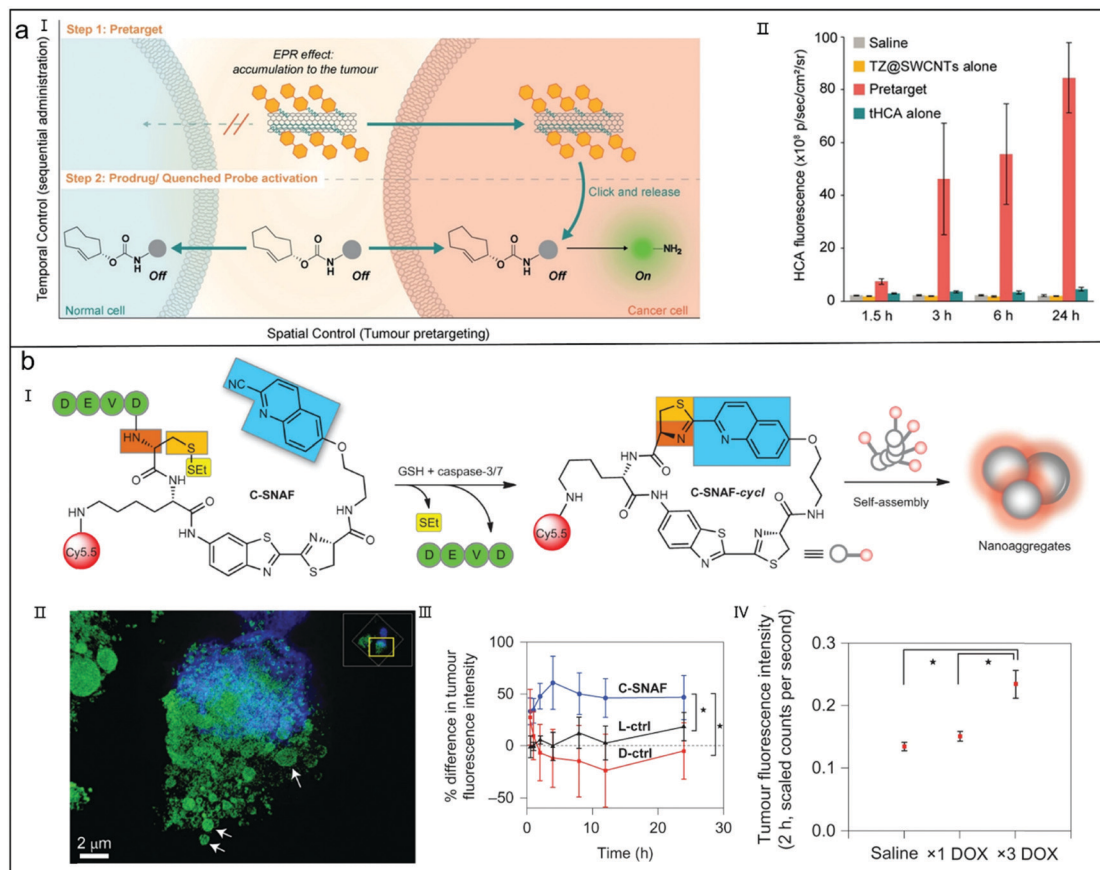


Fig. 6 (a) Bioorthogonal carbon nanotubes for tumor imaging. (I) Imaging mechanism of bioorthogonal carbon nanotubes. (II) Time-lapse NIR fluorescence intensity of tumor after different treatments. Reproduced with the permission from ref. 138. Copyright 2020, Wiley-VCH Verlag GmbH & Co. KGaA, Weinheim. (b) Bioorthogonal nanoaggregates for detecting caspase activity. (I) Imaging mechanism of nanoaggregates. (II) CLSM image of apoptotic cells treated with C-SNAF-SIM. (III) The % difference in tumor fluorescence intensity over the course of imaging for C-SNAF, L-ctrl and D-ctrl. (IV) A comparison of tumor fluorescence intensity at 2 h after treatment with C-SNAF in different groups. Reproduced with the permission from ref. 143. Copyright 2014, Nature Publishing Group.

fluorescence signal could reach as deep as 500 μm in tumor, suggesting HFIs have great potential for deeply intravital imaging.

To assess the therapeutic efficacy and selectivity of anti-cancer drugs, real-time monitoring of tumor apoptosis may be an effective method. Because apoptotic proteins, such as caspase-3 and caspase-7, are closely related to cell apoptosis,^{140–142} Rao *et al.* designed a caspase-3/7-sensitive probe C-SNAF which could real-time monitor the apoptosis of tumor cells (Fig. 6b-I).¹⁴³ The probe C-SNAF consisted of a disulfide bond for thiol-involved reduction, a _L-DEVD sequence for caspase-3/7-specific cleavage, as well as a 2-cyano-6-hydroxyquinoline (CHQ) and a _D-cysteine group for bioorthogonal reactions. Good membrane permeability of the probes and abundant caspase-3/7 in apoptotic tumor cells together induced the intramolecular bioorthogonal condensation and the formation of macrocycle C-SNAF-cycl. Owing to the hydrophobic interactions and π–π stacking, C-SNAF-cycl self-assembled into nanoaggregates which acted as excellent imaging contrasts for apoptotic tumor cells. Upon treatment with C-SNAF-SIM, strong green fluorescent nanoaggregates could be observed all over the cytosol or tumor tissues pretreated with apoptotic drugs, demonstrating that caspase-3/7 induced the

formation of nanoaggregates in living systems (Fig. 6b-II). The fluorescence signal in apoptotic drug-treated tumor was obviously higher than the control groups (Fig. 6b-III), and was proportionate to the caspase-3/7 activity, suggesting that C-SNAF probes specifically labelled the apoptotic tumors. Interestingly, the fluorescence in tumor was weak after one round of apoptotic drug injection, while explosively increased after three rounds of administration (Fig. 6b-IV), suggesting C-SNAF accurately reported the real-time chemotherapeutic efficacy at different treatment stages. Hence, C-SNAF probes are able to provide useful and instant feedback information for cancer treatment.

2.2 Metal-free bioorthogonal click chemistry for magnetic resonance imaging (MRI)

It is well known that glycosylation plays an important role in intercellular communication and cell migration. Although some techniques have been applied in glycosylation imaging *in vitro*, dynamic and in-depth imaging of glycans *in vivo* is challenging. Based on metabolic glycoengineering (*N*-azidoacetyl-galactosamine, Ac₄GalNAz, **15**) and a gadolinium-involving

bioorthogonal MRI probe (TMDIBO-Lys-Gd, **16**), Neves *et al.* realized *in vivo* imaging of glycosylated tissues (Fig. 7a-I).¹⁴⁴ Probe **16** consisted of a DBCO moiety, a hydrophilic lysine linker and a clinically approved gadolinium-involving DOTA chelator. By feat of the metabolic labelling and bioorthogonal reaction strategy, high gadolinium content and distinct MRI signals (Fig. 7a-II) were detected in tumor, liver and kidney tissues. However, without Ac₄GalNAz pretreatment, these signals were low, suggesting the glycosylated tissues were accurately imaged by the designed strategy. As surface glycan plays a vital role in living systems, this glycosylation-based bioorthogonal system has promising potentials in realizing the fast and non-invasive MRI of glycosylated tissues in preclinical models of multiple diseases.

To overcome the problem of severe side effects in radiotherapy, pretargeting strategies usually containing the primary targeting agents and the secondary imaging agents are proposed. Due to their impressive reaction kinetics and high selectivity, bioorthogonal reactions have been considered as the ideal reactions to connect the primary targeting agents and the secondary imaging agents in living systems. Herth *et al.* constructed a series of TCO-decorated polypeptide-graft-polypeptoid copolymers (PeptoBrushes 17–19) with core-shell structures to significantly prolong the half-life of TCO moieties *via* the shielding effect (Fig. 7b-I).¹⁴⁵ Attributing to the EPR effect of PeptoBrushes, obvious signals were detected in tumors at 2 h post injection *in vivo*, which could significantly promote the clinical translation of the nanoparticles by decreasing

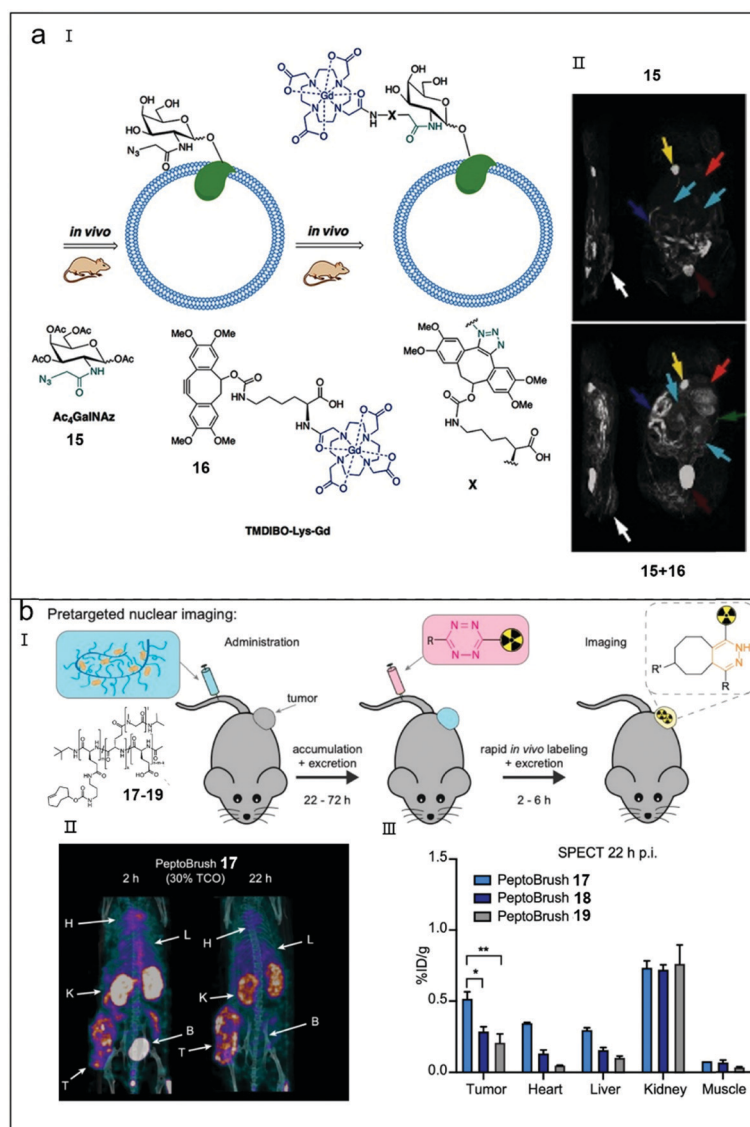


Fig. 7 (a) Synergy of metabolic labelling and MRI for glycosylation imaging *in vivo*. (I) Illustration of glycans labelling strategy. (II) T_1 -weighted MRI of mice after different treatments. Reproduced with the permission from ref. 144. Copyright 2015, Wiley-VCH Verlag GmbH & Co. KGaA, Weinheim. (b) Pretargeted nuclear imaging based on DBCO/Tz ligation reaction. (I) Illustration of pretargeted nuclear imaging strategy. (II) SPECT/CT images obtained from mice assigned in pretargeted imaging group. (III) Image derived uptake values in tumors and main organs. Reproduced with the permission from ref. 145. Copyright 2019, American Chemical Society.

expenses and reducing the risk of nonscheduled treatment protocols (Fig. 7b-II). Interestingly, the accumulation of PeptoBrushes in tumors and other organs remained at a low level throughout the study (Fig. 7b-III). This may be attributed to the less available radiolabelled PeptoBrushes in the blood for the EPR-promoted tumor accumulation due to the low injected dose of imaging agents, thus no huge increase of uptake was monitored in tumor with the extension of time. Although the tumor uptake became low, imaging contrast was obviously improved at the early imaging point, which provided a great superiority for PeptoBrushes nanomedicines to be applied in pretargeted nuclear imaging.

For cancer diagnostic application, ^1H MRI usually owns the high sensitivity but low selectivity due to the large amount of water molecules inside the tissues. On the contrary, ^{19}F MRI has compromised sensitivity but high selectivity because

^{19}F can easily accumulate in tumor tissues. Hence, integrating the high selectivity of ^{19}F MRI and the superior sensitivity of ^1H MRI undoubtedly can improve the diagnosis accuracy of tumor. By conjugating TFMB-Arg-Val-Arg-Arg-Cys(StBu)-Lys-CBT (20) onto Fe_3O_4 nanoparticle (IONP) *via* amido linkage, Liang *et al.* constructed a probe with ^1H MRI and ^{19}F MRI abilities (IONP@20) (Fig. 8a-I).¹⁴⁶ Owing to the paramagnetic relaxation enhancement (PRE) effect, ^{19}F MRI of IONP@20 was quenched at first. However, under the catalysis of furin, TFMB-Arg-Val-Arg-Arg moiety in 20 was cut off and then the signal of ^{19}F MRI recovered. Simultaneously, bioorthogonal CBT-Cys click reactions among IONP@20 residues were initiated by GSH, which eventually led to the formation of cross-linked IONPs. Attributing to the aggregation of IONP, R_2 of ambient water molecules was elevated and T_2 MRI signal was significantly enhanced. Thus, this smart IONP@20 probe with furin

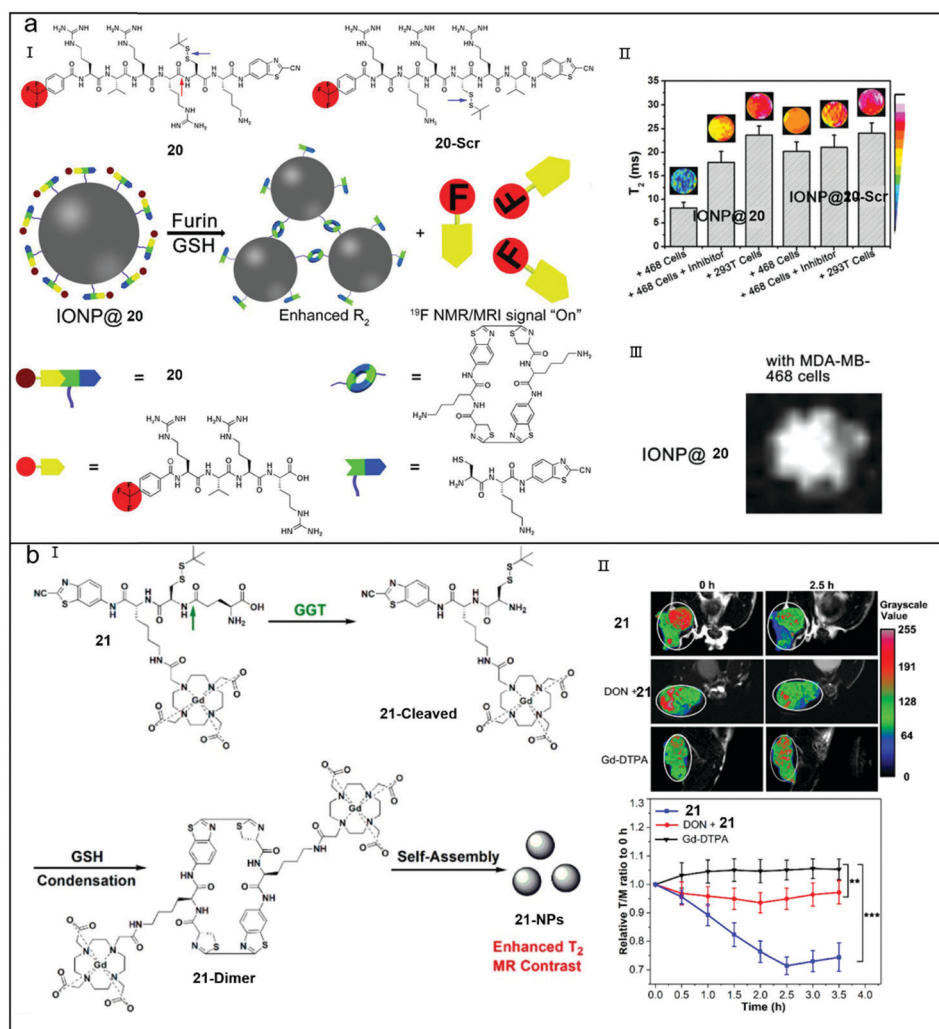


Fig. 8 (a) Furin-triggered NP aggregation to enhance ^{19}F and ^1H MRI *in vivo*. (I) ^{19}F and ^1H MRI mechanism of furin-triggered NP aggregation. (II) T_2 images and T_2 values of IONP@20-Scr and IONP@20 after incubation with different cells. (III) ^{19}F MR image of IONP@20 after incubation with MDA-MB-468 cells. Reproduced with the permission from ref. 146. Copyright 2019, Wiley-VCH Verlag GmbH & Co. KGaA, Weinheim. (b) GGT-triggered Gd-based contrast agent to improve T_2 -weighted MRI of tumors *in vivo*. (I) T_2 -weighted MRI mechanism of GGT-initiated Gd-based contrast agent. (II) T_2 MR images of mice bearing HeLa tumor after different treatments (upside) and T/M (tumor-to-muscle) ratio analysis of T_2 values in different groups (below). Reproduced with the permission from ref. 147. Copyright 2019, American Chemical Society.

and GSH dual-responsiveness realized accurate imaging of tumors. Widespread IONP aggregates appeared in Golgi bodies of MDAMB-468 cells overexpressing furin and significantly enhanced ^1H MRI signals were observed after the treatment with IONP@20 (Fig. 8a-II). Meanwhile, ^{19}F MRI signals were switched on (Fig. 8a-III), to detect furin activity of tumor cells. As expected, the signals of T_2 MRI and ^{19}F MRI of tumors were also augmented in the IONP@20 group, indicating that smart PRE effect and furin-induced IONP aggregation led to precise dual-MRI of tumor. After ingenious modification, this dual-responsive probe shows the potentials for precise ^1H and ^{19}F MRI of tumor in bigger rodents in the near future.

Gd-based MRI contrast agents (CAs) routinely serve as T_1 -dominated CAs. Latest research reported that Gd-based nanostructures could also be employed as T_2 -weighted CAs at high magnetic field. However, the Gd-based nanoparticles *in situ* formed in cells have not been used to improve the *in vivo* T_2 -weighted MRI of tumors at high magnetic field. Liang *et al.* designed a Gd-based MRI probe which self-assembled into nanoparticles in the presence of γ -glutamyltranspeptidase (GGT), resulting in the enhanced T_2 -weighted MRI of tumors at high magnetic field (Fig. 8b-I).¹⁴⁷ Under the catalysis of GGT on the cell membrane, the Glu moiety in 21 was cut off and 21-Cleaved was generated. Intracellular GSH then cleaved the disulfide bond of 21-Cleaved and CBT-Cys condensation among the residues of 21-Cleaved smoothly occurred to form 21-Dimer. Attributed to the π - π stacking, the amphiphilic 21-Dimer self-assembled into Gd-based nanoparticles (21-NPs) inside tumor cells, which owned enhanced T_2 -weighted MRI ability at high magnetic field. The T_2 value of tumors in the 21 group reached its maximum at 2.5 h post injection, but the T_2 value of tumors in control groups increased very slightly (Fig. 8b-II), suggesting GGT-triggered intracellular 21-NPs contributed to the increased T_2 MR contrast of solid tumors. When high magnetic field is permissible in clinic, this T_2 -weighted MRI probe can be employed to diagnose GGT-related malignancy in the future.

2.3 Metal-free bioorthogonal click chemistry for photoacoustic imaging (PAI)

Due to the existence of blood brain tumor barrier (BBTB), blood brain barrier (BBB) and intricate brain tumor microenvironment, the development of new imaging method for brain tumors has been hindered by the low delivery efficiency of contrast agents. Liu *et al.* constructed a multimodal imaging contrast agent cRGD-CM-CPIO to escape the barriers of brain tumors (Fig. 9a-I).¹⁴⁸ To obtain cRGD-CM, CM was firstly labelled with large numbers of azide groups by means of metabolic glycoengineering. Then, cRGD was conjugated onto CM through the bioorthogonal azide/BCN click reaction. CPIO consisted of ultrasmall IONPs and a diketopyrrolopyrrole (DPP)-based conjugated polymer (CP). The brain tumor-bearing mice treated with cRGD-CM-CPIO showed a higher fluorescence outcome than those injected with CM-CPIO, implying the higher tumor targeting efficiency of cRGD-CM coating than CM coating. MRI displayed the similar results as the FI (Fig. 9a-II). PAI showed that cRGD-CM-CPIO overlaid the whole cross-section of brain

tumor, while CM-CPIO only located at the superficial layer of brain tumor (Fig. 9a-III), demonstrating that cRGD-CM-CPIO overcame the barriers of BBB and BBTB. This study provides a good example of bioorthogonal CM as a potential theranostic approach to overcome the delivery barriers existing in brain tumors.

Due to the high spatial resolution, PAI is preferred in diagnosing superficial cancers. Although various PA agents have been designed, a smart enzyme-activatable probe that can enhance the PA signal of tumor tissues has not been reported. Liang *et al.* reported a NIR probe IR775-PhePhe-Tyr(H_2PO_3)-OH (1P) to improve PA imaging of alkaline phosphatase (ALP) at cellular level and in animals (Fig. 9b-I).¹⁴⁹ Under the catalysis of ALP in tumor tissues, 1P transformed into hydrophobic IR775-Phe-Phe-Tyr-OH (22) which self-assembled into nanoparticles (22-NPs) in tumor cells after endocytosis. Formation of nanoparticles quenched the NIR fluorescence of the probe but enhanced its PA imaging ability. PA signals in ALP-overexpressing HeLa tumors were much stronger than those in the ALP inhibitor-treated groups (Fig. 9b-II), indicating ALP played a key role in enhancing the PA signal of tumors. In contrast, PA signal in muscle tissues was very low, suggesting that 1P probe was able to selectively activate PA signals at tumor sites. Because different levels of ALP were expressed at different proliferative and differentiative stages of tumors, 1P was also able to precisely distinguish the progression of tumors. As the construction method of 1P is universal, more elaborately-designed PA probes can be constructed based on this method to precisely diagnose other difficult miscellaneous diseases.

2.4 Metal-free bioorthogonal click chemistry for positron emission tomography (PET) imaging and Raman imaging (RI)

Positron-emission tomography (PET) imaging is a clinical routine modality for cancer diagnosis owing to its high sensitivity. Because tumor cells are metabolically active, it is difficult to conduct precise PET imaging of specific tumor. Hence, tumor-targeted strategies are necessary to increase the selectivity of PET probes. Liang *et al.* synthesized a furin-initiated radiotracer Acetyl-Arg-Val-Arg-Arg-Cys(StBu)-Lys-(DOTA- ^{68}Ga)-CBT (CBT- ^{68}Ga) which could be co-injected with its cold analog CBT-Ga to enhance PET imaging of target tumors *in vivo*. In the presence of GSH and furin, CBT- ^{68}Ga successively underwent disulfide bond reduction and CBT-Cys bioorthogonal click reaction to form dimerization or trimerization which eventually self-assembled into CBT- ^{68}Ga nanoparticles (CBT- ^{68}Ga -NPs) (Fig. 9c-I).¹⁵⁰ Compared with the CBT- ^{68}Ga control group, stronger PET signal was observed in tumors at 1 h post injection of CBT-Ga + CBT- ^{68}Ga and the signal was observed even after 3 h (Fig. 9c-II), suggesting CBT- ^{68}Ga -NPs not only increased the accumulation of the radiotracers in tumor tissues but also improved the PET imaging of tumors. No pathological change was observed in main organs and tissues in the experimental group, suggesting the biocompatibility of CBT- ^{68}Ga probes was excellent. Hence, CBT- ^{68}Ga not only owns outstanding PET imaging

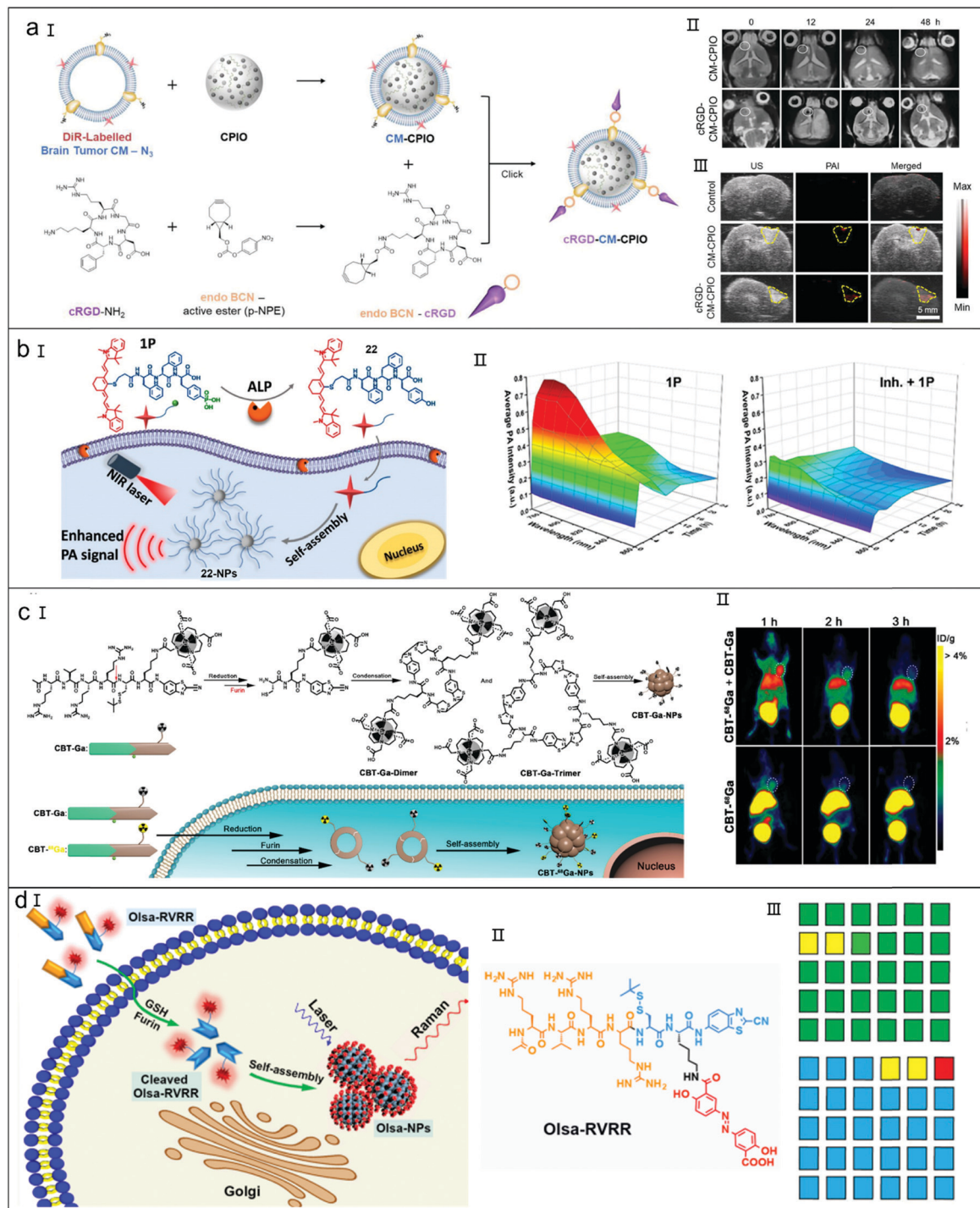


Fig. 9 (a) Biomimetic nanoparticles for brain tumor imaging. (I) Preparation route of cRGD-CM-CPIO nanoparticles. (II) MRI images of brain tumors after different treatment. (III) PAI images of brain tumors after different treatment. Reproduced with the permission from ref. 148. Copyright 2020 Wiley-VCH Verlag GmbH & Co. KGaA, Weinheim. (b) ALP-triggered NIR nanoparticle to enhance PA imaging of tumors *in vivo*. (I) PA imaging mechanism of ALP-triggered NIR nanoparticle. (II) 3D PA spectra of tumors *in vivo* after different treatments. Reproduced with the permission from ref. 149. Copyright 2018, American Chemical Society. (c) Furin-triggered ⁶⁸Ga-based nanoparticle to enhance PET imaging of tumors *in vivo*. (I) Imaging mechanism of furin-initiated ⁶⁸Ga nanoparticle. (II) PET images of mice bearing MDA-MB-468 tumor after different treatments. Reproduced with the permission from ref. 150. Copyright 2019, American Chemical Society. (d) Furin-triggered Olsa-NPs for Raman imaging of tumors. (I) Raman imaging mechanism of furin-triggered Olsa-NPs. (II) Structure of Olsa-PRVV. (III) Machine classification results of Raman spectra. Reproduced with the permission from ref. 151. Copyright 2021, Wiley-VCH Verlag GmbH & Co. KGaA, Weinheim.

capability but also has good biocompatibility, both of which are important for *in vivo* imaging.

Attributed to its high photostability and molecular specificity, Raman spectroscopy has been used to recognize tumour-genesis and progression, as well as to evaluate the therapeutic effect. However, the clinical use of Raman spectroscopy is still limited because there are severe signal interferences from cellular or tissue matrix. Therefore, a targeted Raman imaging agent is urgently desired to detect tumor progression. Bulte *et al.* designed a new Raman reporter (Olsa-RVRR) which could specifically emit distinct Raman signals in furin-overexpressing tumor cells (Fig. 9d-I and -II).¹⁵¹ After being internalized by tumor cells overexpressing furin, Olsa-RVRR transformed into the hydrophobic oligomers under GSH reduction and furin cleavage. Then the driving forces of supramolecular interactions forced oligomers to self-assemble into Olsa-NPs which not only increased the cellular concentration of Olsa but also prolonged the retention time of drugs in tumor cells. The Raman signal accurately distinguished Olsa-RVRR treated tumors from others in control groups (Fig. 9d-III), confirming the specific accumulation of Olsa-NPs enhanced the Raman signal of tumor tissues. As olsalazine (Olsa) is an efficient DNA methylation inhibitor, Olsa-RVRR may serve as a new cancer theranostic platform in which Raman imaging acts as diagnostic method and Olsa works as chemotherapeutic agent.

3. Metal-free bioorthogonal click chemistry for cancer therapy

3.1 Metal-free bioorthogonal click chemistry for chemotherapy

Over the past decades, there existed several examples applying bioorthogonal reactions for prodrug activation at cellular level, while their *in vivo* utilizations were rare because of the off-target drug release and weakened reactivity of prodrugs caused by stereo-hindrance effect.¹⁵² Gamble *et al.* developed a new bioorthogonal prodrug activation strategy to explore their *in vivo* application (Fig. 10a, I).¹⁵³ Anticancer drug DOX was linked to an azide group through a self-eliminating linker *p*-aminobenzyloxycarbonyl (PABC), thus a prodrug **24** was formed. After azide/TCO bioorthogonal reactions (step 1–3), a fast 1,6-elimination reaction was induced by the acid-catalyzed imine hydrolysis, which led to the cleavage of PABC linker from the prodrug followed by a rapid drug release (step 4–5). Compared with free DOX, prodrug **24** showed a lower cytotoxicity. However, the cytotoxicity recovered after the addition of **25**, suggesting bioorthogonal reaction successfully helped release the active DOX (Fig. 10a-II). With the help of **25**, active **26** was rapidly released in mouse serum, indicating the rate of activation reaction was higher under physiological conditions, which was an excellent advantage for *in vivo* application. Notably, free **26** bound more serum proteins than prodrugs **24**, and **25** could slowly transform into its unreactive isomer CCO–OH. Although this activation strategy stays at the initial phase of the prodrug activation, it laid a solid foundation for

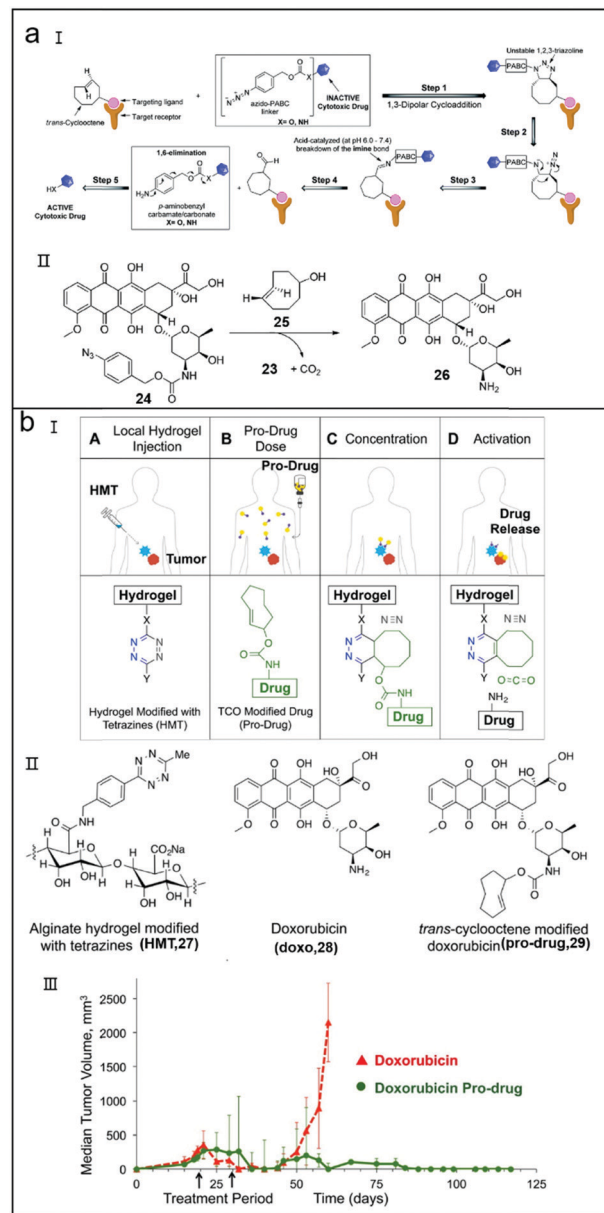


Fig. 10 (a) 1,3-dipolar cycloaddition system for prodrug activation. (I) The proposed mechanism of prodrug activation. (II) Structures of **23**, **24**, **25** and **26**. Reproduced with the permission from ref. 153. Copyright 2015, The Royal Society of Chemistry. (b) Prodrug activation strategy to treat STS. (I) Illustration of prodrug activation strategy. (II) Structures of **27**, **28** and **29**. (III) The change of tumor size during the therapy in different groups. Reproduced with the permission from ref. 156. Copyright 2016, American Chemical Society.

the future development of *in vivo* bioorthogonal activation or protection/deprotection applications.

Although nano-drug delivery systems have significantly reduced the side effects of free drugs, their therapeutic efficacy for soft tissue sarcoma (STS) is still poor because of the high heterogeneity of STS.^{154,155} Strategies are urgently needed to realize tumor-specific drug release for STS treatment. Royzen *et al.* reported a iEDDA reaction-based therapeutic strategy, in which small molecule prodrugs could be specifically activated

at tumor sites and ensured an effective therapeutic concentration of anticancer drug in tumor (Fig. 10b-I).¹⁵⁶ The pretargeted system consisted of an alginate hydrogel decorated with tetrazine groups (HMT) and a TCO-based prodrug (29) (Fig. 10b-II). After post-injected prodrugs reached the tumor site, the iEDDA reactions between tetrazine and TCO groups occurred and initiated the drugs release *in situ*. Attributed to the abundant tetrazine moieties on the hydrogel, small molecule prodrugs were concentrated at the tumor sites, making up for their suboptimal pharmacokinetics. Compared with control groups, the tumor volume remained undetectable throughout the experiment in prodrug groups (Fig. 10b-III), indicating active drugs were efficiently released from prodrugs *in vivo* and their anti-tumor activity was highly kept. This approach offers a new way for *in situ* concentrating anticancer drugs at targeted location without relying on the endogenous markers/bioactive molecules, and it holds an enormous potential to improve the clinical therapeutic effect of STS.

Metabolic glycoengineering acts as a useful tool to artificially anchor bioorthogonal groups onto the surfaces of cells. Nevertheless, selectively labelling the interesting cell types still remains challenging.^{157–159} Cheng *et al.* designed an unnatural sugar possessing an ability to selectively label tumor cells with azido moieties, providing convenience for the following bioorthogonal reaction-based targeting strategy (Fig. 11a-I).¹⁶⁰

To acquire high labelling specificity towards tumor cells, a histone deacetylase (HDAC)/cathepsin L (CTSL)-responsive Ac_4ManAz derivant (DCL-AAM) was constructed. After dual-enzyme hydrolysis, DCL-AAM underwent a structural rearrangement and quickly released the active $Ac_3ManAzOH$ to label cell membrane with N_3 groups (Fig. 11a-II). DBCO-doxorubicin prodrug (DBCO-VC-Dox) (Fig. 11a-III) was conjugated onto the N_3 -anchored cell membrane *via* the bioorthogonal chemistry and underwent the cathepsin B-mediated enzyme hydrolysis to release active DOX. The formulation of DCL-AAM + DBCO-VC-Dox significantly inhibited the tumor growth and prolonged the lifetime of mice in two cancer models (LS174T and MDA-MB-231 tumor models). In addition, bioorthogonal system significantly reduced lung metastasis and induced low systemic toxicity. This click chemistry-based tissue active targeting strategy (ATTACK) can be further developed using other sugar derivatives which respond to different endogenous bioactive molecules.

Owing to the large size and low stability, traditional antibody-drug conjugates (ADCs) encounter various problems, such as poor tissue penetration and unsatisfactory efficacy.^{161,162} Prodrug strategy in which the toxicity of drug is provisionally inhibited outside the cell but recovered in the cell, can be applied to improve the current ADCs. Chen *et al.* reported a prodrug-antibody conjugate (ProADC, TCO-Dox-Ab) that not only

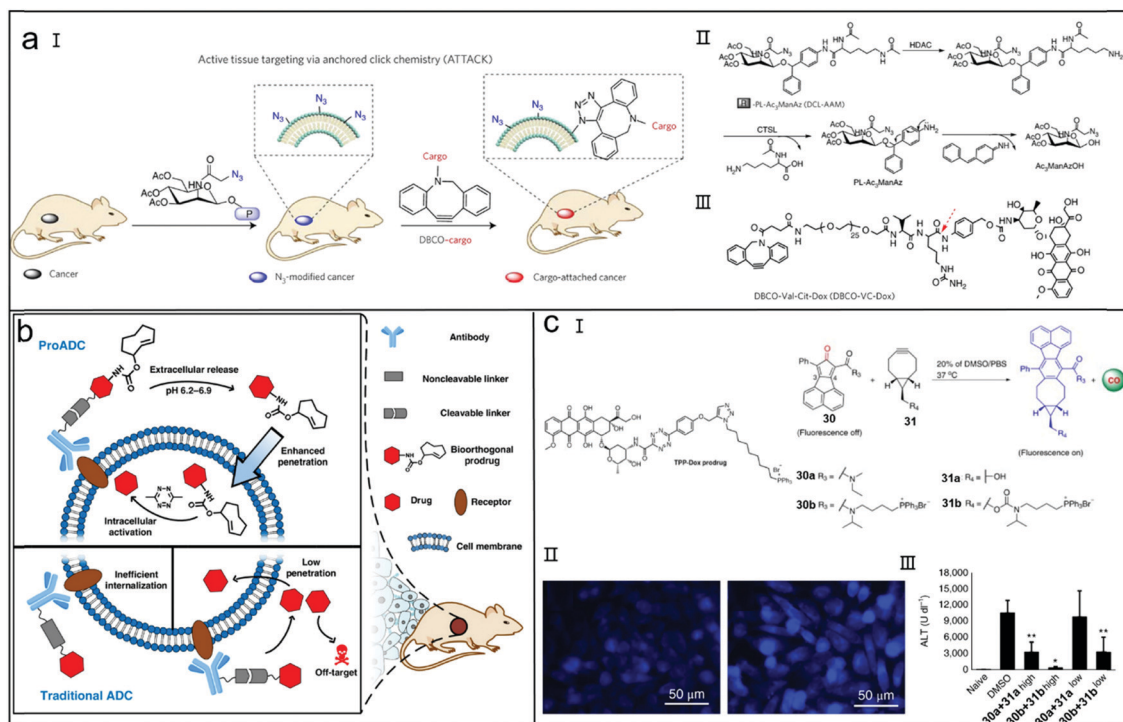


Fig. 11 (a) ATTACK strategy to enhance tumor accumulation of anticancer drugs. (I) Illustration of ATTACK strategy. (II) Degradable mechanism of DCL-AAM. (III) Structure of DBCO-VC-Dox. Reproduced with the permission from ref. 160. Copyright 2017, Nature Publishing Group. (b) The proposed mechanism of ProADC strategy. Reproduced with the permission from ref. 163. Copyright 2019, Chinese Chemical Society. (c) Enrichment-initiated prodrug activation strategy to enhance tumor accumulation of anticancer drugs. (I) Illustration of enrichment-initiated prodrug activation strategy. (II) CLSM images of RAW264.7 cells incubated with 30b (1 μ M) + 31b (1 μ M) (left) and 30b (5 μ M) + 31b (5 μ M) (right). (III) Serum ALT level of mice treated with acetaminophen followed by compounds 30a + 31a or 30b + 31b (high: 4 mg kg^{-1} ; low: 0.4 mg kg^{-1}). Reproduced with the permission from ref. 166. Copyright 2018, Nature Publishing Group.

enhanced the cell penetration but also increased the intracellular activity of drugs (Fig. 11b).¹⁶³ Attributed to the pH-sensitive linker between anti-Her2 antibody and TCO-Dox, TCO-Dox was efficiently released at the tumor sites. Based on the bioorthogonal chemistry, TCO-Dox was specifically activated by 3,6-dimethyl-1,2,4,5-tetrazine (Me₂Tz) in tumor cells, thus ensuring the excellent anticancer effect and biocompatibility. In the future work, Me₂Tz can be endowed with a tumor-targeted function to develop a dual-targeting project, which may further enhance the therapeutic efficacy and reduce side effects.

It is well known that targeting approaches can efficiently concentrate prodrugs or drug conjugates at desired locations,^{164,165} however the following controlled drug release becomes a challenge. Wang *et al.* developed a concentration-sensitive system for prodrug activation based on the kinetics of the bioorthogonal reaction (Fig. 11c-I).¹⁶⁶ In detail, it is assumed that the concentration of prodrug in blood was low and did not cause toxicity (second-order rate constant = 0.25 M⁻¹ s⁻¹, calculated $t_{1/2}$ = 100 h). When the prodrugs were enriched at the target sites, the kinetics of click reactions rapidly triggered the drug release, thus enhancing the cytotoxicity of prodrug. In this system, tetrazine/cyclooctyne and cyclopentadienone/strained alkyne were selected as two bioorthogonal pairs for prodrug activation, DOX and CO were two drug models. Triphenylphosphonium (TPP) decoration was used to enrich drugs in mitochondria to decrease their first $t_{1/2}$. In tetrazine/cyclooctyne bioorthogonal system, drug release was triggered by a click, cyclization and release (CCR) sequential process. The IC₅₀ values of HeLa cells treated with TPP-decorated prodrugs were lower than that in non-TPP prodrug groups, indicating that enrichment of prodrugs in mitochondria promoted the DOX release. In cyclopentadienone/strained alkyne bioorthogonal system, a naphthalene group was introduced into the structure of cyclopentadienone to obtain a fluorescence imaging capability. Fluorescence imaging (Fig. 11c-II), tumor necrosis factor- α (TNF- α) and serum alanine aminotransferase (ALT) (Fig. 11c-III) analysis collectively indicated that TPP conjugation was able to enhance the local delivery of CO and provided a potent potential for hepatoprotection. Based on the acquired results, these two enrichment-triggered release (ETR) approaches may play their therapeutic functions for treatment of acute liver injury and malignant tumors.

Adverse drug reactions (ADRs) of anticancer drugs strictly restrict their maximum doses, resulting in tumor metastasis and cancer recurrence. Various strategies including nanomedicines and prodrug activation have been developed to avoid ADRs,^{167,168} but the effectiveness of these approaches is not satisfactory. Gao *et al.* designed an enzyme-instructed supramolecular self-assembly (EISA) based on Tz/TCO decaging reaction to realize selective activation of prodrugs in cancer cells (Fig. 12a).¹⁶⁹ Because enzyme activity was specific to tumor cells, EISA precisely recognized the target cells and triggered the formation of supramolecular self-assembly. Tz moieties were attached onto the EISA motif (NapK(Tz)YF, 33) to trigger the iEDDA-mediated decaging reaction of TCO-caged prodrugs (TCO-Dox) in cancer cells. Based on this EISA, abundant Tz

groups accumulated inside tumor cells and TCO-Dox prodrugs were efficiently activated, both of which cooperatively led to the death of cancer cells. In the presence of EISA, the EC₅₀ value of TCO-Dox against HeLa cells was significantly lower than free DOX, indicating the accumulation of EISA in HeLa cells was more effective than free DOX. Tumor growth was obviously inhibited in the 33 + TCO-Dox group (Fig. 12b), and the body weight of mice remained stable throughout the treatment (Fig. 12c), indicating the bioorthogonal system not only guaranteed efficient tumor growth inhibition but also reversed the ADRs of DOX. Hence, this EISA provides a new possibility for small molecular prodrug to effectively alleviate ADRs in cancer chemotherapy.

Recently, bioorthogonal decaging reactions have been developed to activate prodrugs,¹⁷⁰⁻¹⁷² but multifunctional bioorthogonal platforms were rarely reported for tumor theranostics. Wu *et al.* developed a bioorthogonal system on the basis of vinyl ether/Tz decaging reaction to simultaneously realize prodrug activation and fluorescence imaging (Fig. 13a).¹⁷³ This platform consisted of a Tz-linked NIR fluorophore (Tz-NR) and a vinyl ether-conjugated camptothecin (vinyl ether-masked CPT). Owing to the through-bond energy transfer (TBET), the NIR fluorescence of Tz-NR was temporarily quenched. Upon the occurrence of bioorthogonal decaging reaction between Tz and vinyl ether groups, CPT was released from vinyl ether-masked CPT and NIR fluorescence of Tz-NR was recovered. To improve the bioavailability of the two-component system, Tz-NR and prodrugs were encapsulated into PEG-conjugated phospholipid vesicles, forming liposomal trigger (LIP-NR-Tz) and liposomal prodrug (LIP-prodrug), respectively. LIP-NR-Tz + LIP-prodrug showed a high tumor accumulation and activated NIR fluorescence *via* the EPR effect and bioorthogonal reaction (Fig. 13b). In addition, bioorthogonal system showed a higher tumor suppression efficiency and undetectable organ damage, confirming this combined strategy safely and efficiently erased tumors (Fig. 13c). This bioorthogonal decaging reaction offers a new strategy for cancer diagnosis and treatment in living systems.

Targeted delivery of nanomedicines has been widely used in cancer theranostics,¹⁷⁴ but they always have low therapeutic efficacy due to their limited penetration. Therefore, there is a need to exploit new nanoplatfoms that can deliver nanomedicines deeply into tumors. Inspired by the fact that inflammatory immune cells can be recruited to support the tumor growth, Hyeon *et al.* designed a click reaction-assisted immune cell targeting (CRAIT) strategy to transport nanomedicines to the interior and avascular sites of tumors (Fig. 14a-I).¹⁷⁵ TCO moieties were conjugated onto CD11b antibodies (anti-CD11b-TCO) and tetrazines were conjugated onto DOX-loaded mesoporous silica nanoparticles (MSNs-Tz) to form bioorthogonal pairs. CD11b⁺ inflammatory cells served as the active transporter to transport the DOX-loaded nanoparticles to the avascular regions of tumors. CD11b⁺ cells were still observed in tumor vessels at 24 h post injection of MSNs-Tz and anti-CD11b-TCO, suggesting that CRAIT-based drug delivery was efficient even after bioorthogonal nanoparticles were cleared from blood

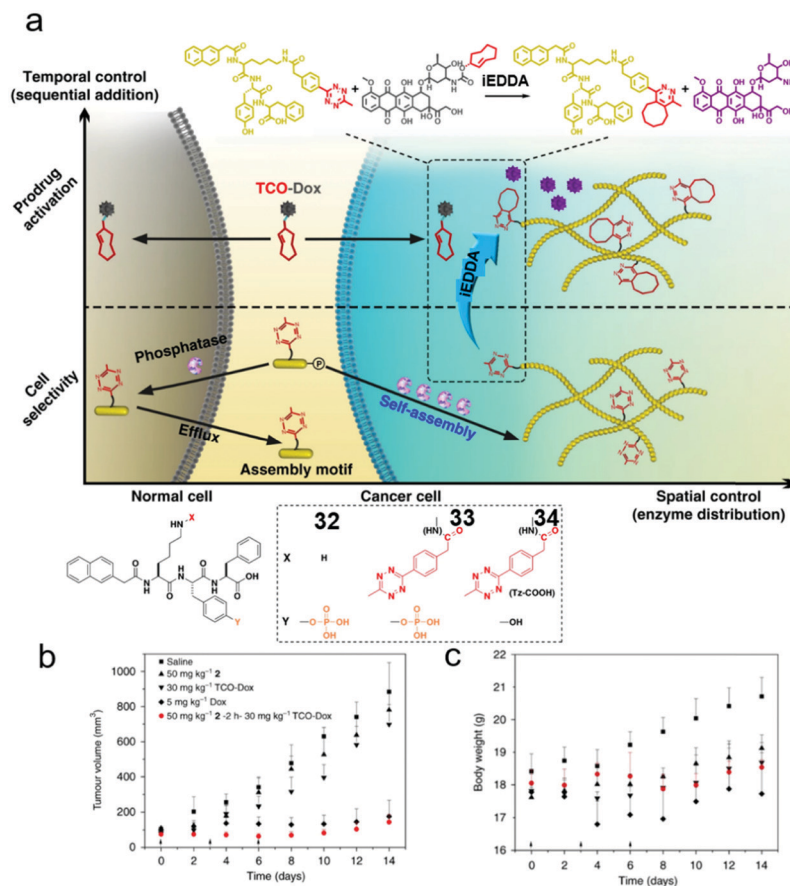


Fig. 12 Enzyme-catalyzed bioorthogonal strategy for tumor-specific prodrug activation. (a) Therapy mechanism of enzyme-catalyzed bioorthogonal strategy and structures of **32**, **33** and **34**. (b) Tumor growth curves of mice after different treatments. (c) The change of the body weight after different treatments. Reproduced with the permission from ref. 169. Copyright 2018, Nature Publishing Group.

(Fig. 14a-II). The therapeutic efficacy of CRAIT strategy on 4T1 tumor model was obviously higher than control groups (Fig. 14a-III), revealing that CRAIT strategy efficiently delivered therapeutic nanoparticles into tumors. CRAIT strategy also showed no notable toxicity to major organs, suggesting the minimized side effects of CRAIT strategy (Fig. 14a-IV). This CRAIT strategy can be developed to manipulate different nano-vehicles and cells for the treatment of life-threatening diseases without complex *ex vivo* manipulation of immune cells.

Multidrug resistance (MDR) is one main cause for the failure of cancer chemotherapy. Hence, how to increase the cellular drug concentration and prolong their retention time are crucial to overcome the MDR of cancer therapy.^{176,177} Bulte *et al.* designed a small molecule probe (Olsa-RVRR) which not only prolonged drug retention in tumors but also enhanced chemical exchange saturation transfer magnetic resonance imaging (CEST MRI) of tumors (Fig. 14b-I).¹⁷⁸ RVRR was conjugated onto anticancer drug Olsa to realize two functions: (1) enhancing the membrane penetration of Olsa-RVRR; (2) providing a substrate which is specific to furin. Upon entering into tumor cells overexpressing furin, Olsa-RVRR immediately took off the RVRR peptide and *tert*-butyl sulfydryl because of the catalysis of furin and GSH. Then, intermolecular click condensation between

cyano groups and 1,2-aminothiol groups occurred and produced Olsa nanoparticles (Olsa-NPs) in tumor cells, which not only prolonged drug retention but also enhanced CEST MRI signals (Fig. 14b-II). The OlsaCEST signals in HCT116 tumor were always higher than control groups, and the signals could still be observed even after 24 h (Fig. 14b-III), suggesting OlsaNPs were indeed formed in HCT116 tumors. In line with CEST MRI results, Olsa-RVRR showed a more effective tumor inhibition on both LoVo and HCT116 tumor models (Fig. 14b-IV), suggesting the tumor accumulation of OlsaNPs and their long retention time contributed to the high anticancer effect. This furin-targeted and MRI-guided platform has great potential for multi-directionally monitoring the drug accumulation, tumor aggressiveness and therapeutic response.

Because of the different sensitivity of cells to chemotherapeutics in solid tumor, tumor heterogeneity is still a major challenge in chemotherapy. Cancer stem-like cells (CSCs) are considered as the primary cause for intratumor heterogeneity, and also the chief offender of progression, recurrence and metastasis of malignancies. Mo *et al.* developed a cell differentiation-regulated nanomedicine (ATRA/CPT-NPs), in which all-*trans* retinoic acid (ATRA) and camptothecin (CPT) acted as differentiation-inducing agent and cytotoxic drug respectively,

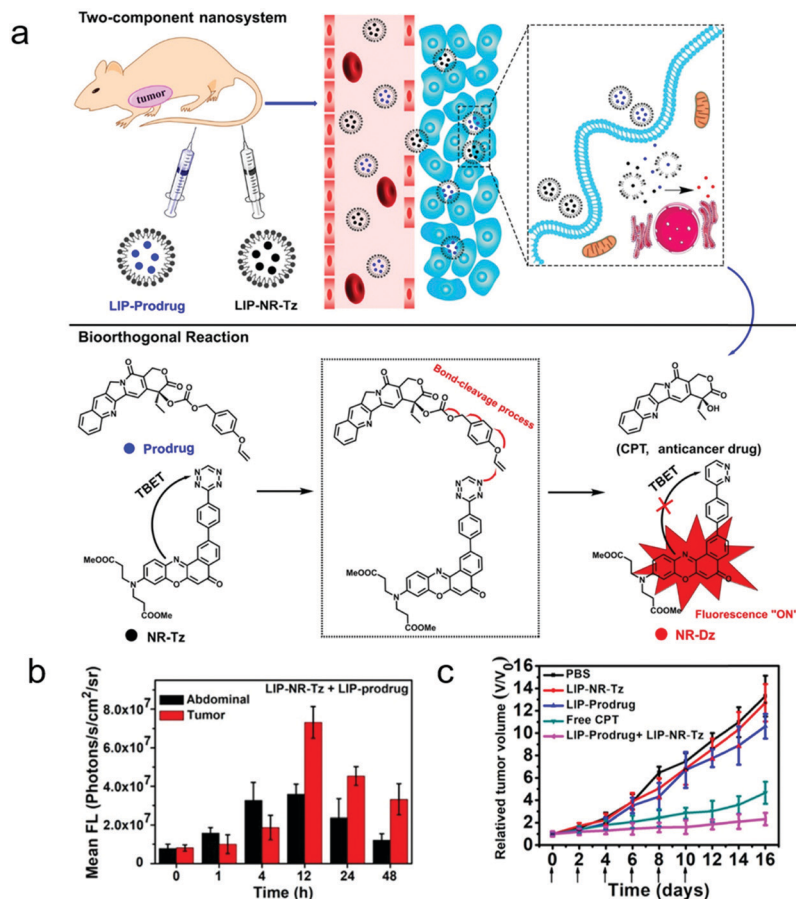


Fig. 13 Bioorthogonal nanoplatform for NIR imaging and selective prodrug activation. (a) Therapy mechanism of bioorthogonal nanoplatform. (b) The mean fluorescence intensities of abdomen and tumor at different time points after administration of LIP-NR-Tz + LIP-prodrug. (c) The change of body weight after different treatments. Reproduced with the permission from ref. 173. Copyright 2019, American Chemical Society.

to overcome the therapeutic barrier imposed by the CSCs-rooted heterogeneity (Fig. 15a-I).¹⁷⁹ After endocytosis by CSCs, ATRA/CPT-NPs rapidly released ATRA owing to the hypoxia-induced structure transition to initiate the differentiation of CSCs. Then the elevated ROS level from the differentiation of CSCs led to the release of CPT *via* the cleavage of oxalate linkers, thus enhancing the cytotoxicity to the differentiated cells (Fig. 15a-II). The released CPT also relieved tumor hypoxia condition by suppressing the expression of hypoxia-inducible factor-1 α (HIF-1 α) to keep the high chemotherapeutic efficacy. Compared with control groups, ATRA/CPT-NPs showed the strongest therapeutic benefits (Fig. 15a-III and -IV), suggesting the sequential ATRA and CPT release was necessary to improve the antitumor efficacy. As expected, ATRA/CPT-NPs not only inhibited the tumor growth (Fig. 15a-V), but also efficiently prevented tumor recurrence and metastasis, suggesting the outstanding anticancer promotion ability of this cell differentiation-regulated nanomedicine. The obtained results provide a perspective prospect for synergistic nanotherapeutic strategy in overcoming CSCs-related chemotherapeutic resistance.

Mitochondrial dysfunction has a close relationship with a variety of diseases, such as obesity, neurodegenerative diseases, diabetes and malignancy. It is urgently desired to develop novel

theranostic approaches to fight against mitochondriopathies. Vrabel *et al.* designed a series of 1,2,4,5-tetrazines (35a–35i) which selectively accumulated in the mitochondria of living cells and underwent bioorthogonal reactions with TCO-caged molecules to release fluorescent molecules or active drugs (Fig. 15b-I).¹⁸⁰ 35b, 35e and 35i exhibited rapid release of fluorescent dyes in cells and one-cell mouse embryos within 2 h (Fig. 15b-II), suggesting this bioorthogonal strategy could realize a fast and accurate fluorescence imaging. In addition to bioimaging, this strategy was also applied in prodrug activation. TPP and TCO groups were attached onto the hydroxyl group of niclosamide *via* a self-immolative linker to obtain TCO-TPP-niclosamide. The protonophoric activity of niclosamide was recovered in the presence of 35i, indicating prodrug activation was realized in cells (Fig. 15b-III). Based on these encouraging results, it is believed that more biological processes will be regulated by the bioorthogonal reaction in a more precise manner in the near future.

3.2 Metal-free bioorthogonal click chemistry for photodynamic therapy (PDT) and photothermal therapy (PTT)

Prodrug activation triggered by bioorthogonal chemistry has a potential to overcome the tumor heterogeneity, but the majority

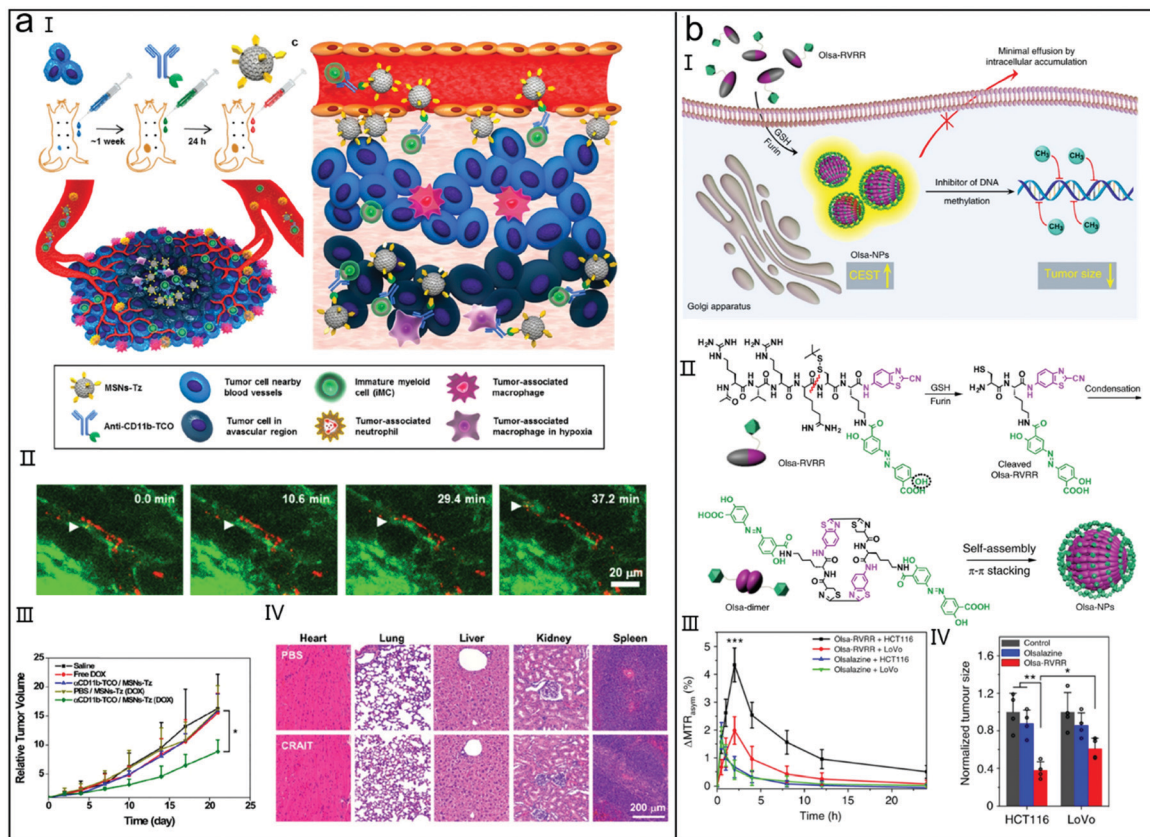


Fig. 14 (a) CRAIT strategy to realize deep tumor penetration. (I) Illustration of CRAIT strategy. (II) Images of tumor blood vessels in mice at 24 h after treatment with anti-CD11b-TCO + MSNs-Tz (green: anti-CD11b-TCO; red: MSNs-Tz). (III) Tumor growth curves after different treatments. (IV) Haematoxylin and eosin (H&E)-staining of main organs after different treatments. Reproduced with the permission from ref. 175. Copyright 2019, American Chemical Society. (b) Furin-triggered nanodrugs to enhance MRI and tumor therapy. (I) Therapy mechanism of Olsa-RVRR in cells overexpressing furin. (II) Self-assembly of Olsa-RVRR. (III) Time course of standardized OlsaCEST signal in tumors after different treatments (subtraction of the MTR_{asym} value at 0 h to acquire standardized OlsaCEST signal). (IV) Normalized tumor size in different groups at day 33 (normalized to PBS group). Reproduced with the permission from ref. 178. Copyright 2019, Nature Publishing Group.

of current activation strategies rely on endogenous enzymes or receptors which are expressed differently in different tumors.^{181,182} As acidosis is regarded as a typical characteristic of tumor, the acidic microenvironment is always used as a tumor-specific stimulus to trigger bioorthogonal reactions in tumors. Wang *et al.* designed a pH-responsive polymer containing tertiary amine and tetrazine groups (PEG-P(AEMA-*r*-Tz)) (Fig. 16a).¹⁸³ Under neutral conditions, polymers self-assembled into micelles (ASTNs) to enclose the tetrazine groups and shield their activity. However, micelles rapidly collapsed and tetrazine groups were activated in the acidic tumor microenvironment, thus initiating bioorthogonal reactions in tumors. To realize imaging-guided cancer treatment, a macrotheranostic prodrug CyPVE composed of a PEG hydrophilic chain and a vinyl ether-caged hemicyanine dye (CyPOH) was constructed. Under the acidic microenvironment, the vinyl ether groups of CyPVE were cleaved by ligation-elimination bioorthogonal reactions, thus the phototoxicity and NIR fluorescence of CyPOH was activated. The red fluorescence signal was only lit up around the periphery of the multicellular spheroids (MCSs) derived from 4T1 cells at pH 7.4, but could reach a 100 μm depth at pH 6.5 (Fig. 16b),

demonstrating CyPVE was activated by ASTNs in the acidic environment. The theranostic performances of the ASTNs/CyPVE group surpassed the control groups, including *in vivo* fluorescence imaging, tumor inhibition and safety, collectively demonstrating this new prodrug activation strategy had a great potential in promoting the development of smart cancer theranostics.

It is well known that targeted drug delivery can increase the accuracy of cancer treatment. Nevertheless, this active targeting strategy always has limited tumor penetration, thus the outcomes of cancer therapy are unsatisfactory.^{184,185} Wang *et al.* developed an extracellular vesicles (EVs)-mediated metabolic tumor labelling strategy to enhance the tumor penetration ability of drug delivery systems (Fig. 17a-1).¹⁸⁶ Attributed to the EPR effect and metabolic glycoengineering, nanoscale azide precursors (Az-NPs) could label perivascular tumor cells with abundant azide groups. Through the delivery by EVs, the azide-containing ligands diffused all over the tumor tissues and the whole tumor region was well labelled. Meanwhile, the post-injected DBCO-Ce6 prodrug easily penetrated into tumor tissues to kill cancer cells *via* PDT. Almost all the 4T1 cells died after the

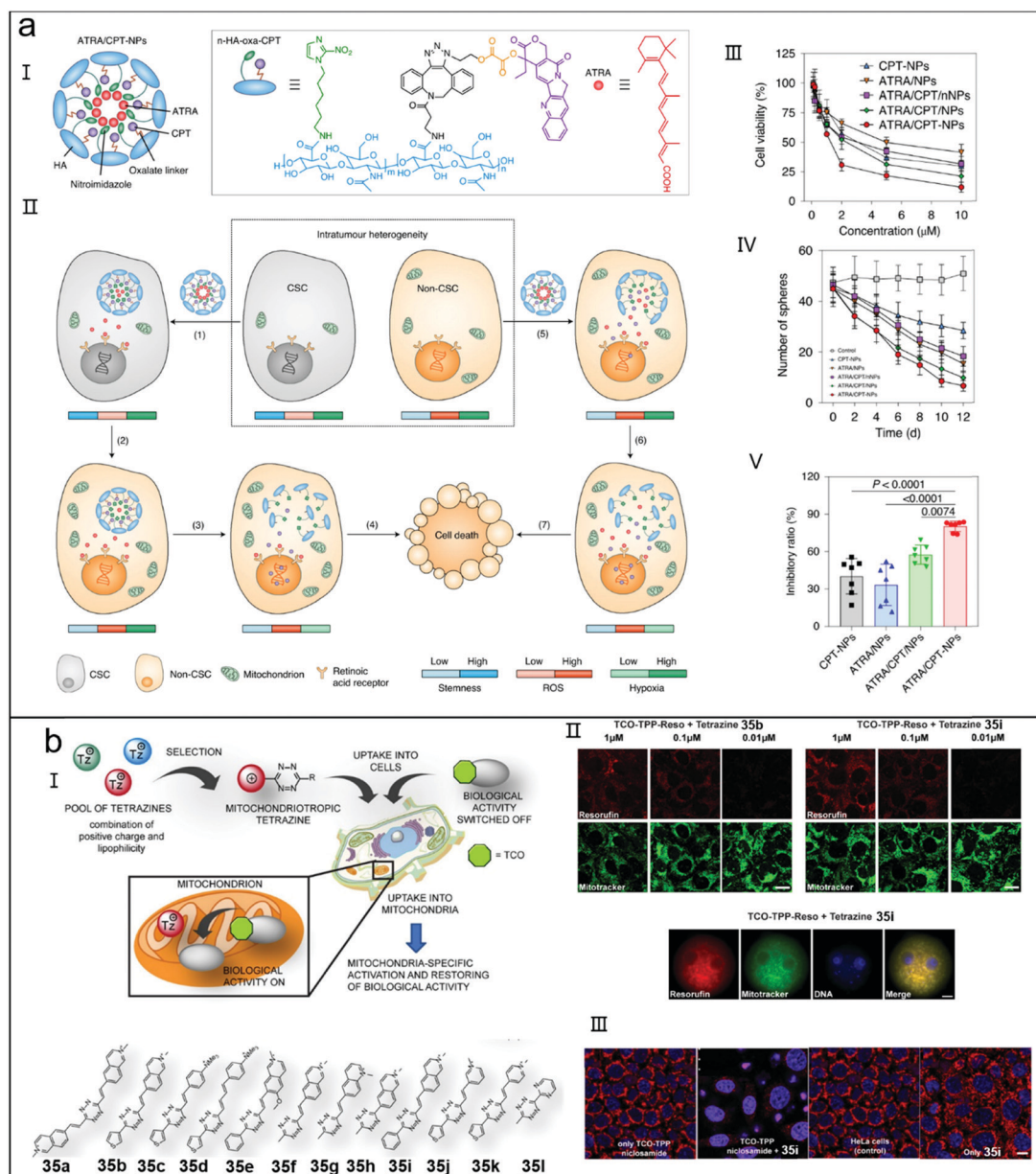


Fig. 15 (a) Cell differentiation-regulated therapeutic strategy to overcome the heterogeneity of CSC. (I) Chemical structures of the components of ATRA/CPT-NPs. (II) Mechanism of cell differentiation-regulated therapeutic strategy. (III) Cell viability of MCF-7 SP cells after different treatments. (IV) The number of tumour spheres after different treatments within 12 days (diameter > 50 μm). (V) Inhibitory ratios of tumors after different treatments. Reproduced with the permission from ref. 179. Copyright 2021, Springer Nature Limited. (b) Mitochondria-targeted bioorthogonal strategy for prodrug activation. (I) Mechanism of mitochondria-targeted bioorthogonal strategy and chemical structures of 1,2,4,5-tetrazines derivatives. (II) CLSM images of cells (above) and one-cell mouse embryos (below) after treatment with TCO-TPP-Reso + Tetrazine 35b or TCO-TPP-Reso + Tetrazine 35i. (III) CLSM images of cells after treatment with 35i, TCO-TPP niclosamide or TCO-TPP niclosamide + 35i. Scale bar: 10 μm . Reproduced with the permission from ref. 180. Copyright 2020, American Chemical Society.

treatment with Az-NP/DBCO-Ce6, suggesting Ce6 was firmly anchored on the cell membrane and generated abundant ROS to kill tumor cells (Fig. 17a-II). The red fluorescence of Ce6 in the Az-NPs/DBCO-Ce6 group appeared both in the margin and interior of avascular regions, but the red fluorescence of control groups only appeared at the periphery, indicating EVs played a key role in transporting azide ligands into tumor. This artificial EVs-mediated targeting strategy offers a novel alternative strategy for

current drug delivery systems to enhance their tumor targeting ability and penetration.

A theranostic nanoplatform that combines fluorescence imaging with PTT can ensure precise diagnosis and efficient treatment of deep-seated tumors. Nevertheless, a light activatable nanosystem with both bright fluorescence signal and high PTT efficiency is difficult to obtain, because fluorescence emission always competes with photothermal efficiency.^{187,188}

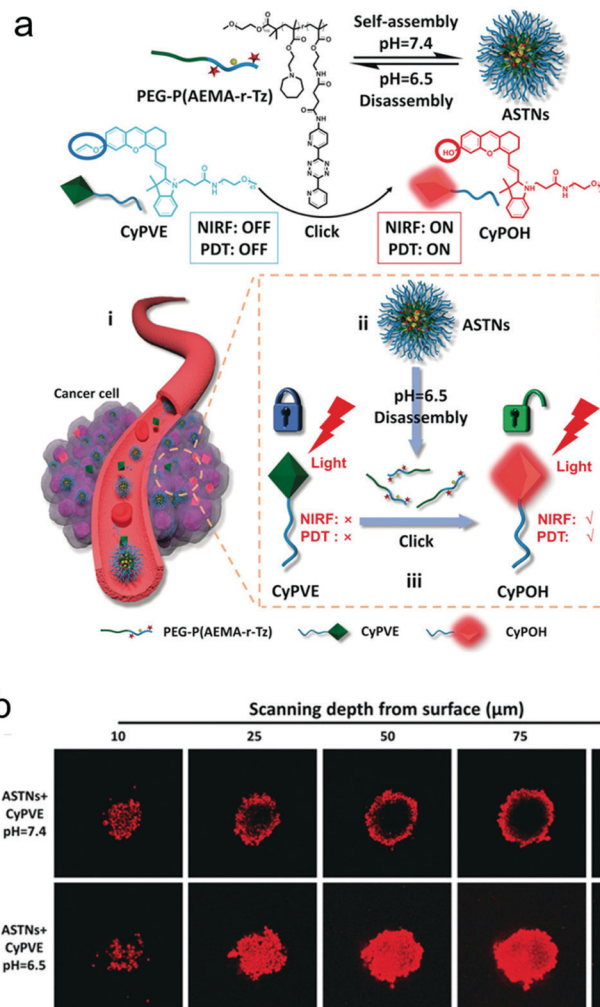


Fig. 16 Low pH-triggered prodrug activation strategy to enhance the tumor penetrability of nanomedicine. (a) Mechanism of low pH-triggered prodrug activation strategy. (b) CLSM images of 4T1 MCSs after treatment with ASTNs + CyPVE for 4 h at pH = 6.5 or pH = 7.4. Scale bar: 100 μm. Reproduced with the permission from ref. 183. Copyright 2020 Wiley-VCH Verlag GmbH & Co. KGaA, Weinheim.

Fan *et al.* developed a squaraine-based semiconducting polymer, which was decorated with DBCO groups (PSQPNs-DBCO) to realize accurate fluorescence imaging and high-efficient PTT treatment (Fig. 17b-I).¹⁸⁹ PSQPNs-DBCO emitted an NIR-II fluorescence at 1290 nm and had a high S/N ratio in living system. Attributing to the azide/DBCO bioorthogonal click reactions, PSQPNs-DBCO selectively accumulated in the tumor tissues, thus significantly improving the efficiency of cancer theranostics. The major blood vessels of brain, abdomen and hind limb of mice were easily distinguished from the background in PSQPNs-DBCO + Ac₄ManNAz group, revealing that PSQPNs-DBCO was an optimal nanoprobe to image vascular systems (Fig. 17b-II). PSQPNs-DBCO + Ac₄ManNAz also induced the strongest tumor fluorescence and highest tumor inhibition, firmly confirming bioorthogonal chemistry-guided PSQPNs-DBCO enhanced the tumor targeting ability of the theranostic agents. Based on these outstanding *in vivo* performances, this NIR II theranostic system has a great potential to realize its clinical transformation.

Light-gated ion channels can spatiotemporally regulate cellular activities by optically controlling the transport of ions across the cell membrane. However, most of the current strategies are dependent on UV or visible light, thus greatly limiting their applications in living systems.^{190,191} Xing *et al.* reported an NIR light-initiated strategy, in which neodymium (Nd³⁺) doped upconversion nanocrystals (UCNs) were site-specifically attached on the cell membrane *via* N₃/DBCO bioorthogonal click reaction to spatiotemporally regulate Ca²⁺ ion-channel activity (Fig. 18a-I).¹⁹² DBCO group was conjugated onto UCNs, affording DBCO-UCNs which converted 808 nm NIR light into 480 nm light. Channelrhodopsins-2 (ChR2) protein could be activated by 480 nm light and realized remote control of Ca²⁺ influx. Irradiation with 808 nm light resulted in a great increase of intracellular Ca²⁺ in a light dose-dependent manner in ChR2 + Ac₄ManNAz + DBCO-UCNs group (Fig. 18a-II), indicating the Ca²⁺ level inside cells was precisely regulated by NIR light. In zebrafish model, ChR2 + Ac₄ManNAz + DBCO-UCNs group also efficiently regulated Ca²⁺ ion-channel activity

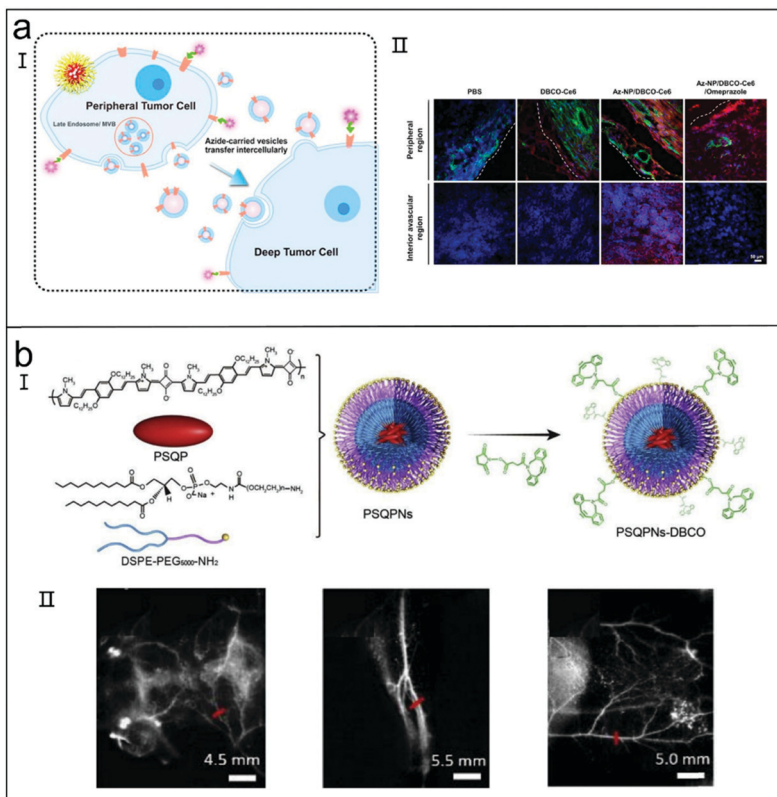


Fig. 17 (a) EVs-mediated bioorthogonal strategy to enhance the tumor penetrability of nanomedicine. (I) Illustration of EVs-mediated bioorthogonal strategy. (II) CLSM images of freezing microtome section of tumors in different groups (green: Alexa Fluor[®] 488-tagged CD31 antibody; red: Ce6). Scale bar: 50 μ m. Reproduced with the permission from ref. 186. Copyright 2020, Elsevier Ltd. (b) 1064 nm-excitable theranostic nanoplatform for NIR-II FI and PTT. (I) Preparation process of PSQPNs-DBCO. (II) NIR-II fluorescence images of the brain, leg and abdomen of mice in the PSQPNs-DBCO group. Reproduced with the permission from ref. 189. Copyright 2020, Elsevier Ltd.

(Fig. 18a-III) and increased the expression of caspase-3, suggesting this strategy conveniently manipulated the activation of ion channels and apoptosis *in vivo*. Hence, this light-gated ion strategy has great potentials to specifically regulate membrane-associated physiological processes in living systems.

Although various strategies have been developed to treat cancer, the evaluation of therapeutic outcomes is always delayed and invasive.^{193,194} Liang *et al.* designed a small molecular NIR probe Cys(StBu)-Asp-Glu-Val-Asp-Lys(Cypate)-CBT (Cy-CBT) to evaluate tumor therapeutic effect in real-time (Fig. 18b-I).¹⁹⁵ Cy-CBT underwent CBT-Cys condensation and self-assembled into nanoparticles (CyCBT-NP) in the presence of GSH. Because of the inter- and intra-molecular quenching effect, the fluorescence of Cy-CBT-NP was temporarily quenched, but the photo-thermal effect of the probe was activated. The caspase 3-induced cleavage of Asp-Glu-Val-Asp (DEVD) moiety from CyCBT-NP resulted in the collapse of Cy-CBT-NP and recovery of NIR fluorescence, which could be used to evaluate the PTT effect of Cy-CBT-NP. The fluorescence of tumor in Cy-CBT-NP group gradually increased and the fluorescence intensity had a proportional relationship with irradiation time, demonstrating Cy-CBT-NP self-evaluated their PTT efficiency *via* apoptosis-dependent fluorescence imaging. Compared with control groups, Cy-CBT-NP + laser was able to induce severe apoptosis of tumors (Fig. 18b-II),

and its anticancer effect was the most prominent (Fig. 18b-III). Based on the excellent performances of Cy-CBT-NP, it can realize simultaneously PTT and real-time self-evaluation of therapeutic results in clinic.

Superparamagnetic iron oxide nanoparticles (SPIO NPs) have been used to enhance T_2 -weighted imaging and improve the PTT effect *via* assembly/aggregation for cancer theranostics.^{196,197} However, SPIO NPs tend to form clusters under physiological conditions, followed by the rapid clearance by the mononuclear phagocyte system. Yu *et al.* designed an Ac-Arg-Val-Arg-Arg-Cys(StBu)-Lys-CBT probe (36) and then conjugated it onto SPIO NPs to generate Ac-Arg-Val-Arg-Arg-Cys (StBu)-Lys(SPIO)-CBT (SPIO@1NPs) which could realize tumor-specific accumulation (Fig. 19a).¹⁹⁸ After endocytosis by furin-overexpressing tumor cells, the disulfide bond of SPIO@1NPs was reduced by GSH and the RVR substrate was cleaved by furin, both of which initiated CBT-Cys condensation and triggered the formation of SPIO aggregates. MRI T_2 contrast of MDA-MB-468 tumor was greatly improved after injection of SPIO@1NPs, indicating T_2 -weighted imaging of tumors was enhanced by this furin-triggered aggregation (Fig. 19b). The therapeutic effect of PTT in SPIO@1NPs group was the highest while its systemic toxicity was low (Fig. 19c), suggesting tumor-specific accumulation of SPIO aggregates guaranteed the safety of this therapeutic

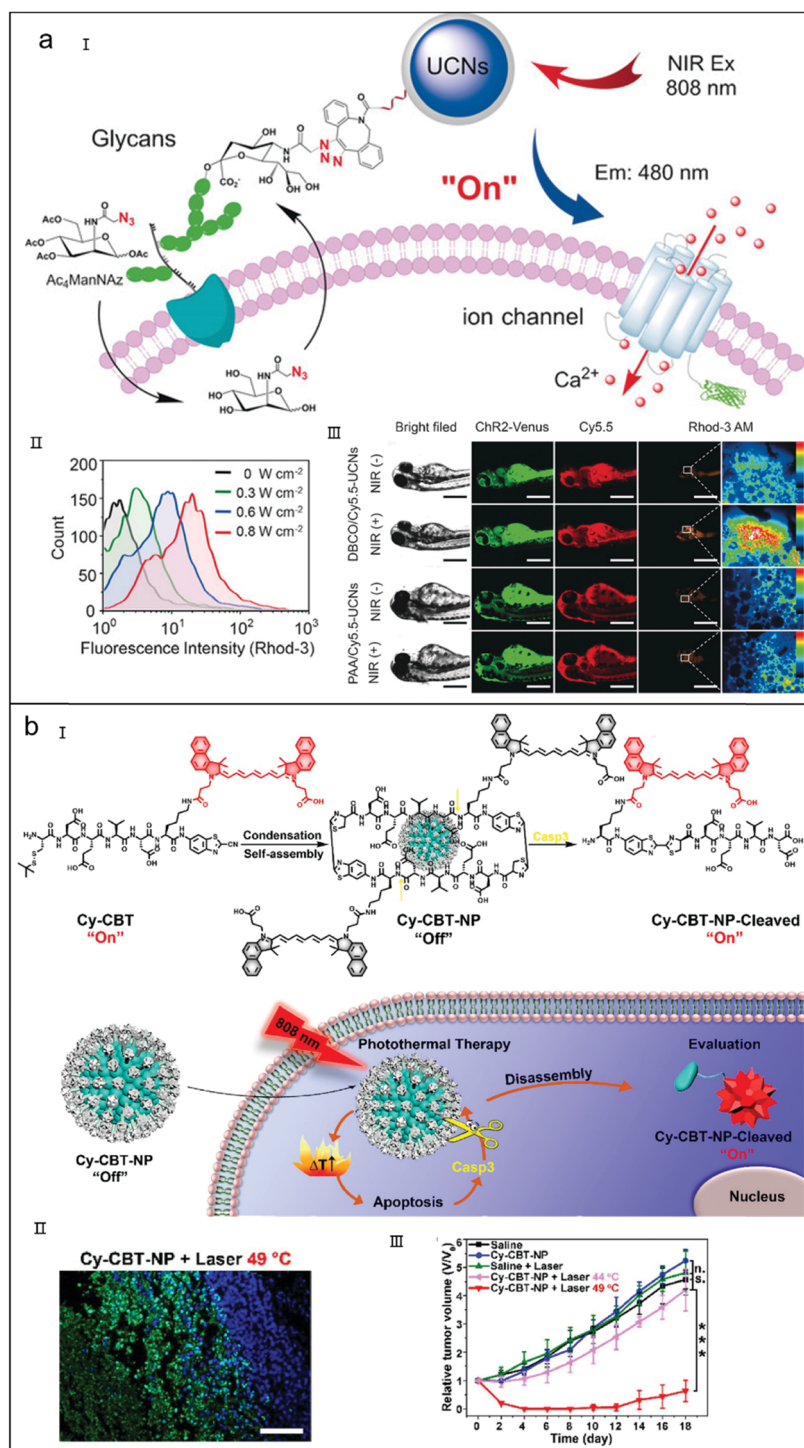


Fig. 18 (a) UCNs-based bioorthogonal strategy to remote control of cation influx. (II) Mechanism of remote control of cation influx. (III) Flow cytometry (FCM) analysis of intracellular Ca^{2+} concentration with different light power. (III) Fluorescence imaging of zebrafish after treatment with DBCO/Cy5.5-UCNs or PAA/Cy5.5-UCNs with or without NIR light. Scale bar: 400 μm . Reproduced with the permission from ref. 192. Copyright 2017, Wiley-VCH Verlag GmbH & Co. KGaA, Weinheim. (b) Reduction-triggered bioorthogonal strategy to self-evaluate anticancer effect. (II) Mechanism of reduction-triggered bioorthogonal strategy. (II) TUNEL staining of tumor from mice sacrificed at 24 h after treatment with Cy-CBT-NP + laser. (III) Tumor volume curves of mice bearing HeLa tumor in different groups. Scale bar: 50 μm . Reproduced with the permission from ref. 195. Copyright 2020, Wiley-VCH Verlag GmbH & Co. KGaA, Weinheim.

strategy. Based on this furin-triggered intracellular self-aggregation strategy, exogenous SPIO NPs could selectively accumulate in tumor and realize MRI-guided PTT for cancer.

Nanovehicles that can undergo size deformation in the abnormal tumor microenvironment (TME) can pass through the stroma-dominant penetration barrier and improve the

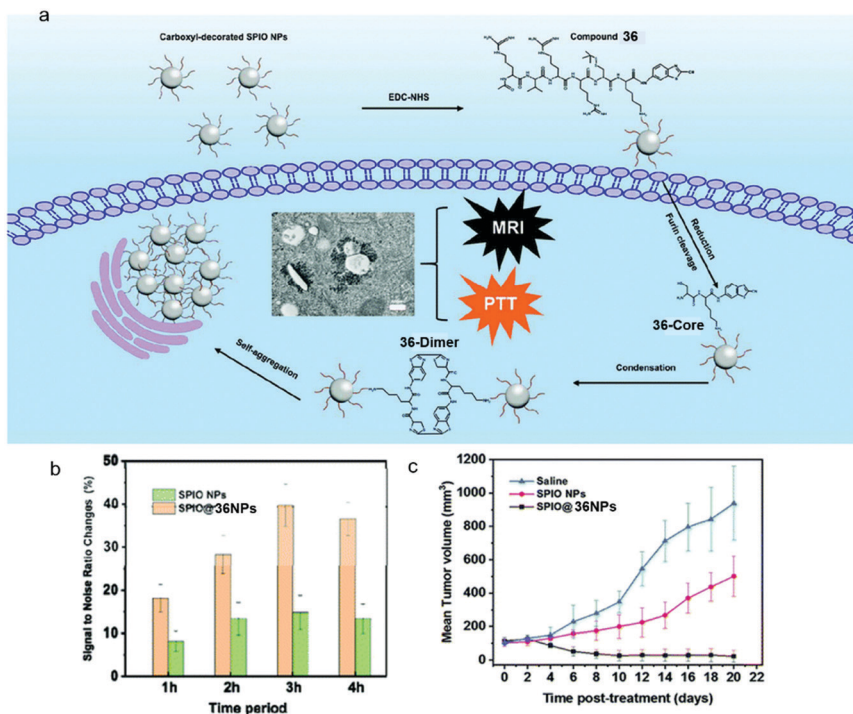


Fig. 19 Furin-triggered Fe_3O_4 nanoplatform to enhance T_2 -weighted MRI and PTT *in vivo*. (a) Mechanism of MRI and PTT of furin-triggered Fe_3O_4 nanoplatform. (b) Time course S/N ratio change of tumors from mice treated with SPIO@36NPs or SPIO NPs in different groups. (c) Tumor volume curves of mice in different groups. Reproduced with the permission from ref. 198. Copyright 2020, The Royal Society of Chemistry.

effective concentration of therapeutic agents in deep tumor tissue. Nevertheless, merely circumventing TME barriers in the process of drug delivery is inadequate, because TME can nourish residual tumor cells to promote their metastasis, thus leading to the failure of cancer therapies. Min *et al.* developed a nanoframework (T-PFRT) composed of a therapeutic module and a TME-normalizing module to remodel TME.¹⁹⁹ Zinc phthalocyanine photosensitizer was encapsulated in the ferritin nanocage (PFRT) to construct the therapeutic module, and stroma-remolding inducer (iTGF β) and oxygen supplier hemoglobin (Hb) were encapsulated in the cavity of lipid-covered dendritic mesoporous silica nanoparticles (DMSN-L) to establish the TME-normalizing modules. A peptide linker sensitive to matrix metalloproteinase 2 (MMP2) was utilized to conjugate DMSN-L (~ 100 nm) with PFRT (~ 12 nm), forming a “core-satellite” structure (Fig. 20a-I). In the TME where MMP2 over-expressed, T-PFRT liberated small PFRT for PDT. Meanwhile, the synergistic effect of Hb-enhanced oxygen supply and iTGF β -induced excessive extracellular matrix (ECM) depletion remodeled TME, overcoming the obstacles of hypoxia and stroma. The TME normalization further facilitated deep penetration of small PFRT, thereby improving the performance of PDT in deep tumor tissues. Compared with control groups, DMSN-PFRT showed deeper penetration, indicating the introduction of stroma remodeling agents eliminated the ECM obstacles in the process of drug delivery (Fig. 20a-II). DMSN-PFRT also showed higher oxygen delivering capacity under hypoxic conditions, suggesting the anoxic condition of tumor could be improved. T-PFRT could significantly inhibit the

growth and metastasis of tumor cells (Fig. 20a-III-VI) *in vitro* and *in vivo*. Through delicate design, this core-satellite nanoframework can be developed into other therapeutic systems to realize TME remodeling-facilitated disease treatment.

Radiodynamic therapy (RDT) with the ability to transform X-rays to UV-visible light for PDT is an emerging therapeutic method to overcome the defects of the traditional radiotherapy (RT) and PDT, such as the unfocused energy of RT and the restricted penetration depth of PDT. Nanoscale metal organic frameworks (NMOFs) established from high-Z ions and photosensitizers (PSS) can conduct the energy of X-rays to PSS to realize RDT. However, the reported NMOFs have some ineluctable drawbacks such as ACQ effect, low singlet oxygen production and no fluorescent tracking. Liu *et al.* used an AIE PS and hafnium ions (Hf^{4+}) to construct a NMOF (Hf-AIE) to realize synergistic RDT and RT.²⁰⁰ To increase the biocompatibility, Hf-AIE core was decorated with lipid to form Hf-AIE-PEG (Fig. 20b-I). DBCO/ N_3 bioorthogonal reaction and metabolic glycoengineering promoted the tumor accumulation of nanomedicine. The fluorescence of cells in Hf-AIE-PEG-DBCO + Ac_4ManNAz group was distinct and overlapped well with the cell membrane (Fig. 20b-II), suggesting Hf-AIE-PEG-DBCO nanoparticles were successfully anchored on the surface of N_3 -labelled tumor cells through bioorthogonal reaction. The accumulation of Hf-AIE-PEG-DBCO in tumors pretreated with Ac_4ManNAz was higher than control groups (Fig. 20b-III), revealing that click chemistry enhanced tumor accumulation of Hf-AIE-PEG-DBCO. Attributing to the deep tissue penetration of X-ray, the anticancer efficacy of Hf-AIE-PEG-DBCO + Ac_4ManNAz + X-ray group was also satisfactory even

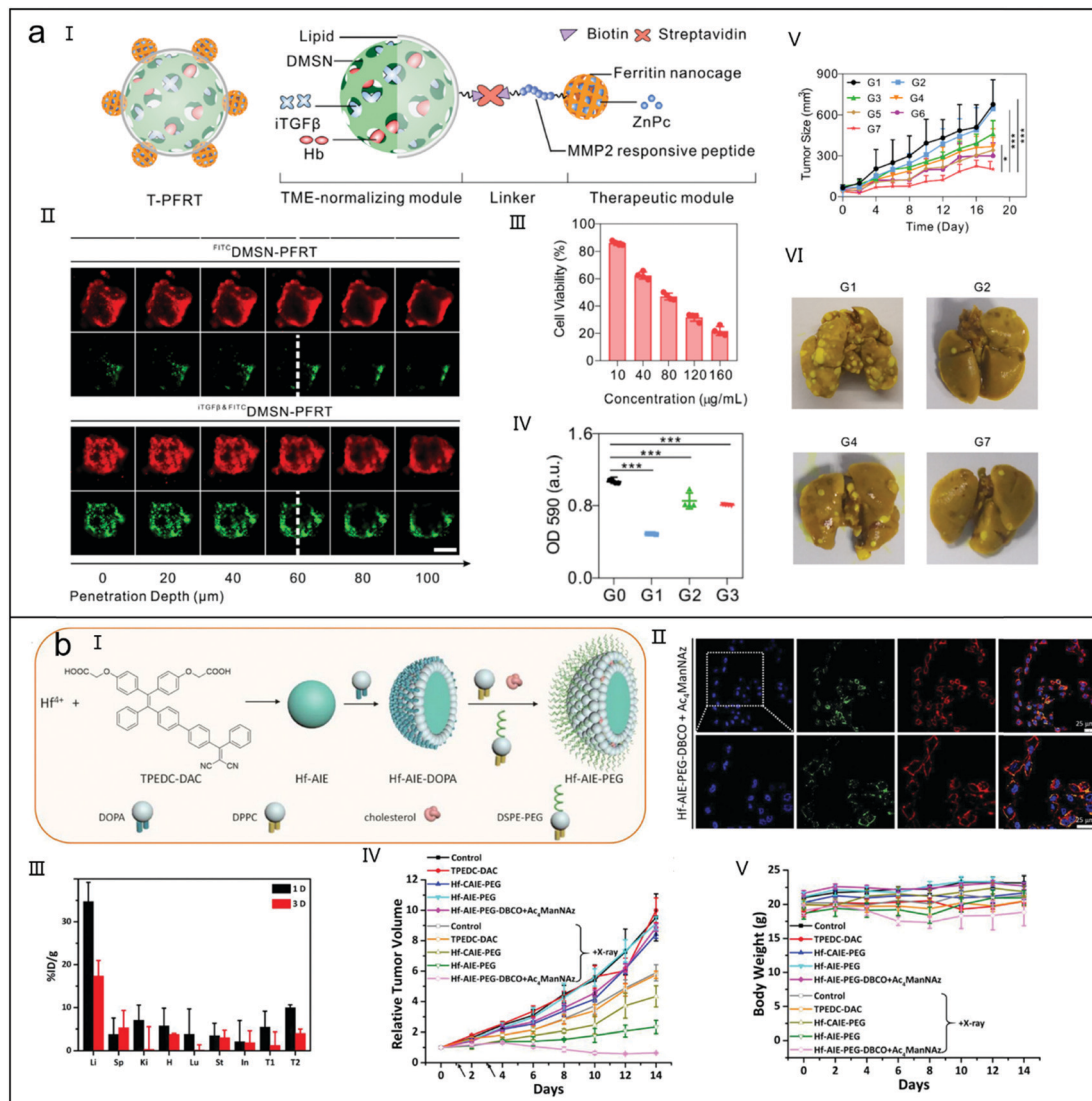


Fig. 20 (a) Size transformable nanoframeworks to enhance PDT. (I) The composition of nanoframework T-PFRT. (II) Penetrability analysis of DMSN-PFRT with or without MMP2-cleavable peptide linkage in 3D tumor spheroid model. (III) Cell viability of 4T1 cells treated with different concentrations of T-PFRT. (IV) Migration of 4T1 cells after different treatments (G0: control group, G1: iTGF β , G2: iTGF β DMSN-L, G3: iTGF β DMSN-PFRT). (V) Tumor growth curves of mice after different treatments (G1: PBS; G2: T-PFRT without laser irradiation; G3: DMSN-PFRT (w/o pep) with laser irradiation; G4: DMSN-PFRT with laser irradiation; G5: iTGF β DMSN-PFRT with laser irradiation; G6: ^{oxy}Hb DMSN-PFRT with laser irradiation; G7: T-PFRT with laser irradiation). (VI) Images of lung nodule metastases of mice in different groups. Scale bar: 200 μ m. Reproduced with the permission from ref. 199. Copyright 2021, Wiley-VCH Verlag GmbH & Co. KGaA. (b) Bioorthogonal AIE nanomedicine to realize RT and RDT. (I) Preparation route of Hf-AIE-PEG. (II) CLSM images of 4T1 cells pretreated with Ac $_4$ ManNAz followed by Hf-AIE-PEG-DBCO. (III) Biodistribution of Hf-AIE-PEG-DBCO in mice at 1 day or 3 day post-injection (T1 and T2 are tumors without and with Ac $_4$ ManNAz pretreatment. Li: liver, Sp: spleen, Ki: kidney, H: heart, Lu: lung, St: stomach, In: intestine). (IV) Tumor growth curves of mice in different groups. (V) Body weight change of mice in different groups. Scale bar: 25 μ m. Reproduced with the permission from ref. 200. Copyright 2021, Wiley-VCH Verlag GmbH & Co. KGaA.

a 3 mm lean pork covered on the tumor (Fig. 20b-IV). Notably, there was no obvious organ damage and detectable body weight change (Fig. 20b-V), indicating the excellent biosafety of Hf-AIE-PEG-DBCO. Based on these results, this bioorthogonal AIE NMOF has great potentials in treating deep tumor through the synergistic RDT and RT.

3.3 Metal-free click chemistry for cancer immunotherapy

The pretargeted radioimmunotherapy (PRIT) is a multistep strategy which delivers high dose of radioactive therapeutics

to tumors but low dose to normal tissues.^{201,202} Quinn *et al.* designed two kinds of tetrazine-based chelators (DOTA-PEG $_{10}$ -tetrazine and TCMC-Bn-SCN-PEG $_{10}$ -tetrazine) and investigated their radiolabelling efficiency in ^{212}Pb α -particle involved PRIT (Fig. 21a-I).²⁰³ A mouse monoclonal antibody (mAb), CC49, was conjugated with TCO groups to give rise to a pretargeting molecule (CC49-TCO). PRIT strategy consisted of three steps: (1) pretargeting CC49-TCO; (2) injecting clearing agent; (3) injecting ^{212}Pb -DOTA-Tz (Fig. 21a-II). As expected, ^{212}Pb -DOTA-Tz efficiently suppressed the tumor growth in a

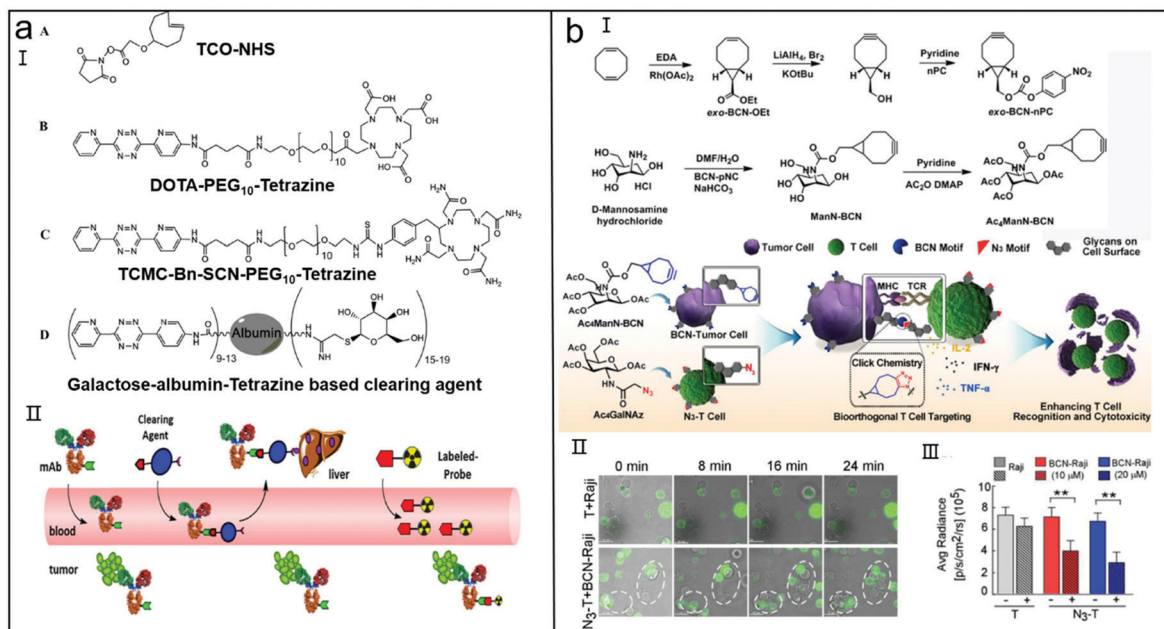


Fig. 21 (a) Pretargeted radioimmunotherapy mediated by bioorthogonal cycloaddition chemistry. (I) Structures of bioorthogonal reagents. (II) Mechanism of pretargeted radioimmunotherapy. Reproduced with the permission from ref. 203. Copyright 2017, American Chemical Society. (b) Bioorthogonal T cell-targeted strategy to enhance anticancer effect. (I) Synthetic route of $Ac_4ManN-BCN$ and the mechanism of T cell-targeted strategy. (II) Time-lapse CLSM images of cocultured Raji cells and T cells treated with or without $Ac_4GalNAz$ ($Ac_4ManN-BCN$) (T cell with green fluorescence stained by anti-CD3; Raji cells with no fluorescence). (III) Cytotoxicity of N_3-T cells against $BCN-Luci-Raji$ cells (fluorescence intensity of luciferase is proportional to the survival rate of Raji cells; the concentration of $Ac_4ManNBCN$: 10 or 20 μM). Scale bar: 15 μm . Reproduced with the permission from ref. 206. Copyright 2018, Wiley-VCH Verlag GmbH & Co. KGaA, Weinheim.

dose-dependent manner and greatly improved the survival rate. Although high dose of $^{212}Pb-DOTA-Tz$ (such as 7.40 MBq) caused acute radiation toxicity, it was safe at low dose. This ^{212}Pb α -particle-involved PRIT strategy is a good example to promote the development of PRIT.

It is well known that tumor cells can be killed by T cells *via* cell surface recognition.^{204,205} However, the heterogeneity of receptors on the surface of tumors and the low affinity between T cells and tumor cells always result in the low therapeutic efficacy and severe off-target effect. Cai *et al.* reported a targeting strategy to enhance the recognition between T cells and tumor cells (Fig. 21b-I).²⁰⁶ In this targeting strategy, complementary bioorthogonal moieties (azide group and BCN group) were separately anchored on the surface of T cells and tumor cells *via* glycolytic process. Attributing to the bioorthogonal click reactions, BCN-tumor cells firmly connected with the N_3-T cells, promoting the recognition ability of T cells toward tumor cells and activating T cells. When N_3-T cells and BCN-Raji cells moved closely, they immediately bound together and called up more cells to form a big cell cluster, indicating that fast bioorthogonal reactions on cell surface promoted the migration and adhesion of T cells to tumor cells (Fig. 21b-II). After co-incubation with N_3-T cells, the survival rate of BCN-Luci-Raji cells decreased by nearly 60%, suggesting bioorthogonal reactions on cell surface also enhanced immune cytotoxicity against tumor cells (Fig. 21b-III). In addition, N_3-T cells incubated with BCN-Raji cells produced multiple cytokines, such as $TNF-\alpha$, interleukin-2 (IL-2) and interferon- γ (IFN- γ),

suggesting bioorthogonal reactions effectively activated T cells. This universal bioorthogonally glycometabolic labelling strategy not only expands applications of T cell immunotherapy but also offers a new and robust method to modify T cell.

In a similar work, Cai *et al.* utilized the chimeric antigen receptor-T (CAR-T) cell engineering strategy to improve curative results and decrease the side effects of clinical adoptive transfer of CAR-T cells (Fig. 22).²⁰⁷ CAR-T cells and tumor cells were respectively anchored with N_3 - and BCN-groups *via* the $Ac_4GalNAz$ and $Ac_4ManNBCN$ -mediated metabolic glycoengineering. Benefiting from bioorthogonal click chemistry, N_3/BCN groups on the cell surfaces strengthened the recognition interactions between CAR-T cells and tumor cells, leading to the deep penetration, increased accumulation and homing of CAR-T cells in tumor tissues. All these advantages jointly improved the therapeutic effect for solid tumor. This strategy holds a great potential to improve the curative effect of clinical CAR-T immunotherapy and avoid side effects in patients.

CAR-T therapy has shown great success in blood cancer, but its availability in solid tumors is limited due to the hostile microenvironment of solid tumors. Cai *et al.* developed a nanoengineered CAR-T strategy to improve the efficacy of solid tumor therapy (Fig. 23a).²⁰⁸ Indocyanine green nanoparticles (INPs) that served as a photosensitizer were conjugated onto CAR-T cells to generate CAR-T biohybrids (CT-INPs). Under NIR laser irradiation, CT-INPs destroyed the extracellular matrix, expanded blood vessels, loosened compact tissue, and stimulated chemokine secretion without weakening CAR-T cell activities.

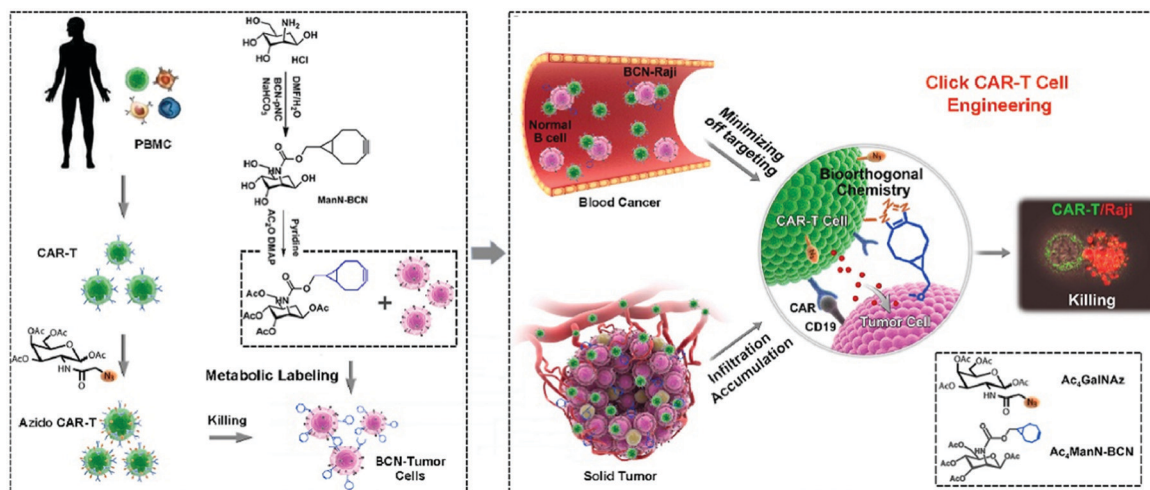


Fig. 22 Click CAR-T cell engineering strategy to improve tumor immunotherapy. Reproduced with the permission from ref. 207. Copyright 2020, Elsevier Ltd.

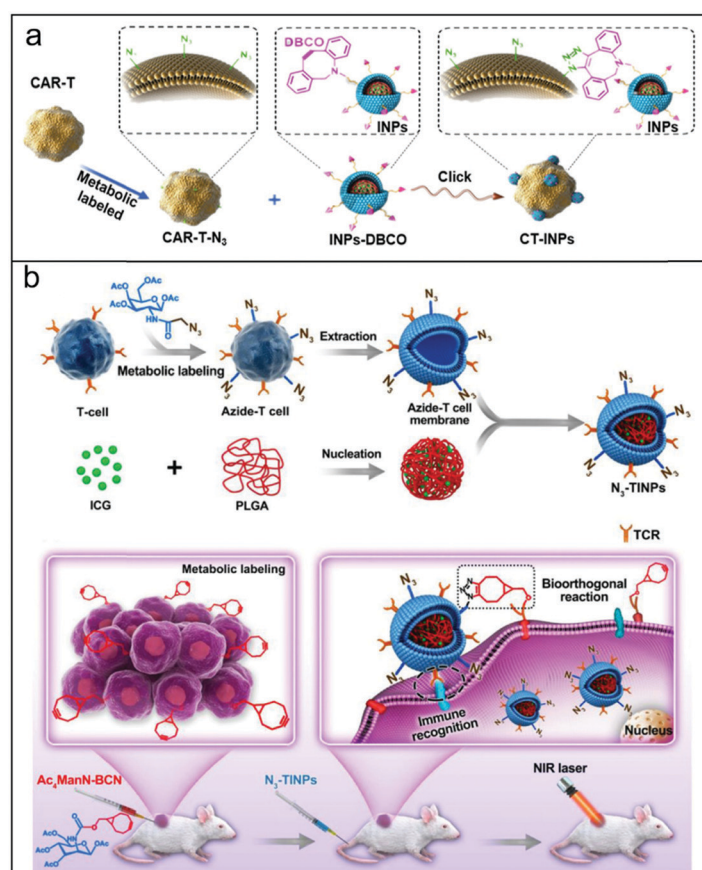


Fig. 23 (a) Nanoengineered CAR-T biohybrids to improve tumor immunotherapy. Reproduced with the permission from ref. 208. Copyright 2021, Wiley-VCH Verlag GmbH & Co. KGaA, Weinheim. (b) T cell mimicking dual-targeting nanomedicine to enhance PTT effect. Reproduced with the permission from ref. 209. Copyright 2019, Wiley-VCH Verlag GmbH & Co. KGaA, Weinheim.

These immune-favorable tumor microenvironments enhanced the infiltration and recruitment of CT-INPs and boosted CAR-T immunotherapeutic outcomes. This tumor microenvironment-remodelling CAR-T strategy provides reliable treatment guidance for solid tumor immunotherapy.

Due to the immune recognition receptors on the T cell surfaces, T cell membranes are promising targets for nanodrug carriers. Nevertheless, this single targeting strategy usually has low therapy efficacy owing to the heterogeneity of tumors. Cai *et al.* developed a dual-targeting strategy to enhance the

tumor accumulation of nanomedicines (Fig. 23b).²⁰⁹ With the assistance of metabolic glycoengineering, N_3 and BCN modified unnatural monosaccharide precursors incorporated N_3 and BCN groups onto surfaces of T cells and tumor cells respectively, to overcome the low therapy efficacy of single targeting strategy. INPs wrapped with N_3 anchored T cell membrane (N_3 -TINPs) could specifically target BCN receptors and natural antigens on tumor surfaces *via* bioorthogonal reactions and immune recognition. As expected, N_3 -TINPs not only brightly lit up tumors but also greatly increased the PTT effect of tumors. Hence, this T cell mimicking dual-targeting nanomedicine provides a new alternative targeting strategy to improve the therapy efficacy of PTT.

Chemical tools have been used to expand the functions of antibodies, such as cytotoxicity and molecular imaging capability. Recently, it is reported that changing the physical properties of antibodies can bring unique properties to antibodies.^{210,211} Urano *et al.* used bioorthogonal click reactions on

the surface of cells to induce surface-antibody aggregation, thus changing the functionalities and behaviors of antibodies (Fig. 24a-I).²¹² A series of clickable antibody linkers (AbCs) were constructed, in which BCN-, Tz- or methyltetrazine (MTz-) were conjugated onto *N*-hydroxysuccinimidyl ester (a site for protein labelling) *via* different length of PEG linkers (Fig. 24a-II). In the circulation medium, the click reactions between antibodies was adequately slow but became fast on the cell surfaces, so cross-linking reactions on cell surfaces were initiated. In HER2-expressing SKBR3 and trastuzumab system, cell growth was promoted (Fig. 24a-III), suggesting intracellular growth signaling was activated. Meanwhile, nuclear phospho-ERK signaling was also activated after antibody clicking (Fig. 24a-IV), demonstrating that the aggregation of antibodies caused the condensation of surface acceptors and triggered cross-phosphorylation. It is believed that this methodology can serve as a synthetic biology tool to regulate cellular fate in the future experimental and clinical stages.

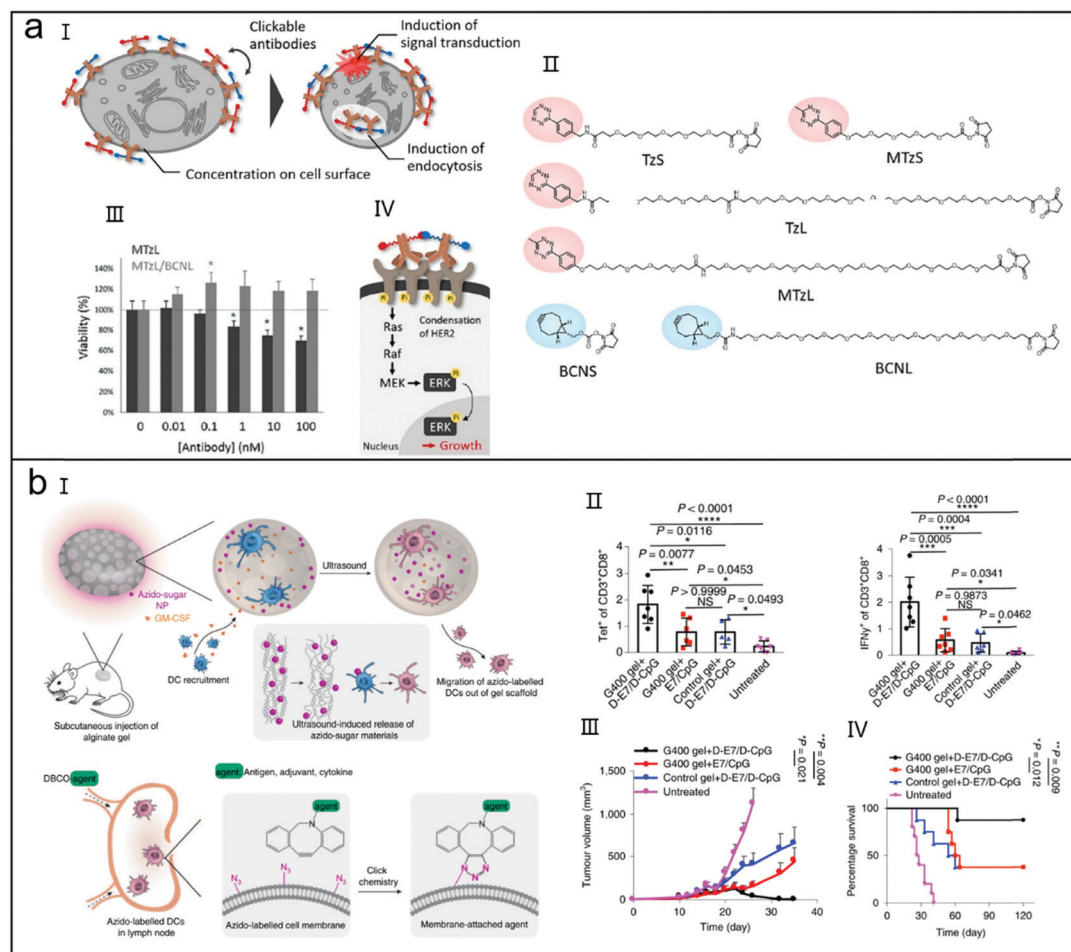


Fig. 24 (a) Bioorthogonal strategy to alter the functionalities of antibody. (I) Illustration of antibody cross-linking on the cell surface. (II) Structures of bioorthogonal reagents. (III) Viability assay of SKBR3 cells after treatment with MTzL or MTzL/BCNL for 48 h. (IV) Signal path of cell growth activated by antibody cross-linking. Reproduced with the permission from ref. 212. Copyright 2020, American Chemical Society. (b) Bioorthogonal strategy to regulate DCs. (I) Mechanism of DCs regulation. (II) Percentage of E7 tetramer⁺ cells (left) and IFN- γ ⁺ cells (right) among CD3⁺ T cells in PBMCs at day 16. (III) Tumor volume curves of mice in different groups. (IV) Survival curves of mice in different groups. Reproduced with the permission from ref. 215. Copyright 2020, Springer Nature Limited.

Dendritic cells (DCs) are crucial targets for tumor immunotherapies. DCs have been labelled by fluorescent dyes or radioelements to investigate their distribution,^{213,214} but DCs-specific labelling *in situ* followed by targeted immune modulation has not been reported. Mooney *et al.* used bioorthogonal reactions to conjugate DBCO-bearing immunomodulatory agents onto azide-labelled DCs to activate T cell and enhance immunotherapy (Fig. 24b-I).²¹⁵ Granulocyte-macrophage colony-stimulating factor (GM-CSF) and poly(azido-sugar)₄₀ (G400 NP) were simultaneously encapsulated in the biocompatible alginate gel to concentrate and bioorthogonally label DCs. The azide-labelled DCs specifically delivered DBCO-bearing immunomodulatory agents (cytokines, tumor antigens and adjuvants) towards T cells, thus DC-T cell interactions and T cell priming were activated, which enhanced tumor immunotherapy. Compared with control groups, a higher number of IFN- γ ⁺ CD8⁺ T cells and E7 tetramer⁺ CD8⁺ T cells were detected in DC/LNs-targeted cancer vaccine group (Fig. 24b-II), suggesting this DC/LNs-targeted strategy enhanced the vaccine effect. DC/LNs-targeted vaccine also efficiently suppressed tumor growth (Fig. 24b-III) and acquired the longest survival time (Fig. 24b-IV), indicating this strategy elicited good immunotherapy effect. As a result, this strategy could concentrate, label and track DCs to enhance DC-T cell interactions and boost the therapeutic effect of immunotherapy.

Because symbiotic stroma cells, such as tumor regulatory T cells (T_{reg}) and macrophages, play important roles in tumor progression, regulating their functionalities in the TME is an important step in cancer immunotherapy. Through TME immunomodulation, macrophage polarization (M2 to M1) can be induced and abundant intratumoral H₂O₂ can be generated. The increased H₂O₂ triggers the occurrence of the Fenton reaction,^{216,217} which can liberate antigens and activate the immunomodulatory response. Based on these ideas, Xie *et al.* constructed a biomimetic magnetosome (Pa-M/Ti-NC) to realize the synergism of immunomodulation and ferroptosis for cancer therapy (Fig. 25a-I).²¹⁸ In magnetosome system, Fe₃O₄ magnetic nanoclusters (MNCs) consisted of a magnetic core and a N₃-labelled leukocyte membrane. TGF- β inhibitor (Ti) was loaded in the leukocyte membrane and PD-1 antibody (Pa) was bioorthogonally anchored on the N₃-labelled membrane surface. In tumor tissues, Pa and Ti collectively created an immunogenic TME and induced the production of a great deal of H₂O₂. The increased H₂O₂ promoted the Fenton reaction and the generation of ROS. ROS initiated the lethal ferroptosis of tumor cells and triggered the release of tumor antigens, which in turn improved the immunogenicity of TME. The ratios of CD4⁺/Treg, CD8⁺/Treg and M1/M2 were greatly induced (Fig. 25a-II), and high level of H₂O₂ was detected (Fig. 25a-III) in the Pa-M/Ti-NC(m) group, suggesting the joint inhibition of Pa and Ti indeed created an immunogenic TME. Pa-M/Ti-NC(m) also completely suppressed tumor growth (Fig. 25a-IV) and led to a 50-day lifetime, suggesting the engineered magnetosomes had superior therapeutic performance as well as better biocompatibility. Excellent antitumor and antimetastatic performance were also achieved on a

metastatic tumor model (Fig. 25a-V), consolidating the superior therapeutic capacity of Pa-M/Ti-NC(m). No recurrence was observed (Fig. 25a-VI) during the therapeutic period, indicating the immunological memory effect was induced by Pa-M/Ti-NC(m) (Fig. 25a-VII). All of these results support that biomimetic magnetosomes can act as promising nanomedicines to safely and effectively fight against cancer.

The increasing knowledge of oncology and immunology has greatly promoted the development of versatile cancer vaccines. However, owing to the existence of efferent lymphatic vessels, vaccines easily flow out from lymph nodes, decreasing their presenting efficiency to antigen-presenting cells (APCs). The released antigens in APCs are always presented and processed with the major histocompatibility complex (MHC) II, meaning humoral immunity is mainly activated, but not for cellular immunity.^{219,220} Xie *et al.* developed a biomimetic magnetosome as an effective cancer nanovaccine (A/M/C-MNC) to enhance their presenting efficiency and cellular immunity (Fig. 25b-I).²²¹ With the help of electrostatic interactions, Toll-like receptor (TLR) agonists CpG-ODN (C) were adsorbed on the core of Fe₃O₄ MNCs, generating C-MNC. Then N₃-anchored cell membranes (M) were covered on the C-MNC, forming M/C-MNC. At last, DBCO-labelled anti-CD205 (A) was conjugated onto M/C-MNC *via* N₃/DBCO click reaction, leading to the formation of A/M/C-MNC. Owing to the superparamagnetism of Fe₃O₄ MNCs and antibody anchored membrane decoration, significant T cell proliferation with superior cytotoxic activity and clonal diversity could be achieved. Compared with other immune cells, the uptake of A/M/C-MNC in CD8⁺ DCs was the highest (Fig. 25b-II), indicating A/M/C-MNC nanovaccines were preferentially internalized by CD8⁺ DCs, which promoted the main MHC I cross-presentation. Furthermore, enhanced T cell division (Fig. 25b-III) and long lymph node retention time (4 weeks) were achieved (Fig. 25b-IV) in the A/M/C-MNC(m) group, suggesting the superparamagnetism of Fe₃O₄ MNCs was necessary for tumor elimination. The engineered nanovaccines displayed excellent anticancer and prognosis effects on five different tumor models, suggesting the anticancer immunocompetence was greatly activated by A/M/C-MNC. An over 80-days lifetime and a 100% survival rate were observed in different tumor models, suggesting the safety of the nanovaccines was high. Encouraged by these satisfactory results, the engineered magnetosomes can be considered as an ideal cancer vaccine with high safety for tumor therapy.

Because of the homology, exosomes can mimic the functions of their parent cells for cancer therapy.^{222,223} However, the therapeutic outcomes of exosomes *in vivo* are always unsatisfactory. Xie *et al.* developed a pH-responsive dual-targeting exosome (M1 Exo-Ab) to enhance the immunotherapy of tumors (Fig. 26a-I).²²⁴ Based on bioorthogonal reactions, anti-signal regulatory protein alpha (sIRP α) and anti-CD47 antibody (aCD47) were anchored onto M1 macrophage exosomes (M1 Exo) *via* a pH-responsive benzoic-imine bond, generating M1 Exo-Ab. Attributing to the targeting function of aCD47, M1 Exo-Ab selectively accumulated in CD47-overexpressing tumor cells. The low pH in tumor sites cleaved the benzoic-imine

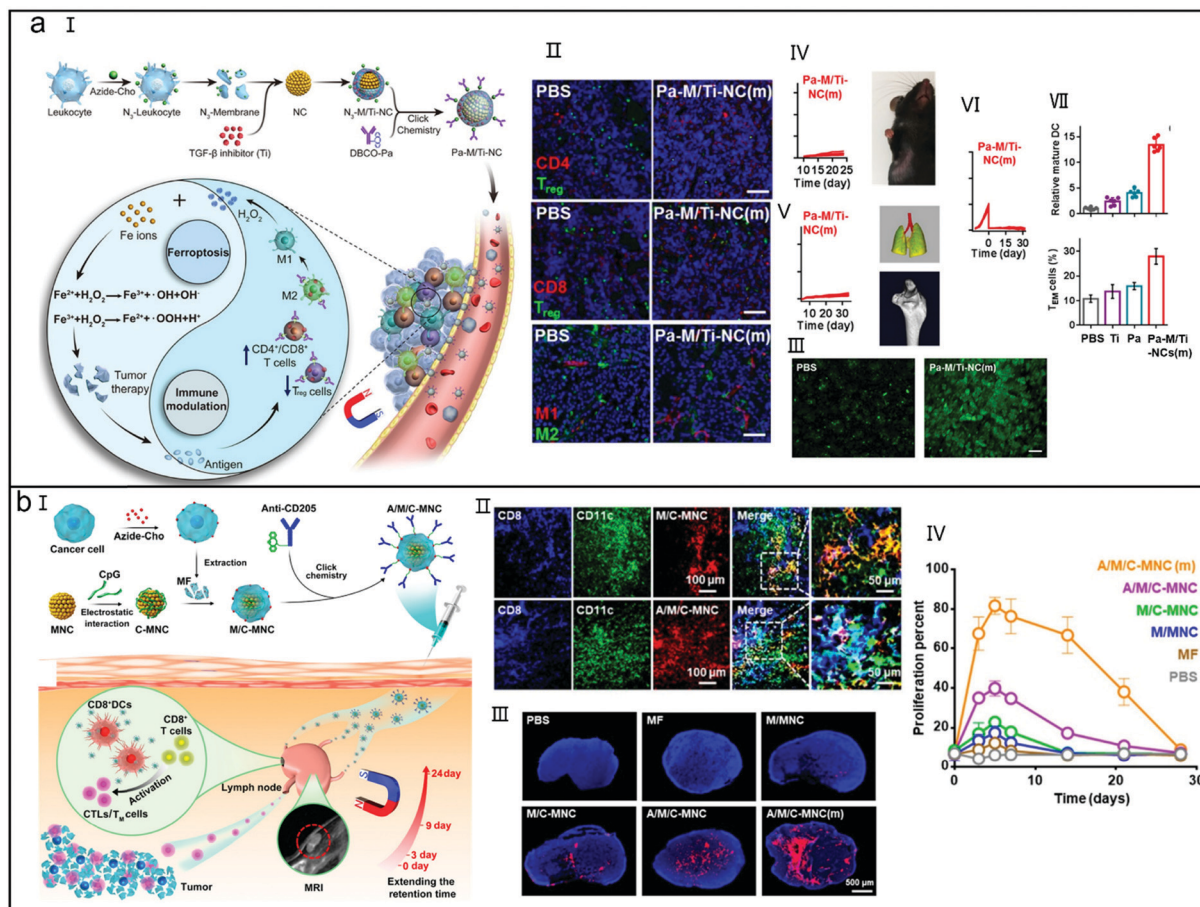


Fig. 25 (a) Biomimetic magnetosomes to enhance immunotherapy of cancer. (I) Mechanism of magnetosomes-based immunotherapy strategy. (II) Immunofluorescence images of tumor tissues after treatment with Pa-M/Ti-NCs(m). Scale bar: 100 μm . (III) CLSM images of hydroxyl radical (green) in tumor tissues after treatment with PBS or Pa-M/Ti-NCs(m). Scale bar: 10 μm . (IV) Tumor volume curves of Pa-M/Ti-NC(m) group and the representative CT images of bone metastasis and lung metastasis. (V) Tumor volume curves of Pa-M/Ti-NC(m) group. (VI) Percent of mature DCs in primary tumors and T_{EM} cells in the spleen of mice after different treatments. Reproduced with the permission from ref. 218. Copyright 2019, American Chemical Society. (b) Engineered magnetosomes for efficient cancer vaccination. (I) Mechanism of A/M/C-MNC-initiated cellular immune responses. (II) Fluorescence images of mouse lymph node after treatment with DiD-labeled M/C-MNC and A/M/C-MNC. (III) Immunohistochemical analysis of Ki67 expression in mouse lymph node (blue: DAPI; red: secondary antibody of Ki67). (IV) Proliferation analysis of cytotoxic T lymphocytes for 4 weeks after different treatments. Reproduced with the permission from ref. 221. Copyright 2019, American Chemical Society.

bond of M1 Exo-Ab to release aCD47 and aSIRP α , which subsequently blocked their corresponding receptors on macrophages or tumor cells respectively. As a result, tumor cells sent out “eat me” signals to macrophages to improve the cytophagy efficiency. Meanwhile, the native M1 Exo were able to reprogramme protumoral M2 macrophages into anti-tumoral M1 macrophages, further improving the anticancer efficacy of M1 Exo-Ab. Large numbers of 4T1 tumor cells were phagocytized by M2 macrophages in the M1 Exo-Ab group (Fig. 26a-II), suggesting M1 Exo-Ab was able to induce macrophage polarization. The antitumor efficacy of M1 Exo-Ab was also the best, and no lung metastasis and a high survival rate were acquired (Fig. 26a-III), demonstrating the high safety of M1 Exo-Ab for cancer immunotherapy. Because this synergistic strategy can be applied to various exosomes/ligands systems, a universal exosome-based platform for cancer immunotherapy can be constructed.

Owing to the immunosuppressed tumor microenvironment, the efficacy of immunotherapy is usually low. M2 type macrophages and microglia that support angiogenesis, tumor growth and immunosuppression, are the dominating ringleaders for the “cold” tumor microenvironment. Hence, reprogramming the phenotype of macrophages and microglia from M2 type to M1 type has a potential to break through the predicament of immunotherapy. Zhang *et al.* designed an erythrocyte membrane-cladded nucleic acid nanogel (Vir-Gel) which was decorated with M2pep and HA2 peptides to remodel the phenotype of immune cells and improve the effect of immunotherapy (Fig. 26b-I).²²⁵ With the help of M2pep and HA2 peptides, Vir-Gel could target to M2-macrophage and microglial cells. Then, miR155 was released from Vir-Gel under the catalysis of ribonuclease H (RNase H) and remodeled M2 immune cells to M1 type. Compared with control groups, Vir-Gel showed the best uptake efficiency (Fig. 26b-II), demonstrating that membrane

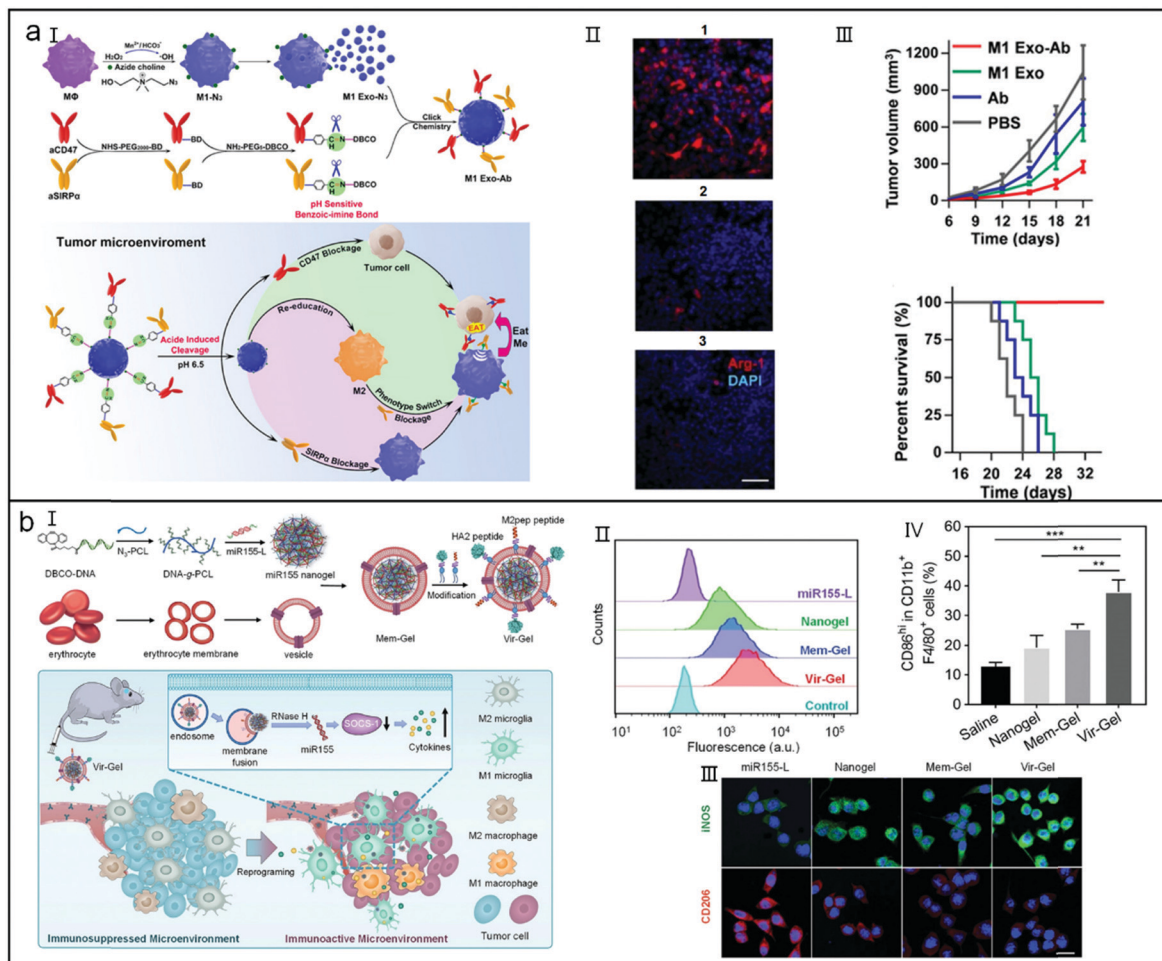


Fig. 26 (a) Engineered exosomes for cancer immunotherapy. (I) Mechanism of M1 Exo-Ab-based immune synergy effect. (II) CLSM images of Arginase-1 expression in M2 macrophages after different treatments (1: pristine M2; 2: M2 treated with M1 Exo; 3: M2 treated with M1 Exo-Ab). (III) Tumor volume curves and survival curves after different treatments. Scale bar: 100 μ m. Reproduced with the permission from ref. 224. Copyright 2020, Wiley-VCH Verlag GmbH & Co. KGaA, Weinheim. (b) A virus-like nucleic acid nanogel to enhance glioblastoma therapy. (I) Mechanism of glioblastoma immunotherapy of Vir-Gel. (II) FCM analysis of M2-type BV-2 cells after different treatments. (III) CLSM images of CD206 (M2 phenotype marker) and iNOS (M1 phenotype marker) expression in M2-type BV-2 cells after different treatments. (IV) Quantity analysis of M1 microglia and macrophages in tumors after different treatments. Scale bar: 20 μ m. Reproduced with the permission from ref. 225. Copyright 2021, Wiley-VCH Verlag GmbH & Co. KGaA, Weinheim.

coating and peptides decoration increased the cellular uptake of Vir-Gel. Meanwhile, the iNOS signal related to M1 type in M2-type BV-2 cells treated with Vir-Gel was improved (Fig. 26b-III), suggesting the ability of Vir-Gel to remodel immune cells. The amount of M2 immune cells in tumors in Vir-Gel group was remarkably decreased (Fig. 26b-IV), demonstrating Vir-Gel also efficiently remodeled immune cells *in vivo*. Due to the effective delivery capability and noninvasive feature, this virus-biomimetic nucleic acid nanogel provides a new direction for the development of tumor immune agents.

LN contain abundant APCs and lymphatic endothelial cells (LECs) which are ideal target cells for immunotherapeutic drugs, hence direct LN targeting strategy may be a promising approach to improve immunotherapy. Nie *et al.* developed a click chemistry-based active LN accumulation system (ALAS) to improve the accumulation of cancer vaccines in LNs and enhance tumor immunotherapy (Fig. 27a).²²⁶ Under the

albumin hitchhiking mechanism, azide groups were anchored on LECs, forming N_3 -LECs. OVA_{257–264} peptide (a model CD8⁺ T-cell epitope antigen) and poly(I:C) (a TLR agonist) were encapsulated in DBCO-conjugated liposomes (DL), generating DL-O/IC vaccine. With the help of N_3 /DBCO click reaction, DL-O/IC was specifically guided to LECs to improve tumor immunotherapy. Compared with control groups, DL-O/IC induced the highest levels of CD40⁺/CD80⁺/CD86⁺ BMDCs, SIINFEKL-H-2K^b cells, TNF- α and IL-6 expression (Fig. 27b), suggesting ALAS-based vaccines could be internalized by BMDCs and initiate antigen presentation and immune response. ALAS vaccine also efficiently inhibited metastasis (Fig. 27c) and suppressed the primary tumor growth (Fig. 27d), suggesting that ALAS vaccines could induce an impressive anticancer immune reaction *in vivo*. A high survival rate (Fig. 27e) and a long lifetime were also acquired in the ALAS vaccine group, indicating the adverse effect of ALAS vaccine was low. Being able to load other

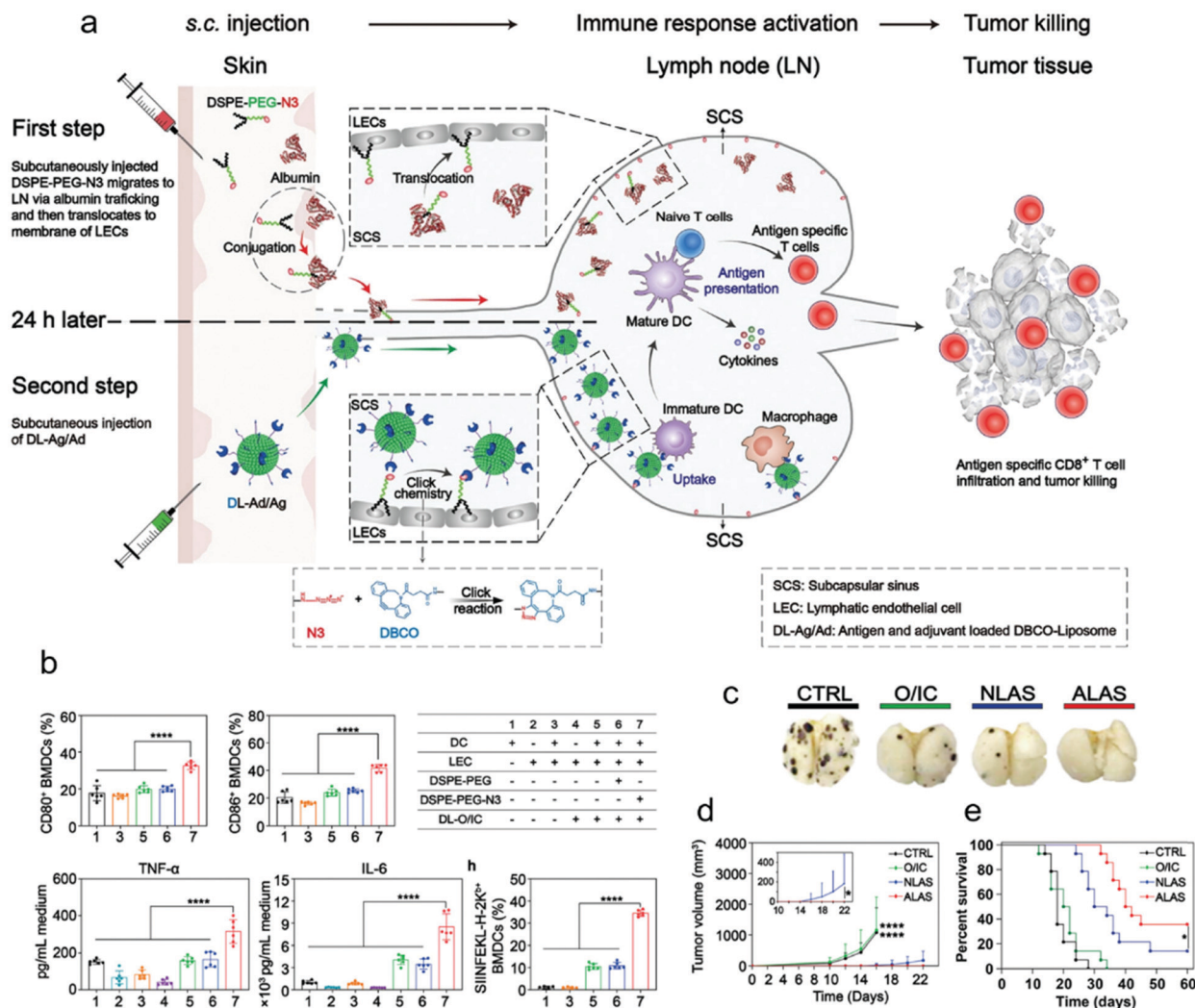


Fig. 27 (a) Therapy mechanism of LNs-targeted cancer vaccine. (b) FCM analysis of CD80⁺ and CD86⁺ cells and ELISA assay of cytokines (IL-6 and TNF- α) after different treatments. (c) The pictures of lung metastatic nodules in different groups. (d) Tumor growth curves of mice in different groups. (e) Survival curves of mice in different groups. Reproduced with the permission from ref. 226. Copyright 2021, Wiley-VCH Verlag GmbH & Co. KGaA, Weinheim.

versatile antigen peptides, ALAS vaccine provides a powerful platform for personalized cancer immune therapy.

4. Conclusions

In this review, a majority of fantastic research about metal-free bioorthogonal click chemistry in cancer theranostics have been summarized. Characterized by fast rate, high yield, non-poisonous by-product and aqueous reaction system, click chemistry can be introduced into living system without interference from surrounding environment.^{227–231} As an excellent partner of bioorthogonal chemistry, metabolic glycoengineering can anchor different chemical groups (such as -N₃, -SH and -CO-) onto the glycan backbone *via* inherent biosynthetic pathways.^{232–234} The common unnatural monosaccharides applied in metabolic glycoengineering are usually glucosamine,

galactosamine and mannosamine.^{235–241} The bioorthogonal glycometabolic labelling strategy^{242–246} can overcome the non-specific drug activation and limited tumor penetrability in traditional nanomedicines. Specifically, bioorthogonal groups can be firstly implanted on the targeting cell surface *via* metabolic glycoengineering, followed by the administration of prodrugs with complementary groups. After circulation, prodrugs rapidly react with the pretargeted bioorthogonal groups and are activated *in situ*. To enhance tumor penetrability of nanomedicines, two bioorthogonal methodologies are always employed. One is the construction of size-controllable macromolecular prodrugs which can be peeled into small nanoparticles in the tumor-specific microenvironment, such as low pH, redox and hypoxia.^{247–252} Because the small sized nanomedicines can easily reach the corners of tumor tissues and can be effectively phagocytized by tumor cells, they can significantly promote the final therapeutic performances. Another methodology

is to utilize the tumor-targeted properties of immune cells, such as DCs and T cells.^{253–257} As the key intermediaries of adaptive immune responses, DCs and T cells are important targets for cancer immunotherapies.^{258–262} Through bioorthogonally glycometabolic labelling strategy, immunomodulatory agents, such as antibodies, cytokines and vaccines, can be firmly anchored onto the surface of immune mediators and delivered to the T cells or tumor cells to stimulate a strong adaptive or cellular immune response for tumor inhibition.

Although bioorthogonal chemistry has brought tremendous progresses in cancer theranostics, there are still a number of challenges to be addressed. For example, in order to acquire high S/N signals or substantial drug concentration, high concentration of bioorthogonal agents is needed in target sites.^{263–267} However, due to the shortage of targeting groups or stimuli-responsiveness, most of the current bioorthogonally glycometabolic labelling strategies hardly ensure high concentration of bioorthogonal agents in tumor cells, so poor theranostic results and severe organ damage may be observed. In the following work, the concept of “enrichment triggered release” should be kept in mind to reduce the premature drug release in the drug delivery.^{268–270} In metabolic glycoengineering, unnatural monosaccharides with various click groups can be inserted into glycans on cell membrane. However, due to their fast metabolism, the half-life of these glycans is always short. For the long-time tracking of biological processes, this strategy is unserviceable. Hence, exploring new metabolic precursors and discovering the alternative way to prolong the half-life of glycans are urgently needed in near future. As a two-component approach, there are lots of key factors about bioorthogonally glycometabolic strategies needed to be considered, such as pharmacokinetic profile, stability, effective concentration, off-target effect and safety profile. Besides, the delayed time between the first and second components is undoubtedly another important factor. While the sorts of bioorthogonal chemistry have rapidly expanded recent years, there is still an urgent need for the new bioorthogonal reagents, especially those that can be directly used *in vivo*. Machine learning (ML), a vital component in artificial intelligence (AI), has been applied in many fields, such as drug discovery, cheminformatics and bioinformatics. With the fast development of organic chemistry, materials science and biomedical sciences, smart bioorthogonal reagents will spring up and provide vast amounts of data for ML. Meanwhile, ML will make accurate rules to guide the design of bioorthogonal reagents, greatly reducing cost and boosting efficacy.

Recently, bioorthogonal click chemistry has also been ingeniously utilized in the fields of mRNA and microneedle (MN). For example, the 5'-cap^{273,274} and m⁶A²⁷⁵ of eukaryotic mRNA were modified by bioorthogonal click chemistry to modulate cellular biological functions. Fluorescent labeling of the 5'-cap^{276,277} and the poly(A) tail²⁷⁸ of eukaryotic mRNA with the aid of bioorthogonal click chemistry not only realized the detection and localization of defined RNA strands inside living cells but also enhanced their translation. MN patches, as representative painless transdermal drug delivery systems, have

been utilized for many different biomedical applications. The combination of MN and bioorthogonal click chemistry can realize an *in situ* activation of diagnosis and treatment and avoid organ toxicity, having a great application prospect in the development of anticancer agents.²⁷⁹ With the increasing combination of advanced technology and bioorthogonal click chemistry, it is believed that more breakthrough in cancer theranostics will be realized, and more smart cancer nanomedicines will be approved in clinic in the near future.

Abbreviations

EPR effect	Enhanced permeability and retention effect
CuAAC	Copper-catalyzed azide–alkyne cycloaddition
SPAAC	Strain-promoted azide–alkyne cycloaddition
DIFO	Difluorinated cyclooctyne
TEC	Thiol–ene coupling
iEDDA	Inverse-electron demand Diels–Alder
TCO	<i>trans</i> -Cyclooctene
DBCO	Dibenzyl cyclooctyne
D-Cys	D-Cysteine
CBT	2-Cyanobenzothiazole
BCN	Bicyclo[6.1.0]nonyne
Tz	Tetrazine
MTz	Methyltetrazine
HIPS	Hydrazino-Pictet–Spengler
FI	Fluorescence imaging
MRI	Magnetic resonance imaging
PAI	Photoacoustic imaging
PET	Positron-emission tomography
RI	Raman imaging
PDT	Photodynamic therapy
PTT	Photothermal therapy
S/N	High signal to noise
Aha	Azidohomoalanine
Ac ₄ ManNAz	Tetraacetylated <i>N</i> -azidoacetyl-d-mannosamine
NIR	Near-infrared
FRET	Fluorescence resonance energy transfer
ACQ	Aggregation-caused quenching
SPICC	Strain-promoted iminosydnone–cycloalkyne cycloaddition
AIE	Aggregation-induced emission
AIEgens	AIE luminogens
TPE	Tetraphenylethene
D–A	Donor–acceptor
Ac ₄ GalNAz	<i>N</i> -Azidoacetylgalactosamine
ICG	Indocyanine green
PRE	Paramagnetic relaxation enhancement
CAS	Contrast agents
GGT	γ-Glutamyltranspeptidase
BBTB	Blood brain tumor barrier
BBB	Blood brain barrier
ALP	Alkaline phosphatase
CHQ	2-Cyano-6-hydroxyquinoline
STS	Soft tissue sarcoma

HDAC	Histone deacetylase
CTSL	Cathepsin L
ATTACK	Click chemistry-based tissue active targeting strategy
ADCs	Antibody–drug conjugates
Me ₂ Tz	3,6-Dimethyl-1,2,4,5-tetrazine
TPP	Triphenylphosphonium
CCR	Cyclization and release
TNF- α	Tumor necrosis factor- α
ALT	Alanine aminotransferase
ETR	Enrichment-triggered release
ADRs	Adverse drug reactions
EISA	Enzyme-instructed supramolecular self-assembly
TBET	Through-bond energy transfer
CRAIT	Click reaction-assisted immune cell targeting
MDR	Multidrug resistance
CSCs	Cancer stem-like cells
ATRA	All- <i>trans</i> retinoic acid
CPT	Camptothecin
HIF-1 α	Hypoxia-inducible factor-1 α
MCSs	Multicellular spheroids
EVs	Extracellular vesicles
UCNs	Upconversion nanocrystals
ChR2	Channelrhodopsins-2 protein
SPIO NPs	Superparamagnetic iron oxide nanoparticles
TME	Tumor microenvironment
ECM	Excessive extracellular matrix
RDT	Radiodynamic therapy
RT	Radiotherapy
NMOFs	Nanoscale metal organic frameworks
PSs	Photosensitizers
PRIT	Pretargeted radioimmunotherapy
IL-2	Interleukin-2
IFN- γ	Interferon- γ
CAR-T	Chimeric antigen receptor-T cell
DCs	Dendritic cells
T _{reg}	Tumor regulatory T cells
APCs	Antigen-presenting cells
TLR	Toll-like receptor
MHC	Major histocompatibility complex
aSIRP α	Anti-signal regulatory protein alpha
aCD47	Anti-CD47 antibody
RNase H	Ribonuclease H
LECs	Lymphatic endothelial cells

Conflicts of interest

There are no conflicts to declare.

Acknowledgements

This work was supported by the Zhejiang Provincial Natural Science Foundation of China (LQ20B040001 and LZ21E030002), the Tsinghua University Spring Breeze Fund (2021Z99CFZ007),

the startup funding by Tsinghua University, the National Natural Science Foundation of China (22175107), the Starry Night Science Fund of Zhejiang University Shanghai Institute for Advanced Study (SN-ZJU-SIAS-006), Shenzhen Bay Laboratory Startup Fund (21310071), National University of Singapore Startup Fund (NUHSRO/2020/133/Startup/08), and NUS School of Medicine Nanomedicine Translational Research Programme (NUHSRO/2021/034/TRP/09/Nanomedicine).

Notes and references

- J. W. Kim and C. V. Dang, *Cancer Res.*, 2006, **66**, 8927–8930.
- H. A. Idikio, *J. Cancer*, 2011, **2**, 107–115.
- M. Gao, F. B. Yu, C. J. Lv, J. Choo and L. X. Chen, *Chem. Soc. Rev.*, 2017, **46**, 2237–2271.
- F. Ye, Y. Zhao, R. El-Sayed, M. Muhammed and M. Hassan, *Nano Today*, 2018, **18**, 103–123.
- W. Tang, W. P. Fan, J. Lau, L. M. Deng, Z. Y. Shen and X. Y. Chen, *Chem. Soc. Rev.*, 2019, **48**, 2967–3014.
- V. Wagner, A. Dullaart, A.-K. Bock and A. Zweck, *Nat. Biotechnol.*, 2006, **24**, 1211–1217.
- K. Riehemann, S. W. Schneider, T. A. Luger, B. Godin, M. Ferrari and H. Fuchs, *Angew. Chem., Int. Ed.*, 2009, **48**, 872–897.
- Q. J. He, S. R. Guo, Z. Y. Qian and X. Y. Chen, *Chem. Soc. Rev.*, 2015, **44**, 6258–6286.
- M. I. Setyawati, C. Y. Tay, D. Docter, R. H. Stauber and D. T. Leong, *Chem. Soc. Rev.*, 2015, **44**, 8174–8199.
- C. Liang, L. G. Xu, G. S. Song and Z. Liu, *Chem. Soc. Rev.*, 2016, **45**, 6250–6269.
- G. D. Crozals, R. Bonnet, C. Farre and C. Chaix, *Nano Today*, 2016, **11**, 435–463.
- P. C. Zhang, Y. H. Zhai, Y. Cai, Y. L. Zhao and Y. P. Li, *Adv. Mater.*, 2019, **31**, 1904156.
- Z. Li, C. Xiao, T. Y. Yong, Z. F. Li, L. Gan and X. L. Yang, *Chem. Soc. Rev.*, 2020, **49**, 2273–2290.
- T. L. Doane and C. Burda, *Chem. Soc. Rev.*, 2012, **41**, 2885–2911.
- H. Maeda, H. Nakamura and J. Fang, *Adv. Drug Delivery Rev.*, 2013, **65**, 71–79.
- L. Tang and J. J. Cheng, *Nano Today*, 2013, **8**, 290–312.
- N. Bertrand, J. Wu, X. Y. Xu, N. Kamaly and O. C. Farokhzad, *Adv. Drug Delivery Rev.*, 2014, **66**, 2–25.
- L. Z. Feng, O. Betzer, D. L. Tao, T. Sadan, R. Popovtzer and Z. Liu, *CCS Chem.*, 2019, **1**, 239–250.
- Y. Zhang, C. Xu, X. L. Yang and K. Y. Pu, *Adv. Mater.*, 2020, **32**, 2002661.
- H. Cabral, Y. Matsumoto, K. Mizuno, Q. Chen, M. Murakami, M. Kimura, Y. Terada, M. R. Kano, K. Miyazono, M. Uesaka, N. Nishiyama and K. Kataoka, *Nat. Nanotechnol.*, 2011, **6**, 815–823.
- Y. Tsvetkova, N. Beztsinna, M. Baues, D. Klein, A. Rix, S. K. Golombek, W. A. Rawashdeh, F. Gremse, M. Barz, K. Koynov, S. Banala, W. Lederle, T. Lammers and F. Kies, *Nano Lett.*, 2017, **17**, 4665–4674.

- 22 B. L. Chen, W. B. Dai, B. He, H. Zhang, X. Q. Wang, Y. G. Wang and Q. Zhang, *Theranostics*, 2017, **7**, 538–558.
- 23 S. Y. Hua, J. He, F. P. Zhang, J. H. Yu, W. X. Zhang, L. Y. Gao, Y. Y. Li and M. Zhou, *Biomaterials*, 2020, **268**, 120590.
- 24 Y. Xie, Y. Hang, Y. Z. Wang, R. Sleightholm, D. R. Prajapati, J. Bader, A. Yu, W. M. Tang, L. Jaramillo, J. Li, R. K. Singh and D. Oupický, *ACS Nano*, 2020, **14**, 255–271.
- 25 Y. C. He, C. Cong, L. Li, L. Y. Luo, Y. Q. He, Z. N. Hao and D. W. Gao, *ACS Appl. Mater. Interfaces*, 2020, **12**, 8978–8988.
- 26 H. Lee, A. F. Shields, B. A. Siegel, K. D. Miller, I. Krop, C. X. Ma, P. M. LoRusso, P. N. Munster, K. Campbell, D. F. Gaddy, S. C. Leonard, E. Geretti, S. J. Blocker, D. B. Kirpotin, V. Moyo, T. J. Wickham and B. S. Hendriks, *Clin. Cancer Res.*, 2017, **23**, 4190–4202.
- 27 N. McGranahan and C. Swanton, *Cell*, 2017, **168**, 613–628.
- 28 R. K. Ramanathan, R. L. Korn, N. Raghunand, J. C. Sachdev, R. G. Newbold, G. Jameson, G. J. Fetterly, J. Prey, S. G. Klinz, J. Kim, J. Cain, B. S. Hendriks, D. C. Drummond, E. Bayever and J. B. Fitzgerald, *Clin. Cancer Res.*, 2017, **23**, 3638–3648.
- 29 D. A. Lawson, K. Kessenbrock, R. T. Davis, N. Pervolarakis and Z. Werb, *Nat. Cell Biol.*, 2018, **20**, 1349–1360.
- 30 I. Dagogo-Jack and A. T. Shaw, *Nat. Rev. Clin. Oncol.*, 2018, **15**, 81–94.
- 31 J. G. Reiter, M. Baretta, J. M. Gerold, A. P. Makohon-Moore, A. Daud, C. A. Iacobuzio-Donahue, N. S. Azad, K. W. Kinzler, M. A. Nowak and B. Vogelstein, *Nat. Rev. Cancer*, 2019, **19**, 639–650.
- 32 A. Marusyk, M. Janiszewska and K. Polyak, *Cancer Cell*, 2020, **37**, 471–484.
- 33 C. Chiappini, E. D. Rosa, J. O. Martinez, X. Liu, J. Steele, M. M. Stevens and E. Tasciotti, *Nat. Mater.*, 2015, **14**, 532–539.
- 34 G. H. Lu, F. Li, F. Zhang, L.-L. Huang, L. J. Zhang, Y. Lv, W. Wei and H. Y. Xie, *Adv. Funct. Mater.*, 2018, **28**, 1707596.
- 35 T. J. Ji, J. Y. Lang, B. Ning, F. F. Qi, H. Wang, Y. L. Zhang, R. F. Zhao, X. Yang, L. J. Zhang, W. Li, X. H. Shi, Z. H. Qin, Y. Zhao and G. J. Nie, *Adv. Mater.*, 2019, **31**, e1804395.
- 36 G. N. Liu, X. Zhao, Y. L. Zhang, J. C. Xu, J. Q. Xu, Y. Li, H. Min, J. Shi, Y. Zhao, J. Y. Wei, J. Wang and G. J. Nie, *Adv. Mater.*, 2019, **31**, e1900795.
- 37 Y. C. Ma, Y. Y. Zhao, N. K. Bejjanki, X. F. Tang, W. Jiang, J. X. Dou, M. I. Khan, Q. Wang, J. X. Xia, H. Liu, Y.-Z. You, G. Q. Zhang, Y. C. Wang and J. Wang, *ACS Nano*, 2019, **13**, 8890–8902.
- 38 X. Z. Ai, J. Mu and B. G. Xing, *Theranostics*, 2016, **6**, 2439–2457.
- 39 Y. Tan, K. He, B. Tang, H. R. Chen, Z. P. Zhao, C. Q. Zhang, L. Lin and J. B. Liu, *ACS Nano*, 2020, **14**, 13975–13985.
- 40 H. Cabral, H. Kinoh and K. Kataoka, *Acc. Chem. Res.*, 2020, **53**, 2765–2776.
- 41 M. Molina, M. Asadian-Birjand, J. Balach, J. Bergueiro, E. Miceli and M. Calderón, *Chem. Soc. Rev.*, 2015, **44**, 6161–6186.
- 42 S. Wang, P. Huang and X. Y. Chen, *ACS Nano*, 2016, **10**, 2991–2994.
- 43 L. Zhou, H. Wang and Y. P. Li, *Theranostics*, 2018, **8**, 1059–1074.
- 44 M. Ovais, S. Mukherjee, A. Pramanik, D. Das, A. Mukherjee, A. Raza and C. Y. Chen, *Adv. Mater.*, 2020, **32**, e2000055.
- 45 L. Li, Z. Yang and X. Y. Chen, *Acc. Chem. Res.*, 2020, **53**, 2044–2054.
- 46 D. Wu, S. Wang, G. C. Yu and X. Y. Chen, *Angew. Chem., Int. Ed.*, 2021, **60**, 8018–8034.
- 47 C. Luo, J. Sun, B. J. Sun and Z. G. He, *Trends Pharmacol. Sci.*, 2014, **35**, 556–566.
- 48 C. Luo, J. Sun, B. J. Sun, D. Liu, L. Miao, T. J. Goodwin, L. Huang and Z. G. He, *Small*, 2016, **12**, 6353–6362.
- 49 J. J. Shi, P. W. Kantoff, R. Wooster and O. C. Farokhzad, *Nat. Rev. Cancer*, 2017, **17**, 20–37.
- 50 Z. F. Li, C. Z. Di, S. P. Li, X. L. Yang and G. J. Nie, *Acc. Chem. Res.*, 2019, **52**, 2703–2712.
- 51 Q. Liu, J. Q. Cai, Y. D. Zheng, Y. L. Tan, Y. F. Wang, Z. Z. Zhang, C. X. Zheng, Y. Zhao, C. Y. Liu, Y. L. An, C. L. Jiang, L. Q. Shi, C. S. Kang and Y. Liu, *Nano Lett.*, 2019, **19**, 7662–7672.
- 52 L.-Q. Zhou, P. Li, X.-W. Cui and C. F. Dietrich, *Cancer Lett.*, 2020, **470**, 204–219.
- 53 J. H. Ryu, H. Y. Yoon, I.-C. Sun, I. C. Kwon and K. Kim, *Adv. Mater.*, 2020, **32**, e2002197.
- 54 Q. J. He, D. O. Kiesewetter, Y. Qu, X. Fu, J. Fan, P. Huang, Y. J. Liu, G. Z. Zhu, Y. Liu, Z. Y. Qian and X. Y. Chen, *Adv. Mater.*, 2015, **27**, 6741–6746.
- 55 C. Luo, J. Sun, D. Liu, B. J. Sun, L. Miao, S. Musetti, J. Li, X. P. Han, Y. Q. Du, L. Li, L. Huang and Z. G. He, *Nano Lett.*, 2016, **16**, 5401–5408.
- 56 B. J. Sun, C. Luo, H. Yu, X. B. Zhang, Q. Chen, W. Q. Yang, M. L. Wang, Q. M. Kan, H. T. Zhang, Y. J. Wang, Z. G. He and J. Sun, *Nano Lett.*, 2018, **18**, 3643–3650.
- 57 B. J. Sun, C. Luo, X. B. Zhang, M. R. Guo, M. C. Sun, H. Yu, Q. Chen, W. Q. Yang, M. L. Wang, S. Y. Zuo, P. Y. Chen, Q. M. Kan, H. T. Zhang, Y. J. Wang, Z. G. He and J. Sun, *Nat. Commun.*, 2019, **10**, 3211.
- 58 B. J. Sun, Y. Chen, H. Yu, C. Wang, X. B. Zhang, H. Q. Zhao, Q. Chen, Z. G. He, C. Luo and J. Sun, *Acta Biomater.*, 2019, **92**, 219–228.
- 59 P. Xue, J. Wang, X. F. Han and Y. J. Wang, *Colloids Surf., B*, 2019, **180**, 202–211.
- 60 J. Li and P. R. Chen, *Nat. Chem. Biol.*, 2016, **12**, 129–137.
- 61 S. Alonso-de Castro, E. Ruggiero, A. Ruiz-de-Angulo, E. Rezabal, J. C. Mareque-Rivas, X. Lopez, F. López-Gallego and L. Salassa, *Chem. Sci.*, 2017, **8**, 4619–4625.
- 62 J. Rautio, N. A. Meanwell, L. Di and M. J. Hageman, *Nat. Rev. Drug Discovery*, 2018, **17**, 559–587.
- 63 X. Y. Ji and B. H. Wang, *Acc. Chem. Res.*, 2018, **51**, 1377–1385.
- 64 X. Y. Ji, Z. X. Pan, B. C. Yu, L. K. D. L. Cruz, Y. Q. Zheng, B. Ke and B. Wang, *Chem. Soc. Rev.*, 2019, **48**, 1077–1094.
- 65 A. D. Corso, V. Borlandelli, C. Corno, P. Perego, L. Belvisi, L. Pignataro and C. Gennari, *Angew. Chem., Int. Ed.*, 2020, **59**, 4176–4181.

- 66 E. Saxon and C. R. Bertozzi, *Science*, 2000, **287**, 2007–2010.
- 67 H. Nandivada, X. W. Jiang and J. Lahann, *Adv. Mater.*, 2007, **19**, 2197–2208.
- 68 C. R. Becer, R. Hoogenboom and U. S. Schubert, *Angew. Chem., Int. Ed.*, 2009, **48**, 4900–4908.
- 69 E. M. Sletten and C. R. Bertozzi, *Acc. Chem. Res.*, 2011, **44**, 666–676.
- 70 Q. Li, T. Dong, X. H. Liu and X. G. Lei, *J. Am. Chem. Soc.*, 2013, **135**, 4996–4999.
- 71 J. S. Guo, Z. W. Xie, R. T. Tran, D. H. Xie, D. D. Jin, X. C. Bai and J. Yang, *Adv. Mater.*, 2014, **26**, 1906–1911.
- 72 E. M. Sletten and C. R. Bertozzi, *Angew. Chem., Int. Ed.*, 2009, **48**, 6974–6998.
- 73 M. F. Debets, S. S. van Berkel, J. Dommerholt, A. T. J. Dirks, F. P. J. T. Rutjes and F. L. van Delft, *Acc. Chem. Res.*, 2011, **44**, 805–815.
- 74 J. Li, J. T. Yu, J. Y. Zhao, J. Wang, S. Q. Zheng, S. X. Lin, L. Chen, M. Y. Yang, S. Jia, X. Y. Zhang and P. R. Chen, *Nat. Chem.*, 2014, **6**, 352–361.
- 75 B. L. Oliveira, Z. Guo and G. J. L. Bernardes, *Chem. Soc. Rev.*, 2017, **46**, 4895–4950.
- 76 B. W. Li, X. Xie, Z. L. Chen, C. Y. Zhan, F. Zeng and S. Z. Wu, *Adv. Funct. Mater.*, 2018, **28**, 1800692.
- 77 R. D. Row and J. A. Prescher, *Acc. Chem. Res.*, 2018, **51**, 1073–1081.
- 78 K. K.-W. Lo, *Acc. Chem. Res.*, 2020, **53**, 32–44.
- 79 C. G. Parker and M. R. Pratt, *Cell*, 2020, **180**, 605–632.
- 80 E. Latocheski, G. M. D. Forno, T. M. Ferreira, B. L. Oliveira, G. J. L. Bernardes and J. B. Domingos, *Chem. Soc. Rev.*, 2020, **49**, 7710–7729.
- 81 M. Köhn and R. Breinbauer, *Angew. Chem., Int. Ed.*, 2004, **43**, 3106–3116.
- 82 F. L. Lin, H. M. Hoyt, H. van Halbeek, R. G. Bergman and C. R. Bertozzi, *J. Am. Chem. Soc.*, 2005, **127**, 2686–2695.
- 83 C. I. Schilling, N. Jung, M. Biskup, U. Schepers and S. Bräse, *Chem. Soc. Rev.*, 2011, **40**, 4840–4871.
- 84 S. S. van Berkel, M. B. van Eldijk and J. C. M. van Hest, *Angew. Chem., Int. Ed.*, 2011, **50**, 8806–8827.
- 85 C. Bednarek, I. Wehl, N. Jung, U. Schepers and S. Bräse, *Chem. Rev.*, 2020, **120**, 4301–4354.
- 86 H. C. Kolb, M. G. Finn and K. B. Sharpless, *Angew. Chem., Int. Ed.*, 2001, **40**, 2004–2021.
- 87 C. S. McKay and M. G. Finn, *Chem. Biol.*, 2014, **21**, 1075–1101.
- 88 V. V. Rostovtsev, L. G. Green, V. V. Fokin and K. B. Sharpless, *Angew. Chem., Int. Ed.*, 2002, **41**, 2596–2599.
- 89 C. W. Tornøe, C. Christensen and M. Meldal, *J. Org. Chem.*, 2002, **67**, 3057–3064.
- 90 J. M. Baskin, J. A. Prescher, S. T. Laughlin, N. J. Agard, P. V. Chang, I. A. Miller, A. Lo, J. A. Codelli and C. R. Bertozzi, *Proc. Natl. Acad. Sci. U. S. A.*, 2007, **104**, 16793–16797.
- 91 E. M. Sletten and C. R. Bertozzi, *Org. Lett.*, 2008, **10**, 3097–3099.
- 92 K. E. Beatty, J. D. Fisk, B. P. Smart, Y. Y. Lu, J. Szychowski, M. J. Hangauer, J. M. Baskin, C. R. Bertozzi and D. A. Tirrell, *ChemBioChem*, 2010, **11**, 2092–2095.
- 93 E. M. Valkevich, R. G. Guenette, N. A. Sanchez, Y.-C. Chen, Y. Ge and E. R. Strieter, *J. Am. Chem. Soc.*, 2012, **134**, 6916–6919.
- 94 A. Dondoni and A. Marra, *Chem. Soc. Rev.*, 2012, **41**, 573–586.
- 95 F. Wojcik, A. G. O'Brien, S. Götze, P. H. Seeberger and L. Hartmann, *Chemistry*, 2013, **19**, 3090–3098.
- 96 G. Povie, A.-T. Tran, D. Bonnaffé, J. Habegger, Z. Y. Hu, C. L. Narvor and P. Renaud, *Angew. Chem., Int. Ed.*, 2014, **53**, 3894–3898.
- 97 R. Alonso, P. Jiménez-Meneses, J. García-Rupérez, M.-J. Bañuls and Á. Maquieira, *Chem. Commun.*, 2018, **54**, 6144–6147.
- 98 A. Dondoni, *Angew. Chem., Int. Ed.*, 2008, **47**, 8995–8997.
- 99 M. L. Blackman, M. Royzen and J. M. Fox, *J. Am. Chem. Soc.*, 2008, **130**, 13518–13519.
- 100 N. K. Devaraj, R. Weissleder and S. A. Hilderbrand, *Bioconjugate Chem.*, 2008, **19**, 2297–2299.
- 101 C. Freidel, S. Kaloyanova and K. Peneva, *Amino Acids*, 2016, **48**, 1357–1372.
- 102 G. L. Liang, H. J. Ren and J. H. Rao, *Nat. Chem.*, 2010, **2**, 54–60.
- 103 H. J. Ren, F. Xiao, K. Zhan, Y.-P. Kim, H. X. Xie, Z. Y. Xia and J. H. Rao, *Angew. Chem., Int. Ed.*, 2009, **48**, 9658–9662.
- 104 Y. Yuan and G. L. Liang, *Org. Biomol. Chem.*, 2014, **12**, 865–871.
- 105 M. Zhou, J. Hu, M. M. Zheng, Q. H. Song, J. B. Li and Y. Zhang, *Chem. Commun.*, 2016, **52**, 2342–2345.
- 106 K. Huang, Y. H. He, Z. H. Zhu, J. K. Guo, G. L. Wang, C. Deng and Z. Y. Zhong, *ACS Appl. Mater. Interfaces*, 2019, **11**, 22171–22180.
- 107 W. J. Song, Y. Z. Wang, J. Qu, M. M. Madden and Q. Lin, *Angew. Chem., Int. Ed.*, 2008, **47**, 2832–2835.
- 108 J. Stöckigt, A. P. Antonchick, F. R. Wu and H. Waldmann, *Angew. Chem., Int. Ed.*, 2011, **50**, 8538–8564.
- 109 P. Agarwal, J. van der Weijden, E. M. Sletten, D. Rabuka and C. R. Bertozzi, *Proc. Natl. Acad. Sci. U. S. A.*, 2013, **110**, 46–51.
- 110 S. Pomplun, M. Y. H. Mohamed, T. Oelschlaegel, C. Wellner and F. Bergmann, *Angew. Chem., Int. Ed.*, 2019, **58**, 3542–3547.
- 111 X. Sheng and F. Himo, *J. Am. Chem. Soc.*, 2019, **141**, 11230–11238.
- 112 C. Zheng and S.-L. You, *Acc. Chem. Res.*, 2020, **53**, 974–987.
- 113 P. Agarwal, R. Kudirka, A. E. Albers, R. M. Barfeld, G. W. de Hart, P. M. Drake, L. C. Jones and D. Rabuka, *Bioconjugate Chem.*, 2013, **24**, 846–851.
- 114 J. A. Nicholas, J. A. Prescher and C. R. Bertozzi, *J. Am. Chem. Soc.*, 2004, **126**, 15046–15047.
- 115 D. C. Kennedy, C. S. McKay, M. C. B. Legault, D. C. Danielson, J. A. Blake, A. F. Pegoraro, A. Stolow, Z. Mester and J. P. Pezacki, *J. Am. Chem. Soc.*, 2011, **133**, 17993–18001.
- 116 V. Bevilacqua, M. King, M. Chaumontet, M. Nothisen, S. Gabillet, D. Buisson, C. Puente, A. Wagner and F. Taran, *Angew. Chem., Int. Ed.*, 2014, **53**, 5872–5876.

- 117 R. Manova, T. A. van Beek and H. Zuilhof, *Angew. Chem., Int. Ed.*, 2011, **50**, 5428–5430.
- 118 S. B. Lee, H. L. Kim, H.-J. Jeong, S. T. Lim, M.-H. Sohn and D. W. Kim, *Angew. Chem., Int. Ed.*, 2013, **52**, 10549–10552.
- 119 K. Xiong, W. Wei, Y. J. Jin, S. M. Wang, D. X. Zhao, S. Wang, X. Y. Gao, C. M. Qiao, H. Yue, G. H. Ma and H.-Y. Xie, *Adv. Mater.*, 2016, **28**, 7929–7935.
- 120 F. Hu, D. Mao, Kenry, X. L. Cai, W. B. Wu, D. L. Kong and B. Liu, *Angew. Chem., Int. Ed.*, 2018, **57**, 10182–10186.
- 121 Z. Y. He, S. Peng, Q. Wei, S. K. Jia, S. Guo, K. Chen and X. Zhou, *CCS Chem.*, 2020, **2**, 89–97.
- 122 M. Boyce, I. S. Carrico, A. S. Ganguli, S.-H. Yu, M. J. Hangauer, S. C. Hubbard, J. J. Kohler and C. R. Bertozzi, *Proc. Natl. Acad. Sci. U. S. A.*, 2011, **108**, 3141–3146.
- 123 S. T. Laughlin, J. M. Baskin, S. L. Amacher and C. R. Bertozzi, *Science*, 2008, **320**, 664–667.
- 124 H. Koo, S. Lee, J. H. Na, S. H. Kim, S. K. Hahn, K. Choi, I. C. Kwon, S. Y. Jeong and K. Kim, *Angew. Chem., Int. Ed.*, 2012, **51**, 11836–11840.
- 125 E. H. P. Leunissen, M. H. L. Meuleners, J. M. M. Verkade, J. Dommerholt, J. G. J. Hoenderop and F. L. van Delft, *ChemBioChem*, 2014, **15**, 1446–1451.
- 126 U. Rieder and N. W. Luedtke, *Angew. Chem., Int. Ed.*, 2014, **53**, 9168–9172.
- 127 Z. J. Hai, J. J. Wu, D. Saimi, Y. H. Ni, R. B. Zhou and G. L. Liang, *Anal. Chem.*, 2018, **90**, 1520–1524.
- 128 A. Dragulescu-Andrasi, S. R. Kothapalli, G. A. Tikhomirov, J. Rao and S. S. Gambhir, *J. Am. Chem. Soc.*, 2013, **135**, 11015–11022.
- 129 K. Porte, B. Renoux, E. Péraudeau, J. Clarhaut, B. Eddhif, P. Poinot, E. Gravel, E. Doris, A. Wijkhuisen, D. Audisio, S. Papot and F. Taran, *Angew. Chem., Int. Ed.*, 2019, **58**, 6366–6370.
- 130 J. B. Li, H. Kong, L. Huang, B. Cheng, K. Qin, M. M. Zheng, Z. Yan and Y. Zhang, *J. Am. Chem. Soc.*, 2018, **140**, 14542–14546.
- 131 C. Liu, C. Z. Sun, H. N. Huang, K. Janda and T. Edgington, *Cancer Res.*, 2003, **63**, 2957–2964.
- 132 Y. P. Luo, H. Zhou, J. Krueger, C. Kaplan, S. H. Lee, C. Dolman, D. Markowitz, W. Y. Wu, C. Liu, R. A. Reisfeld and R. J. Xiang, *Clin. Invest.*, 2006, **116**, 2132–2141.
- 133 Y. Zhao, Z. J. Hai, H. Y. Wang, L. H. Su and G. L. Liang, *Anal. Chem.*, 2018, **90**, 8732–8735.
- 134 J.-S. Ni, P. F. Zhang, T. Jiang, Y. C. Chen, H. F. Su, D. Wang, Z.-Q. Yu, R. T. K. Kwok, Z. J. Zhao, J. W. Y. Lam and B. Z. Tang, *Adv. Mater.*, 2018, **30**, e1805220.
- 135 P. F. Zhang, T. Jiang, Y. Y. Li, Z. Zhao, P. Gong, L. T. Cai, R. T. K. Kwok, J. W. Y. Lam, X. G. Gu and B. Z. Tang, *Chem. – Asian J.*, 2019, **14**, 770–774.
- 136 X. H. Zhang, B. Wang, N. Zhao, Z. H. Tian, Y. P. Dai, Y. Z. Nie, J. Tian, Z. L. Wang and X. Y. Chen, *Theranostics*, 2017, **7**, 3794–3802.
- 137 E. Ren, C. C. Chu, Y. M. Zhang, J. Q. Wang, X. Pang, X. N. Lin, C. Liu, X. X. Shi, Q. X. Dai, P. Lv, X. M. Wang, X. Y. Chen and G. Liu, *Small Methods*, 2020, **4**, 2000291.
- 138 H. Li, J. Conde, A. Guerreiro and G. J. L. Bernardes, *Angew. Chem., Int. Ed.*, 2020, **59**, 16023–16032.
- 139 W. Y. Mao, J. Tang, L. Q. Dai, X. Y. He, J. Li, L. Cai, P. Liao, R. T. Jiang, J. W. Zhou and H. X. Wu, *Angew. Chem., Int. Ed.*, 2021, **60**, 2393–2397.
- 140 Q.-D. Nguyen, G. Smith, M. Glaser, M. Perumal, E. Arstad and E. O. Aboagye, *Proc. Natl. Acad. Sci. U. S. A.*, 2009, **106**, 16375–16380.
- 141 L. E. Edgington, A. B. Berger, G. Blum, V. E. Albrow, M. G. Paulick, N. Lineberry and M. Bogoyo, *Nat. Med.*, 2009, **15**, 967–973.
- 142 J. R. Johnson, B. Kocher, E. M. Barnett, J. Marasa and D. Piwnicka-Worms, *Bioconjugate Chem.*, 2012, **23**, 1783–1793.
- 143 D. J. Ye, A. J. Shuhendler, L. N. Cui, L. Tong, S. S. Tee, G. Tikhomirov, D. W. Felsher and J. H. Rao, *Nat. Chem.*, 2014, **6**, 519–526.
- 144 A. A. Neves, Y. A. Wainman, A. Wright, M. I. Kettunen, T. B. Rodrigues, S. McGuire, D.-E. Hu, F. Bulat, S. G. Crich, H. Stöckmann, F. J. Leeper and K. M. Brindle, *Angew. Chem., Int. Ed.*, 2016, **55**, 1286–1290.
- 145 E. J. L. Stéen, J. T. Jørgensen, K. Johann, K. Nørregaard, B. Sohr, D. Svatunek, A. Birke, V. Shalgunov, P. E. Edem, R. Rossin, C. Seidl, F. Schmid, M. S. Robillard, J. L. Kristensen, H. Mikula, M. Barz, A. Kjær and M. M. Herth, *ACS Nano*, 2020, **14**, 568–584.
- 146 Z. L. Ding, H. B. Sun, S. C. Ge, Y. Cai, Y. Yuan, Z. J. Hai, T. X. Tao, J. M. Hu, B. Hu, J. F. Wang and G. L. Liang, *Adv. Funct. Mater.*, 2019, **29**, 1903860.
- 147 Z. J. Hai, Y. H. Ni, D. Saimi, H. Y. Yang, H. Y. Tong, K. Zhong and G. L. Liang, *Nano Lett.*, 2019, **19**, 2428–2433.
- 148 Y. K. Duan, M. Wu, D. H. Hu, Y. T. Pan, F. Hu, X. G. Liu, N. Thakor, W. H. Ng, X. Liu, Z. H. Sheng, H. R. Zheng and B. Liu, *Adv. Funct. Mater.*, 2020, **30**, 2004346.
- 149 C. F. Wu, R. Zhang, W. Du, L. Cheng and G. L. Liang, *Nano Lett.*, 2018, **18**, 7749–7754.
- 150 H. Y. Wang, P. Y. Chen, H. Wu, P. Zou, J. Wu, Y. L. Liu and G. L. Liang, *Anal. Chem.*, 2019, **91**, 14842–14845.
- 151 Y. Yuan, P. Raj, J. Zhang, S. Siddhanta, I. Barman and J. W. M. Bulte, *Angew. Chem., Int. Ed.*, 2021, **60**, 3923–3927.
- 152 R. Mahato, W. Tai and K. Cheng, *Adv. Drug Delivery Rev.*, 2011, **63**, 659–670.
- 153 S. S. Matikonda, D. L. Orsi, V. Staudacher, I. A. Jenkins, F. Fiedler, J. Y. Chen and A. B. Gamble, *Chem. Sci.*, 2015, **6**, 1212–1218.
- 154 M. A. Clark, C. Fisher, I. Judson and J. M. Thomas, *N. Engl. J. Med.*, 2005, **353**, 701–711.
- 155 M. F. Brennan, C. R. Antonescu, N. Moraco and S. Singer, *Ann. Surg.*, 2014, **260**, 416–421.
- 156 J. M. M. Oneto, I. Khan, L. Seebald and M. Royzen, *ACS Cent. Sci.*, 2016, **2**, 476–482.
- 157 M. C. Raff, K. L. Fields, S. I. Hakomori, R. Mirsky, R. M. Pruss and J. Winter, *Brain Res.*, 1979, **174**, 283–308.
- 158 Z. Nusser, R. Lujan, G. Laube, J. D. Roberts, E. Molnar and P. Somogyi, *Neuron*, 1998, **21**, 545–559.
- 159 S. Cull-Candy, S. Brickley and M. Farrant, *Curr. Opin. Neurobiol.*, 2001, **11**, 327–335.
- 160 H. Wang, R. B. Wang, K. M. Cai, H. He, Y. Liu, J. Yen, Z. Y. Wang, M. Xu, Y. W. Sun, X. Zhou, Q. Yin, L. Tang,

- I. T. Dobrucki, L. W. Dobrucki, E. J. Chaney, S. A. Boppart, T. M. Fan, S. Lezmi, X. S. Chen, L. C. Yin and J. J. Cheng, *Nat. Chem. Biol.*, 2017, **13**, 415–424.
- 161 K. F. Maass, C. Kulkarni, A. M. Betts and K. D. Wittrup, *AAPS J.*, 2016, **18**, 635–646.
- 162 K. T. Xenaki, S. Oliveira and P. M. P. van Bergen En Henegouwen, *Front. Immunol.*, 2017, **8**, 1287.
- 163 F. Lin, L. Chen, H. Zhang, W. S. C. Ngai, X. M. Zeng, J. Lin and P. R. Chen, *CCS Chem.*, 2019, **1**, 226–236.
- 164 J. C. Kern, M. Cancilla, D. Dooney, K. Kwasnjuk, R. Zhang, M. Beaumont, I. Figueroa, S. Hsieh, L. Liang, D. Tomazela, J. Zhang, P. E. Brandish, A. Palmieri, P. Stivers, M. G. Cheng, G. Feng, P. Geda, S. Shah, A. Beck, D. Bresson, J. Firdos, D. Gately, N. Knudsen, A. Manibusan, P. G. Schultz, Y. Sun and R. M. Garbaccio, *J. Am. Chem. Soc.*, 2016, **138**, 1430–1445.
- 165 V. Chudasama, A. Maruani and S. Caddick, *Nat. Chem.*, 2016, **8**, 114–119.
- 166 Y. Q. Zheng, X. Y. Ji, B. C. Yu, K. L. Ji, D. Gallo, E. Csizmadia, M. Y. Zhu, M. R. Choudhury, L. K. C. D. L. Cruz, V. Chittavong, Z. X. Pan, Z. N. Yuan and L. E. Otterbein, *Nat. Chem.*, 2018, **10**, 787–794.
- 167 K. M. Huttunen, H. Raunio and J. Rautio, *Pharmacol. Rev.*, 2011, **63**, 750–771.
- 168 Y. Barenholz, *J. Control. Release*, 2012, **160**, 117–134.
- 169 Q. X. Yao, F. Lin, X. Y. Fan, Y. P. Wang, Y. Liu, Z. F. Liu, X. Y. Jiang, P. R. Chen and Y. Gao, *Nat. Commun.*, 2018, **9**, 5032.
- 170 R. M. Yusop, A. Unciti-Broceta, E. M. V. Johansson, R. M. Sánchez-Martín and M. Bradley, *Nat. Chem.*, 2011, **3**, 239–243.
- 171 J. T. Weiss, J. C. Dawson, K. G. Macleod, W. Rybski, C. Fraser, C. Torres-Sánchez, E. E. Patton, M. Bradley, N. O. Carragher and A. Unciti-Broceta, *Nat. Commun.*, 2014, **5**, 3277.
- 172 J. Wang, B. Cheng, J. Li, Z. Y. Zhang, W. Y. Hong, X. Chen and P. R. Chen, *Angew. Chem., Int. Ed.*, 2015, **54**, 5364–5368.
- 173 X. Xie, B. Li, J. Wang, C. Y. Zhan, Y. Huang, F. Zeng and S. Z. Wu, *ACS Mater. Lett.*, 2019, **1**, 549–557.
- 174 S. Wilhelm, A. J. Tavares, Q. Dai, S. Ohta, J. Audet, H. F. Dvorak and W. C. W. Chan, *Nat. Rev. Mater.*, 2016, **1**, 16014.
- 175 S. H. Lee, O. K. Park, J. Kim, K. Shin, C. G. Pack, K. Kim, G. Ko, N. Lee, S.-H. Kwon and T. Hyeon, *J. Am. Chem. Soc.*, 2019, **141**, 13829–13840.
- 176 Y. Yuan, L. Wang, W. Du, Z. L. Ding, J. Zhang, T. Han, L. N. An, H. F. Zhang and G. L. Liang, *Angew. Chem., Int. Ed.*, 2015, **54**, 9700–9704.
- 177 W. Du, X. M. Hu, W. C. Wei and G. L. Liang, *Bioconjugate Chem.*, 2018, **29**, 826–837.
- 178 Y. Yuan, J. Zhang, X. L. Qi, S. G. Li, G. S. Liu, S. Siddhanta, I. Barman, X. L. Song, M. T. McMahon and J. W. M. Bulte, *Nat. Mater.*, 2019, **18**, 1376–1383.
- 179 S. Y. Shen, X. Xu, S. Q. Lin, Y. Zhang, H. Y. Liu, C. Zhang and R. Mo, *Nat. Nanotechnol.*, 2021, **16**, 104–113.
- 180 R. Dzijak, J. Galeta, A. Vázquez, J. Kozák, M. Matoušová, H. Fulka, M. Dračínský and M. Vrabec, *JACS Au*, 2021, **1**, 23–30.
- 181 S. N. Ekdawi, D. A. Jaffray and C. Allen, *Nano Today*, 2016, **11**, 402–414.
- 182 F. Seidi, R. Jenjob and D. Crespy, *Chem. Rev.*, 2018, **118**, 3965–4036.
- 183 Y. S. Dong, Y. L. Tu, K. W. Wang, C. F. Xu, Y. Y. Yuan and J. Wang, *Angew. Chem., Int. Ed.*, 2020, **59**, 7168–7172.
- 184 R. Tong and D. S. Kohane, *Annu. Rev. Pharmacol. Toxicol.*, 2016, **56**, 41–57.
- 185 Q. H. Sun, Z. X. Zhou, N. S. Qiu and Y. Q. Shen, *Adv. Mater.*, 2017, **29**, 1606628.
- 186 Y. L. Tu, Y. S. Dong, K. W. Wang, S. Shen, Y. Y. Yuan and J. Wang, *Biomaterials*, 2020, **259**, 120298.
- 187 K. Y. Pu, J. G. Mei, J. V. Jokerst, G. S. Hong, A. L. Antaris, N. Chattopadhyay, A. J. Shuhendler, T. Kurosawa, Y. Zhou, S. S. Gambhir, Z. N. Bao and J. H. Rao, *Adv. Mater.*, 2015, **27**, 5184–5190.
- 188 Y. Y. Jiang and K. Y. Pu, *Acc. Chem. Res.*, 2018, **51**, 1840–1849.
- 189 W. S. Zhang, W. X. Deng, H. Zhang, X. L. Sun, T. Huang, W. J. Wang, P. F. Sun, Q. L. Fan and W. Huang, *Biomaterials*, 2020, **243**, 119934.
- 190 H. Kobayashi, M. Ogawa, R. Alford, P. L. Choyke and Y. Urano, *Chem. Rev.*, 2010, **110**, 2620–2640.
- 191 J. Lin, P. M. Knutsen, A. Muller, D. Kleinfeld and R. Y. Tsien, *Nat. Neurosci.*, 2013, **16**, 1499–1508.
- 192 X. Z. Ai, L. Lyu, Y. Zhang, Y. X. Tang, J. Mu, F. Liu, Y. X. Zhou, Z. H. Zuo, G. Liu and B. G. Xing, *Angew. Chem., Int. Ed.*, 2017, **56**, 3031–3035.
- 193 J. Bussink, J. H. A. M. Kaanders, W. T. A. van der Graaf and W. J. G. Oyen, *Nat. Rev. Clin. Oncol.*, 2011, **8**, 233–242.
- 194 H. M. Chen, W. Z. Zhang, G. Z. Zhu, J. Xie and X. Y. Chen, *Nat. Rev. Mater.*, 2017, **2**, 17024.
- 195 Y. F. Wang, W. Du, T. Zhang, Y. Zhu, Y. H. Ni, C. C. Wang, F. M. S. Raya, L. W. Zou, L. S. Wang and G. L. Liang, *ACS Nano*, 2020, **14**, 9585–9593.
- 196 Z. J. Zhou, D. T. Huang, J. F. Bao, Q. L. Chen, G. Liu, Z. Chen, X. Y. Chen and J. H. Gao, *Adv. Mater.*, 2012, **24**, 6223–6228.
- 197 Z. J. Zhou, Z. H. Zhao, H. Zhang, Z. Y. Wang, X. Y. Chen, R. F. Wang, Z. Chen and J. H. Gao, *ACS Nano*, 2014, **8**, 7976–7985.
- 198 Y. G. Wang, X. H. Li, P. Y. Chen, Y. Dong, G. L. Liang and Y. Q. Yu, *Nanoscale*, 2020, **12**, 1886–1893.
- 199 T. X. Z. Liang, B. H. Zhang, Z. J. Xing, Y. X. Dong, H. M. Xu, X. Q. Chen, L. P. Jiang, J.-J. Zhu and Q. H. Min, *Angew. Chem., Int. Ed.*, 2021, **60**, 11464–11473.
- 200 J. J. Liu, F. Hu, M. Wu, L. L. Tian, F. Gong, X. Y. Zhong, M. C. Chen, Z. Liu and B. Liu, *Adv. Mater.*, 2021, **33**, 2007888.
- 201 D. M. Goldenberg, R. M. Sharkey, G. Paganelli, J. Barbet and J.-F. Chatal, *J. Clin. Oncol.*, 2006, **24**, 823–834.
- 202 M. Patra, K. Zarschler, H.-J. Pietzsch, H. Stephan and G. Gasser, *Chem. Soc. Rev.*, 2016, **45**, 6415–6431.

- 203 M. A. Shah, X. L. Zhang, R. Rossin, M. S. Robillard, D. R. Fisher, T. Bueltmann, F. J. M. Hoeben and T. P. Quinn, *Bioconjugate Chem.*, 2017, **28**, 3007–3015.
- 204 C. S. Hinrichs and S. A. Rosenberg, *Immunol. Rev.*, 2014, **257**, 56–71.
- 205 E. N. Baruch, A. L. Berg, M. J. Besser, J. Schachter and G. Markel, *Cancer*, 2017, **123**, 2154–2162.
- 206 W. J. Li, H. Pan, H. M. He, X. Q. Meng, Q. Ren, P. Gong, X. Jiang, Z. G. Liang, L. L. Liu, M. B. Zheng, X. M. Shao, Y. F. Ma and L. T. Cai, *Small*, 2019, **15**, 1804383.
- 207 H. Pan, W. J. Li, Z. Chen, Y. M. Luo, W. He, M. M. Wang, X. F. Tang, H. M. He, L. L. Liu, M. B. Zheng, X. Jiang, T. Yin, R. J. Liang, Y. F. Ma and L. T. Cai, *Bioact. Mater.*, 2020, **6**, 951–962.
- 208 Z. Chen, H. Pan, Y. M. Luo, T. Yin, B. Z. Zhang, J. H. Liao, M. M. Wang, X. F. Tang, G. J. Huang, G. J. Deng, M. B. Zheng and L. T. Cai, *Small*, 2021, **17**, 2007494.
- 209 Y. T. Han, H. Pan, W. J. Li, Z. Chen, A. Q. Ma, T. Yin, R. J. Liang, F. M. Chen, Y. F. Ma, Y. Jin, M. B. Zheng, B. H. Li and L. T. Cai, *Adv. Sci.*, 2019, **6**, 1900251.
- 210 M. Mitsunaga, M. Ogawa, N. Kosaka, L. T. Rosenblum, P. L. Choyke and H. Kobayashi, *Nat. Med.*, 2011, **17**, 1685–1691.
- 211 K. Sato, K. Ando, S. Okuyama, S. Moriguchi, T. Ogura, S. Totoki, H. Hanaoka, T. Nagaya, R. Kokawa, H. Takakura, M. Nishimura, Y. Hasegawa, P. L. Choyke, M. Ogawa and H. Kobayashi, *ACS Cent. Sci.*, 2018, **4**, 1559–1569.
- 212 T. Komatsu, E. Kyo, H. Ishii, K. Tsuchikama, A. Yamaguchi, T. Ueno, K. Hanaoka and Y. Urano, *J. Am. Chem. Soc.*, 2020, **142**, 15644–15648.
- 213 E. T. Ahrens and J. W. M. Bulte, *Nat. Rev. Immunol.*, 2013, **13**, 755–763.
- 214 I. Rhee, M.-C. Zhong, B. Reizis, C. Cheong and A. Veillette, *Mol. Cell. Biol.*, 2014, **34**, 888–899.
- 215 H. Wang, M. C. Sobral, D. K. Y. Zhang, A. N. Cartwright, A. W. Li, M. O. Dellacherie, C. M. Tringides, S. T. Koshy, K. W. Wucherpfennig and D. J. Mooney, *Nat. Mater.*, 2020, **19**, 1244–1252.
- 216 D. Liße, C. Monzel, C. Vicario, J. Manzi, I. Maurin, M. Copepy, J. Piehler and M. Dahan, *Adv. Mater.*, 2017, **29**, 1700189.
- 217 Z. M. Tang, Y. Y. Liu, M. Y. He and W. B. Bu, *Angew. Chem., Int. Ed.*, 2019, **58**, 946–956.
- 218 F. Zhang, F. Li, G.-H. Lu, W. D. Nie, L. J. Zhang, Y. L. Lv, W. E. Bao, X. Y. Gao, W. Wei, K. Y. Pu and H.-Y. Xie, *ACS Nano*, 2019, **13**, 5662–5673.
- 219 D. Dudziak, A. O. Kamphorst, G. F. Heidkamp, V. R. Buchholz, C. Trumpfheller, S. Yamazaki, C. Cheong, K. Liu, H.-W. Lee, C. G. Park, R. M. Steinman and M. C. Nussenzweig, *Science*, 2007, **315**, 107–111.
- 220 D. J. Irvine, M. A. Swartz and G. L. Szeto, *Nat. Mater.*, 2013, **12**, 978–990.
- 221 F. Li, W. D. Nie, F. Zhang, G. H. Lu, C. L. Lv, Y. L. Lv, W. E. Bao, L. J. Zhang, S. Wang, X. Y. Gao, W. Wei and H.-Y. Xie, *ACS Cent. Sci.*, 2019, **5**, 796–807.
- 222 S. Kourembanas, *Annu. Rev. Physiol.*, 2015, **77**, 13–27.
- 223 Y. Lyu, D. Cui, J. G. Huang, W. X. Fan, Y. S. Miao and K. Y. Pu, *Angew. Chem., Int. Ed.*, 2019, **58**, 4983–4987.
- 224 W. D. Nie, G. H. Wu, J. F. Zhang, L.-L. Huang, J. J. Ding, A. Q. Jiang, Y. H. Zhang, Y. H. Liu, J. C. Li, K. Y. Pu and H.-Y. Xie, *Angew. Chem., Int. Ed.*, 2020, **59**, 2018–2022.
- 225 X. H. Gao, S. Li, F. Ding, X. L. Liu, Y. J. Wu, J. Li, J. Feng, X. Y. Zhu and C. Zhang, *Adv. Mater.*, 2021, **33**, 2006116.
- 226 H. Qin, R. F. Zhao, Y. T. Qin, J. Zhu, L. Chen, C. Z. Di, X. X. Han, K. Cheng, Y. L. Zhang, Y. Zhao, J. Shi, G. J. Anderson, Y. L. Zhao and G. J. Nie, *Adv. Mater.*, 2021, **33**, 2006007.
- 227 J.-F. Lutz, *Angew. Chem., Int. Ed.*, 2008, **47**, 2182–2184.
- 228 T. Plass, S. Milles, C. Koehler, C. Schultz and E. A. Lemke, *Angew. Chem., Int. Ed.*, 2011, **50**, 3878–3881.
- 229 A.-C. Knall and C. Slugovc, *Chem. Soc. Rev.*, 2013, **42**, 5131–5142.
- 230 X. S. Hou, C. F. Ke and J. F. Stoddart, *Chem. Soc. Rev.*, 2016, **45**, 3766–3780.
- 231 P. R. Wratil, R. Horstkorte and W. Reutter, *Angew. Chem., Int. Ed.*, 2016, **55**, 9482–9512.
- 232 J. Du, M. A. Meledeo, Z. Y. Wang, H. S. Khanna, V. D. P. Paruchuri and K. J. Yarema, *Glycobiology*, 2009, **19**, 1382–1401.
- 233 H. Y. Yoon, H. Koo, K. Kim and I. C. Kwon, *Biomaterials*, 2017, **132**, 28–36.
- 234 H. L. P. Tytgat, C.-W. Lin, M. D. Levasseur, M. B. Tomek, C. Rutschmann, J. Mock, N. Liebscher, N. Terasaka, Y. Azuma, M. Wetter, M. F. Bachmann, D. Hilvert, M. Aebi and T. G. Keys, *Nat. Commun.*, 2019, **10**, 5403.
- 235 P. R. Wratil, R. Horstkorte and W. Reutter, *Angew. Chem., Int. Ed.*, 2016, **55**, 9482–9512.
- 236 H. Jiang, A. López-Aguilar, L. Meng, Z. W. Gao, Y. N. Liu, X. Tian, G. L. Yu, B. Ovrnyn, K. W. Moremen and P. Wu, *Angew. Chem., Int. Ed.*, 2018, **57**, 967–971.
- 237 C. Agatemor, M. J. Buettner, R. Ariss, K. Muthiah, C. T. Saeui and K. J. Yarema, *Nat. Rev. Chem.*, 2019, **3**, 605–620.
- 238 L. K. Mahal and C. R. Bertozzi, *Chem. Biol.*, 1997, **4**, 415–422.
- 239 N. J. Agard and C. R. Bertozzi, *Acc. Chem. Res.*, 2009, **42**, 788–797.
- 240 T. A. Denison and Y. H. Bae, *J. Control. Release*, 2012, **164**, 187–191.
- 241 N. Sim and D. Parker, *Chem. Soc. Rev.*, 2015, **44**, 2122–2134.
- 242 H. Koo, M. Choi, E. Kim, S. K. Hahn, R. Weissleder and S. H. Yun, *Small*, 2015, **11**, 6458–6466.
- 243 M. K. Shim, H. Y. Yoon, J. H. Ryu, H. Koo, S. Lee, J. H. Park, J.-H. Kim, S. Lee, M. G. Pomper, I. C. Kwon and K. Kim, *Angew. Chem., Int. Ed.*, 2016, **55**, 14698–14703.
- 244 L. H. Du, H. Qin, T. Ma, T. Zhang and D. Xing, *ACS Nano*, 2017, **11**, 8930–8943.
- 245 S. Lee, S. Jung, H. Koo, J. H. Na, H. Y. Yoon, M. K. Shim, J. Park, J.-H. Kim, S. Lee, M. G. Pomper, I. C. Kwon, C.-H. Ahn and K. Kim, *Biomaterials*, 2017, **148**, 1–15.
- 246 S. Lim, H. Y. Yoon, H. J. Jang, S. Song, W. Kim, J. Park, K. E. Lee, S. Jeon, S. Lee, D.-K. Lim, B.-S. Kim, D.-E. Kim and K. Kim, *ACS Nano*, 2019, **13**, 10991–11007.

- 247 Y. C. Li, X. H. Xu, X. Zhang, Y. K. Li, Z. J. Zhang and Z. W. Gu, *ACS Nano*, 2017, **11**, 416–429.
- 248 H. J. Zhao, B. B. Zhao, L. X. Wu, H. F. Xiao, K. L. Ding, C. X. Zheng, Q. L. Song, L. L. Sun, L. Wang and Z. Z. Zhang, *ACS Nano*, 2019, **13**, 12553–12566.
- 249 X. T. Jiang, J. Xu, M. F. Liu, H. Xing, Z. M. Wang, L. Huang, A. L. Mellor, W. Wang and S. Wu, *Cancer Lett.*, 2019, **462**, 23–32.
- 250 F. Y. Zhou, B. Feng, H. J. Yu, D. G. Wang, T. T. Wang, Y. T. Ma, S. L. Wang and Y. P. Li, *Adv. Mater.*, 2019, **31**, e1805888.
- 251 Y. J. Xie, M. Dougan, N. Jailkhani, J. Ingram, T. Fang, L. Kummer, N. Momin, N. Pishesha, S. Rickelt, R. O. Hynes and H. Ploegh, *Proc. Natl. Acad. Sci. U. S. A.*, 2019, **116**, 7624–7631.
- 252 Y. Xu, J. W. Liu, Z. Y. Liu, H. Ren, J. H. Yong, W. L. Li, H. Wang, Z. Yang, Y. L. Wang, G. G. Chen and X. M. Li, *ACS Nano*, 2020, **14**, 9780–9795.
- 253 M. Compte, S. L. Harwood, I. G. Muñoz, R. Navarro, M. Zonca, G. Perez-Chacon, A. Erce-Llamazares, N. Merino, A. Tapia-Galisteo, A. M. Cuesta, K. Mikkelsen, E. Caleiras and N. Nuñez, *Nat. Commun.*, 2018, **9**, 4809.
- 254 M. P. Avanzi, O. Yeku, X. H. Li, D. P. Wijewarnasuriya, D. G. van Leeuwen, K. Cheung, H. Park, T. J. Purdon, A. F. Daniyan, M. H. Spitzer and R. J. Brentjens, *Cell Rep.*, 2018, **23**, 2130–2141.
- 255 J. Qiao, Z. D. Liu, C. B. Dong, Y. Luan, A. L. Zhang, C. Moore, K. Fu, J. J. Peng, Y. Wang, Z. H. Ren, C. H. Han, T. Xu and Y.-X. Fu, *Cancer Cell*, 2019, **35**, 901–915.
- 256 Y. H. Zhang, C. M. Fang, R. E. Wang, Y. Wang, H. Guo, C. Guo, L. J. Zhao, S. H. Li, X. Li, P. G. Schultz, Y. J. Cao and F. Wang, *Proc. Natl. Acad. Sci. U. S. A.*, 2019, **116**, 15889–15894.
- 257 F. Combes, E. Meyer and N. N. Sanders, *J. Control. Release*, 2020, **327**, 70–87.
- 258 L. Milling, Y. Zhang and D. J. Irvine, *Adv. Drug Delivery Rev.*, 2017, **114**, 79–101.
- 259 B. Olson, Y. D. Li, Y. Lin, E. T. Liu and A. Patnaik, *Cancer Discovery*, 2018, **8**, 1358–1365.
- 260 J. Galon and D. Bruni, *Nat. Rev. Drug Discovery*, 2019, **18**, 197–218.
- 261 J. S. O'Donnell, M. W. L. Teng and M. J. Smyth, *Nat. Rev. Clin. Oncol.*, 2019, **16**, 151–167.
- 262 R. S. Riley, C. H. June, R. Langer and M. J. Mitchell, *Nat. Rev. Drug Discovery*, 2019, **18**, 175–196.
- 263 B. W. Li, P. L. Liu, H. Wu, X. Xie, Z. L. Chen, F. Zeng and S. Z. Wu, *Biomaterials*, 2017, **138**, 57–68.
- 264 F. M. Wang, Y. Zhang, Z. Du, J. S. Ren and X. G. Qu, *Nat. Commun.*, 2018, **9**, 1209.
- 265 X. Y. Ji, R. E. Aghoghovbia, L. K. C. D. L. Cruz, Z. X. Pan, X. X. Yang, B. C. Yu and B. H. Wang, *Org. Lett.*, 2019, **21**, 3649–3652.
- 266 L.-L. Huang, W. D. Nie, J. F. Zhang and H.-Y. Xie, *Acc. Chem. Res.*, 2020, **53**, 276–287.
- 267 M. O. N. van de L'Isle, M. C. Ortega-Liebana and A. Unciti-Broceta, *Curr. Opin. Chem. Biol.*, 2020, **61**, 32–42.
- 268 Y. Zhang, T. Y. Ren, J. X. Gou, L. Zhang, X. G. Tao, B. Tian, P. Q. Tian, D. D. Yu, J. B. Song, X. L. Liu, Y. H. Chao, W. Xiao and X. Tang, *J. Control. Release*, 2017, **261**, 352–366.
- 269 J. Wen, K. Yang, F. Y. Liu, H. J. Li, Y. Q. Xu and S. G. Sun, *Chem. Soc. Rev.*, 2017, **46**, 6024–6045.
- 270 Z. Y. Deng and S. Y. Liu, *J. Control. Release*, 2020, **326**, 276–296.
- 271 M. F. Debets, S. S. van Berkel, J. Dommerholt, A. J. Dirks, F. P. J. T. Rutjes and F. L. van Del, *Acc. Chem. Res.*, 2011, **44**, 805–815.
- 272 E. Kim and H. Koo, *Chem. Sci.*, 2019, **10**, 7835–7851.
- 273 D. Schulz, J. M. Holstein and A. Rentmeister, *Angew. Chem., Int. Ed.*, 2013, **52**, 7874–7878.
- 274 J. M. Holstein, L. Anhäuser and A. Rentmeister, *Angew. Chem., Int. Ed.*, 2016, **55**, 10899–10903.
- 275 K. Hartstock, B. S. Nilges, A. Ovcharenko, N. V. Cornelissen and N. Püllen, *Angew. Chem., Int. Ed.*, 2018, **57**, 6342–6346.
- 276 D. Stummer, C. Herrmann and A. Rentmeister, *ChemistryOpen*, 2015, **4**, 295–301.
- 277 J. M. Holstein, F. Muttach, S. H. H. Schiefelbein and A. Rentmeister, *Chemistry*, 2017, **23**, 6165–6173.
- 278 L. Anhäuser, S. Hüwel, T. Zobel and A. Rentmeister, *Nucleic Acids Res.*, 2019, **47**, e42.
- 279 Z. W. Chen, H. J. Li, Y. J. Bian, Z. J. Wang, G. J. Chen, X. D. Zhang, Y. M. Miao, D. Wen, J. Q. Wang, G. Wan, Y. Zeng, P. Abdou, J. Fang, S. Li, C.-J. Sun and Z. Gu, *Nat. Nanotechnol.*, 2021, **16**, 933–941.